JCB Journal of Cell Biology

ARTICLE

RIM-binding protein couples synaptic vesicle recruitment to release sites

Astrid G. Petzoldt[1*], Torsten W.B. Götz[1*], Jan Heiner Driller[3*], Janine Lützkendorf[1*], Suneel Reddy-Alla[1], Tanja Matkovic-Rachid[1], Sunbin Liu[3], Elena Knoche[1], Sara Mertel[1], Vladimir Ugorets[1], Martin Lehmann[4], Niraja Ramesh[1], Christine Brigitte Beuschel[1], Benno Kuropka[5], Christian Freund[5], Ulrich Stelzl[6], Bernhard Loll[3], Fan Liu[4], Markus C. Wahl[3,7], and Stephan J. Sigrist[1,2]

At presynaptic active zones, arrays of large conserved scaffold proteins mediate fast and temporally precise release of synaptic vesicles (SVs). SV release sites could be identified by clusters of Munc13, which allow SVs to dock in defined nanoscale relation to Ca^{2+} channels. We here show in *Drosophila* that RIM-binding protein (RIM-BP) connects release sites physically and functionally to the ELKS family Bruchpilot (BRP)-based scaffold engaged in SV recruitment. The RIM-BP N-terminal domain, while dispensable for SV release site organization, was crucial for proper nanoscale patterning of the BRP scaffold and needed for SV recruitment of SVs under strong stimulation. Structural analysis further showed that the RIM-BP fibronectin domains form a "hinge" in the protein center, while the C-terminal SH3 domain tandem binds RIM, Munc13, and Ca^{2+} channels release machinery collectively. RIM-BPs' conserved domain architecture seemingly provides a relay to guide SVs from membrane far scaffolds into membrane close release sites.

Introduction

Chemical synapses are the fundamental building blocks of neuronal communication, allowing for a fast and directional exchange of chemical signals between a neurotransmitter releasing presynaptic and receiving postsynaptic target cells. To couple synaptic vesicle (SV) release to electrical stimulation by action potentials, Ca^{2+} ions entering the cell through voltage-gated Ca^{2+} channels activate the Ca^{2+} sensor synaptotagmin that is anchored on SVs to trigger fusion events (Jahn and Fasshauer, 2012; Stanley, 2016). The presynaptic site of SV fusion ("active zone" [AZ]) is covered by an electron-dense scaffold ("cytomatrix") formed by a set of large conserved multidomain proteins (Südhof, 2012; Van Vactor and Sigrist, 2017). How individual AZ scaffold proteins intersect mechanistically with the SV cycle still remains largely enigmatic, though such knowledge was of importance to properly model synapse function in healthy and diseased circuits.

On the level of the individual AZs, recent data from both cultivated rodent neurons and *Drosophila* in vivo neurons suggest that the AZ cytomatrix provides stable SV release sites or "fusion slots" via the clustering of the critical release factor (m)Unc13. The number of such release sites seems to be determined independently of the mechanisms controlling release probability (Böhme et al., 2016; Reddy-Alla et al., 2017; Sakamoto et al., 2018). How SV release sites might be coupled and integrated with additional processes organized by the AZ scaffold, such as the recruitment of SVs under high demand periods of resupply (e.g., high action potential frequencies), remains a largely open question.

The physically extended ELKS family protein (glutamic acid [E], leucine [L], lysine [K],and serine [S]-rich protein) Bruchpilot (BRP) not only operates as the fundamental building block of the *Drosophila* AZ scaffold (Wagh et al., 2006) but was also shown to promote SV recruitment depending on a binding motif at its extreme, AZ membrane-distal C terminus (Hallermann et al., 2010b). Adaptor proteins physically and functionally connecting such extended scaffold proteins, which sample the cytoplasm, and the SV release sites at the AZ membrane might well be relevant in this regard. Rab3-interacting molecule (RIM)-binding proteins (RIM-BPs) are an evolutionarily conserved family of extended AZ scaffold proteins, obviously critical for SV release at *Drosophila* and mammalian central synapses (Acuna et al., 2015, 2016; Grauel et al., 2016; Hibino et al., 2002;

[1]Freie Universität Berlin, Institute for Biology and Genetics, Berlin, Germany; [2]NeuroCure, Charité, Berlin, Germany; [3]Freie Universität Berlin, Institute of Chemistry and Biochemistry/Structural Biochemistry Berlin, Berlin, Germany; [4]Leibniz-Forschungsinstitut für Molekulare Pharmakologie im Forschungsverbund Berlin e.V., Campus Berlin-Buch, Berlin, Germany; [5]Universität Berlin, Institute for Chemistry and Biochemistry, Berlin, Germany; [6]Institut für Pharmazeutische Wissenschaften, Graz, Austria; [7]Helmholtz-Zentrum Berlin für Materialien und Energie, Macromolecular Crystallography, Berlin, Germany.

*A.G. Petzoldt, T.W.B. Götz, J.H. Driller, and J. Lützkendorf contributed equally to this paper; Correspondence to Stephan J. Sigrist: stephan.sigrist@fu-berlin.de; Markus C. Wahl: markus.wahl@fu-berlin.de.

Liu et al., 2011). RIM-BP family proteins with the C-terminal SH3-II/III domains bind to Ca^{2+} channels (Hibino et al., 2002; Liu et al., 2011), release factor Unc13A (Böhme et al., 2016), and RIM, another critical AZ scaffold protein. At *Drosophila* neuromuscular junction (NMJ) synapses, *rim-bp* null alleles provoke a most severe functional phenotype (Liu et al., 2011), stronger than for *rim* and *rim-bp* single mutants at most mammalian synapses (Andrews-Zwilling et al., 2006; Betz et al., 2001; Brockmann et al., 2019). Here we exploit the severity of the synaptic *Drosophila rim-bp* phenotype for a detailed structure-function analysis at *Drosophila* larval neuromuscular (NMJ) synapses. We find that elimination of the individual RIM-BP SH3 domains affected transport to AZs severely; however, the low levels of properly locating RIM-BP-ΔSH3 variants were still able to rescue the "nanoscopic" defects of *rim-bp* null mutants AZ scaffolds. Our crystallographic analysis of the RIM-BP fibronectin III–like (FN-III) domain cluster describes an extended "hinge" in the protein center, which likely plays conformational roles. Finally, the N-terminal region (NTR) of RIM-BP was required to properly organize the overall nanoscopic architecture of the AZ scaffold. While SV docking and numbers of (m)Unc13 clusters remained at normal levels, the NTR was specifically needed for efficient SV recruitment. Thus, we suggest that RIM-BP family proteins evolved as adaptors physically and functionally connecting SV release sites with BRP/ELKS-dependent SV recruitment processes.

Results

RIM-BP family proteins are highly conserved across animal phyla (Mittelstaedt and Schoch, 2007). The reason for their fixed overall domain organization remains unclear but might well reflect an overall functional principle encompassing the entire protein. The single *Drosophila* RIM-BP protein is critical for SV release, but equally needed for AZ structural organization at NMJ glutamatergic synapses, with *rim-bp* null situations displaying a highly disordered core BRP-scaffold when inspected with nanoscopy (Liu et al., 2011). We sought to reconcile the RIM-BP domain architecture with the several discrete functionalities assigned to the protein.

The RIM-BP N-terminal domain connects to the canonical part of the BRP scaffold

We started by asking which interactions might be relevant for RIM-BP's role in the nanoscopic patterning of the AZ scaffold. All RIM-BP family members display three SH3 domains, whose specific sequence identity (Fig. S1 A) and order have been conserved through evolution (Mittelstaedt and Schoch, 2007). While the first SH3-I domain is located in the N-terminal half, a pair of SH3 domains (SH3-II and SH3-III) is located in the C-terminal half of RIM-BPs (Fig. 1 A). SH3 domains mediate protein–protein interactions (PPIs) by binding to proline-rich motifs. RIM-BPs bind via their SH3-II/III domains to voltage-gated Ca^{2+} channel α1 subunits (Hibino et al., 2002; Wang et al., 2000, 2002), with sequence and position of interaction motifs and domains highly similar between *Drosophila* and mammals (Siebert et al., 2015).

First, we probed discrete RIM-BP domains for interaction with other AZ core proteins (BRP, RIM-family), the AZ-residing release factors (i.e., Unc13A), and the intracellular Ca^{2+} channel intracellular C terminus. Thus, we used a systematic, robot-based yeast two-hybrid (Y2H) matrix screening protocol (Worseck et al., 2012). Here, all interactions were tested in two bait–prey and two prey–bait configurations, comprising a total number of 2,424 pairwise tests (Stelzl et al., 2005; Venkatesan et al., 2008; Hegele et al., 2012; see Materials and methods).

In our Y2H analysis, the RIM-BP SH3-II/III domains as expected bound robustly to ligands containing K/RPPXP motifs: voltage-gated Ca^{2+} channel α1 subunit Cacophony (Kittel et al., 2006; Liu et al., 2011), Unc13A (Böhme et al., 2016), and kinesin adaptor Aplip1 (Siebert et al., 2015; Fig. 1 B). In contrast, we did not observe any interactions of the first RIM-BP SH3 domain to these or other PXXP ligands (data not shown). Taken together, the C-terminal SH3 domain tandem of *Drosophila* RIM-BP seems to specifically bundle interactions to AZ release and transport factors.

Still, direct interactions of the RIM-BP SH3-II/III domains with BRP, the only representative of the ELKS family in *Drosophila* and core AZ scaffold organizer (Kittel et al., 2006; Wagh et al., 2006), could not be detected. Sequence homology between *Drosophila* RIM-BP and mammalian RIM-BP1 also extends across the entire NTR but is particularly pronounced in regions of predicted high α-helical character (Fig. S1 B). We recombinantly expressed two small variants of the NTR, NTR^{8-151}, and NTR^{8-254}. Equilibrium circular dichroism (CD) spectra revealed indeed a predominantly α-helical folding for both constructs (Fig. S1 C). Additionally, CD-based thermal melting/reannealing suggested the presence of a folded domain that could refold after thermal denaturation (Fig. S1 D). Numerous ER/K motifs present in the NTR may stabilize α helices (Swanson and Sivaramakrishnan, 2014) and may lead to the formation of coiled-coils (Lupas and Bassler, 2017). Notably, in the Y2H assay, the NTR (residues 1–600) displayed robust interactions with a highly conserved region of BRP (residues 100–650; Fig. 1 B) but not with any other of the known RIM-BP–interacting proteins. The region of BRP that exhibits Y2H interactions with the RIM-BP NTR is contained in both major BRP isoforms (BRP-190 and BRP-170) and previously was shown to be crucial for overall AZ integrity (Fouquet et al., 2009; Matkovic et al., 2013).

As Y2H by itself is insufficient to verify interactions, we first intended to use in vitro interaction testing between recombinantly expressed proteins to probe this interaction using standard pull-down assays. Unfortunately, while the relevant RIM-BP region (residues 1–600) could per se be expressed, a major fraction of the material despite efforts remained largely insoluble, precluding stringent in vitro binding analysis of this region. Consistent with an interaction between RIM-BP and BRP protein, however, we could efficiently coprecipitate RIM-BP with BRP and vice versa from *Drosophila* head lysates (Fig. S2 A).

To use an unbiased approach when exploring the direct binding of RIM-BP to other AZ scaffold proteins from in vivo material, we entailed chemical cross-linking in combination with mass spectrometry (for a schematic representation, see Fig. 1 C; Leitner et al., 2016; Liu and Heck, 2015). More

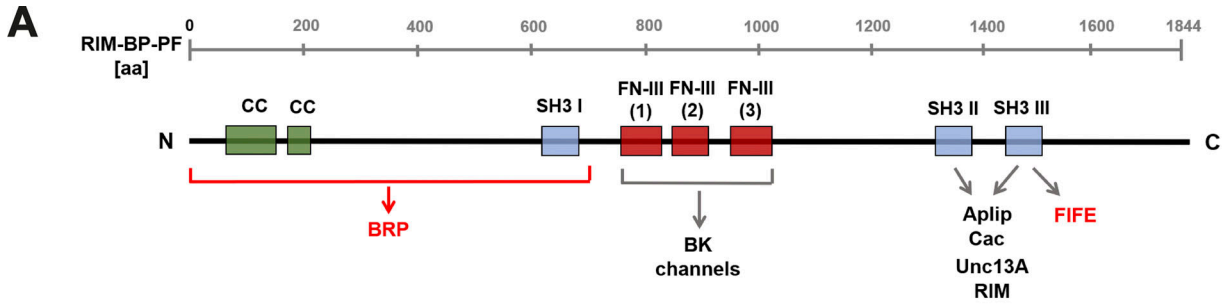

B

RIM-BP	Nterm + CC (1-600 aa)	SH3-I - FN-III(3) (610 -1042 aa)	FN-III (1) - (3) (745-1042aa)	SH3-II (1040-1382 aa)	only SH3-III (1441-1507 aa)	SH3-III to end (1441-1844 aa)
Cac (Cterm) 1500-1848				80	70	92
Unc13A (PxxP motif) 1-606				100	83	83
Aplip1 (PxxP motif)1-250		100		100	100	80
RIM (Zn) 1-227	100	100				
RIM (PxxP motif) 1135-1306				100	100	100
FIFE (PDZ + C2) 474-794					75	80
BRP 100-650	100					

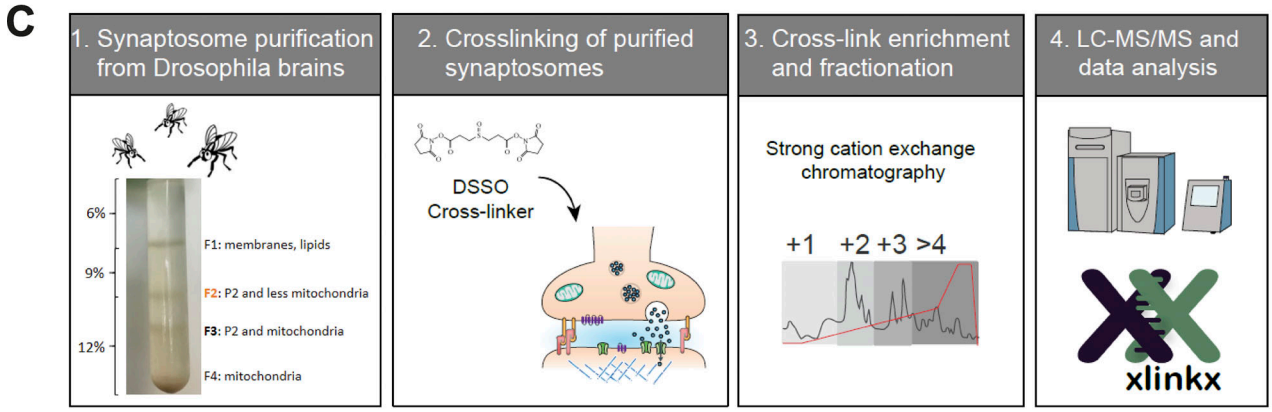

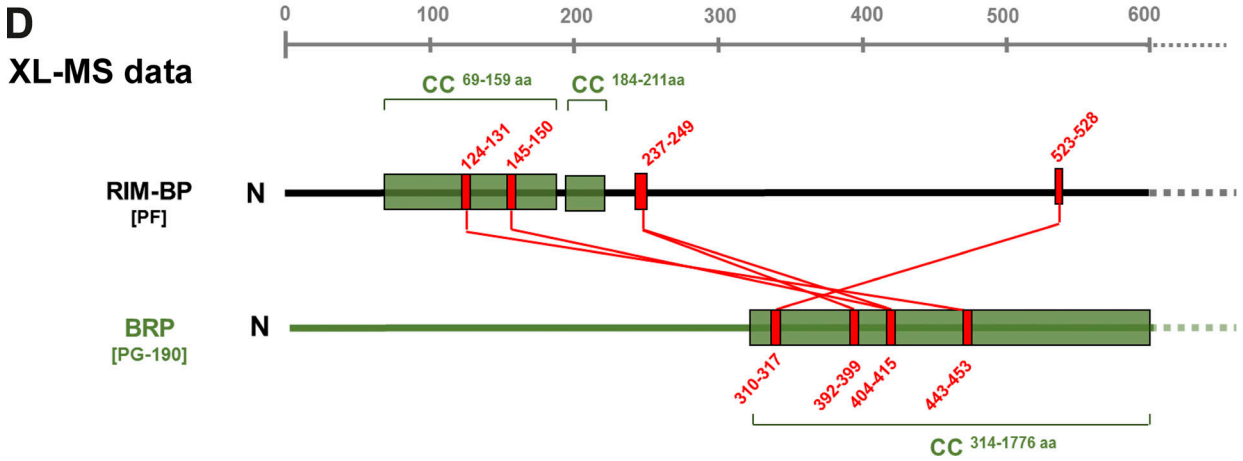

Figure 1. **An interaction matrix between RIM-BP and other AZ core components. (A)** RIM-BP domain structure depicting the protein domains (green: coiled-coil, blue: SH3 domains, red: FN-III domains). The known interaction partners (black) and new interaction partners (red) identified in our Y2H screen are indicated (see B). **(B)** Identification of protein–protein interactions using the systematic automated large-scale mating Y2H approach. High confident RIM-BP interactions are shown and listed in the table. The top five rows show intermolecular interactions that have been described previously between RIM-BP molecules for the C-terminal SH3 domains with the PxxP motif containing AZ players Cac (first row), Unc13A (second row), Aplip (third row), and RIM (fourth and fifth rows). We here identified Fife (sixth row, PxxP motif) as a novel RIM-BP SH3-III binding partner. Row 7 shows the novel interaction of the NTR of RIM-BP with the highly conserved N-terminal Cast domain of BRP. The columns show all truncated RIM-BP constructs used, starting from the N-terminal (left) to the C-terminal (right). Each field contains the information about the protein interaction probability as follows: dark color within an individual field indicates a high interaction probability (>100%), whereas a lighter color indicates a reduced interaction probability (<100%). The protein interaction probability (p) was calculated by dividing the number of interactions received (n) by how often the interactions have been tested (nΣ) as follows: $p_{\text{protein interaction}} = n_{\text{received protein interactions}}/n\Sigma_{\text{all tested protein interactions}}$. **(C)** Schematic representation of the work flow of the cross-linking experiments. **(D)** Cross-link mapping between RIM-BP and BRP between the NTDs (0–600 aa) of both proteins. Lys-Lys cross-links were identified by mass spectrometry with two interaction sites within and two outside of

the coiled-coil domain of the RIM-BP NTD all interacting with the BRP coiled-coil domain (amino acid sequence of interacting peptides indicated in the schematic representation).

specifically, we applied the disuccinimidyl sulfoxide cross-linker on a synaptosome preparation from *Drosophila* brains (Fig. S2, B and C), which we previously developed (Depner et al., 2014). Through extensive proteomics analysis, thousands of cross-links across the synaptic proteome were retrieved (data not shown). These cross-links represent residue-to-residue connections that are within a maximum distance restraint defined by the cross-linker in 3D space. Notably, for RIM-BP, these analyses in total provided five cross-links, which were all positioned within the RIM-BP NTR and connected to a specific stretch of BRP (residues 300–600; Fig. 1 D), consistent with the Y2H analysis data (Fig. 1 B). Thus, our cross-linking proteomics analysis provides independent evidence from in vivo–derived material that the NTR of RIM-BP and a region covering residues 300–600 of BRP mediate contact between these two key AZ scaffold organizers. The fact that only this scaffold–scaffold interaction, but not e.g., interactions of the conserved SH3 domains, could be retrieved by cross-linking points toward a stable "stoichiometric" nature of the RIM-BP::BRP interaction.

These cross-links represent residue-to-residue connections that are within a maximum distance restraint defined by the cross-linker in 3D space. Notably, for RIM-BP, these analyses in total provided five cross-links, which were all positioned within the RIM-BP NTR and connected to a specific stretch of BRP (residues 300–600; Fig. 1 D),

Crystallographic analysis: A hinge-like fibronectin-III array in the RIM-BP center

The structural organization and functional role of the highly conserved array of FN-III domains (Fig. S1 D) in the RIM-BP central part (Fig. 1 A) remained enigmatic so far, despite the recent finding of big potassium channels (BK-channels) binding to this motif (Sclip et al., 2018). We determined the crystal structure of a corresponding RIM-BP fragment (residues 745–1042; RIM-BP$^{745\text{-}1042}$; Fig. 2 A) at 2.45 Å resolution to compare the organization of the FN-III region in RIM-BP to other FN-III arrays and precisely delineate domain borders for subsequent genetic manipulation of the protein in vivo.

An asymmetric unit of the crystals contained two RIM-BP$^{745\text{-}1042}$ chains, in which residues 745–838, 843–945, and 946–1,042 formed the three FN-III domains (Fig. 2 B, Fig. S2 E, and Table S1). FN-III regions in several proteins have been shown to homodimerize (Carr et al., 2001). However, bioinformatics analysis (Krissinel and Henrick, 2007) suggested that RIM-BP$^{745\text{-}1042}$ crystal contacts are not biologically relevant. CoMulti-angle light scattering showed consistently that RIM-BP$^{745\text{-}1042}$ is monomeric in solution ($MW_{theoretical}$: 32,466 D, MW_n: 32,610 ± 107 D [MW, molecular weight]).

FN-III(1) and FN-III(2) interact via a short β-sheet formed between β-strand G of FN-III(1) and the BC loop of FN-III(2) in both copies of the protein (Fig. 2 B). By contrast, FN-III(3) is more loosely appended to FN-III(2). The BC loop of FN-III(3) and the FN-III(2) AB loop interact with the linker region of FN-III(2) and FN-III(3) in one molecule (Fig. 2, C and D). These interactions are lacking in the second molecule, leading to different orientations of the FN-III(3) domains relative to the FN-III(1–2) domains (Fig. 2 D). Analysis of the apparent FN-III(3) movement by the DynDom server (Girdlestone and Hayward, 2016) revealed a rotation of 32.4° and a translation of −1.3 Å of FN-III(3) relative to FN-III(1–2) due to a bending of the FN-III(2)–FN-III(3) linker region (Fig. 2 E).

Most of the published arrays of FN-III regions adopt an arrangement with no or few direct contacts between the FN-III domains. The tight contacts of the FN-III(1–2) module resemble the arrangement of the D4 and D5 FN-III domains in the extracellular domain of gp130, which allows this region of gp130 to signal without major conformational changes upon ligand binding (Xu et al., 2010). Therefore, while the flexible apposition of FN-III(2) and FN-III(3) indicates that this region represents a hinge-like element within RIM-BP, the FN-III(1–2) region might provide a rigid spacer and/or a preformed binding site for a ligand. However, neither our Y2H analyses (Fig. 1 B) nor pull-down experiments using several FN3 domain constructs and adult fly brain extracts revealed stable binding of the RIM-BP FN-III array to other AZ proteins (data not shown).

In vivo structure/function analysis of the RIM-BP domain organization

Deleting RIM-BP at NMJ synapses provides us with a severe structural and functional phenotype at this highly accessible synapse. Based on this, we started a systematic in vivo structure/function analysis using a series of deletion constructs (see schemes in Fig. 3 A). As extended deletions on genomic level would likely interfere with proper splicing and influence mRNA expression levels in an unpredictable manner, we used inducible cDNA-based constructs. All constructs were equipped with GFP to allow for comparing protein and mRNA expression levels of all constructs via the same sequence tag. We tested for mRNA expression levels in adults ("driving" the constructs with pan-neuronal driver line elav-Gal4) by RT-PCR (against the GFP sequence). No significant expression differences between the to-be-analyzed deletion constructs were detected (Fig. S3 A).

We first tested the rescue activity of all constructs by scoring numbers of surviving adults after expressing the RIM-BP variants in a *rim-bp* null mutant background by elav-Gal4 in three biological replicates (Fig. 3 B). As expected (Liu et al., 2011), only very few mature *rim-bp* null mutant animals could be retrieved. In contrast, transgenic expression of the GFP-tagged full-length RIM-BP (RIM-BP-FL^{GFP}) in *rim-bp* null mutants restored viability in the expected mendelian ratio (Fig. 3 B). Importantly, larvae rescued by RIM-BP-FL^{GFP} showed NMJ morphologies, AZ numbers, and BRP levels indistinguishable from WT (Fig. 3 D; Fig. 4 B; and Fig. S3, B–D). Neither was evoked SV release statistically different from WT (Fig. S3, E–G). We would like to emphasize that though Gal4-driven expression of RIM-BP-FL^{GFP} resulted in clearly increased total protein levels as detected in Western blots

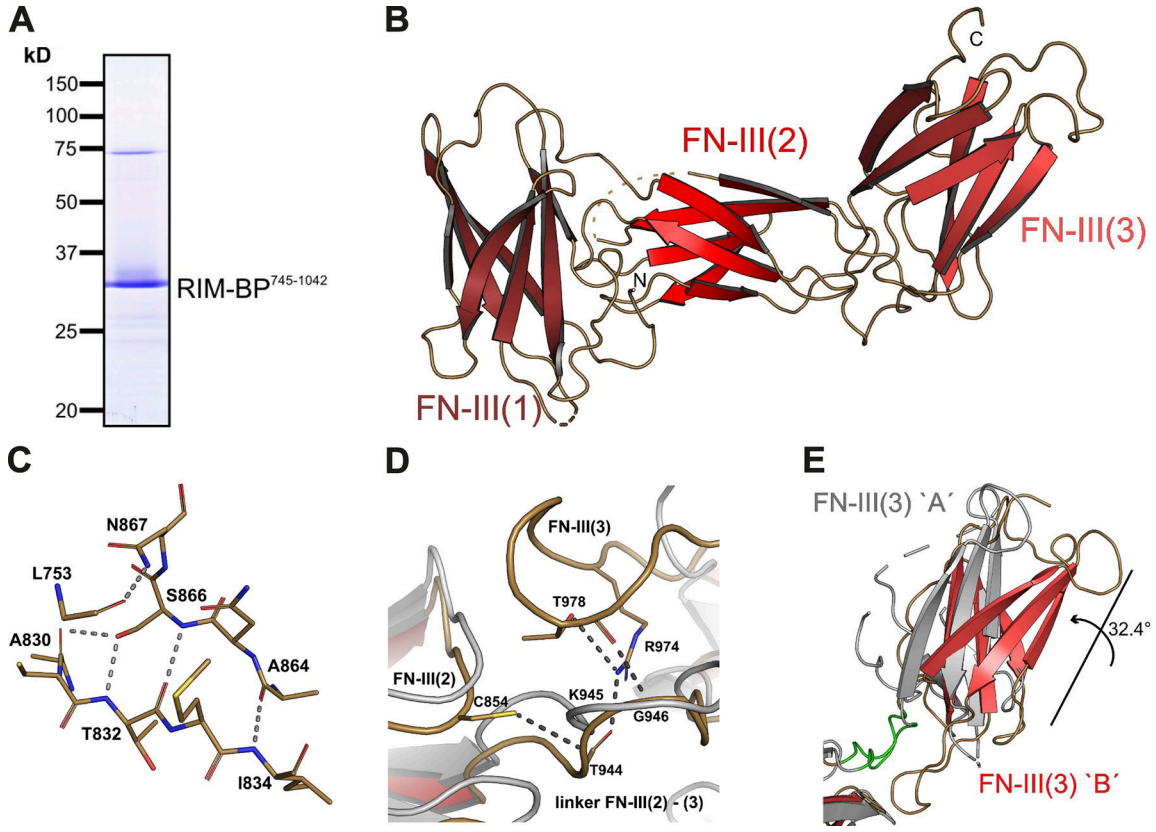

Figure 2. **RIM-BP fibronectin domains form a hinge-like structure. (A)** 12.5% SDS-PAGE analysis of purified RIM-BP$^{745-1042}$, which was used in crystallization experiments. **(B)** A structural cartoon representation of molecule "B" of the three FN-III domains in RIM-BP. Linker regions are colored in sand and β-strands in red, and unmodeled linker regions are indicated by dashed lines. **(C)** Stick representation of the short β-sheet formed between FN-III(1) β-strand G (A830, T832, and I834) and FN-III(2) BC loop (S864, S866, and N867). Gray dashed lines indicate potential hydrogen, bonds with a distance cut-off of ≤3.3 Å. **(D)** Linker region of FN-III(2–3) in molecule "B" (red, sand) and molecule "A" (light gray) when aligning both molecules on FN-III(1–2). Stick representation of side chains involved in potential hydrogen bonds. Gray dashed lines indicate potential hydrogen bonds with a distance cut-off of ≤3.3 Å. **(E)** Alignment of molecules "B" and "A" on the fixed FN-III(1–2) region reveals the movement of the FN-III(3) domain. Flexible linker (green) and the rotation of the domain were calculated by the DynDom server (Girdlestone and Hayward, 2016).

as compared with WT (Fig. S3 H), no signs of any gain-of-function effects were detected here. This is likely explained by transport and especially synapse localization naturally limiting RIM-BP amounts at AZs.

At the AZs of *rim-bp* null mutant larva NMJs (*rim-bp*$^{STOP1/52.01}$), confocal (Fig. 3 C) and stimulated emission depletion microscopy (STED) images (Fig. 4 A) showed a severe misorganization of the BRP scaffold, as expected (Liu et al., 2011). Single-action potential-evoked SV release was drastically reduced (Fig. S4, C–F), while spontaneous release was not altered (Fig. S4, G–I). The RIM-BP-FL^{GFP} localized consistently into the AZ scaffolds in both the mutant and WT background (Fig. 3 D). Planar STED views pictured RIM-BP-FL^{GFP} in the AZ center surrounded by the typical ring of the BRP C-terminal epitope labeled by the Nc82 monoclonal antibody, which resides further from the AZ membrane than the RIM-BP C terminus (Fig. 4 B), as expected from the labeling of the endogenous protein (Liu et al., 2011). Importantly, the STED-nanoscopic BRP distribution was also restored by the expression of RIM-BP-FL^{GFP} in the *rim-bp* null background.

To evaluate the functional role of the FN-III domains, we expressed GFP-tagged constructs bearing deletions of individual FN-III domains in WT and *rim-bp* mutant larvae (Fig. 3, A and E; and Fig. 4 C). Re-expressed RIM-BPΔFN-III(2)^{GFP} and RIM-BPΔFN-III(3)^{GFP} localized faithfully to the AZ in the *rim-bp* mutant background (Fig. 3 E), with their nanoscopic topology in STED images relative to the BPR scaffold appearing very similar to control RIM-BP-FL (Fig. 4, C and H). Although both deletion constructs still rescued the *rim-bp* null mutant lethality (Fig. 3 B), their protein levels at NMJ terminals appeared reduced in the presence of endogenous RIM-BP, possibly indicating that the full-length RIM-BP protein might have advantages over the FN-III(2) and (3) deletion variants in binding into the scaffold. However, in the *rim-bp* mutant background, both constructs reached the synaptic terminal in similar amounts as the RIM-BP-FL^{GFP} construct (Fig. 3 H).

In contrast to these rather weak deficits, deletion of the FN-III(1) domain provoked a nearly total absence of the protein from the synaptic terminal in the *rim-bp* mutant background (Fig. 3, E and H). Consistently, RIM-BPΔFN-III(1)^{GFP} did not rescue viability (Fig. 3 B), and BRP scaffolds appeared as deformed as in *rim-bp* null mutants (Fig. 4, C and H; compare with *rim-bp* mutant Fig. 4 A). Moreover, neurotransmission of this genotype (RBPΔFN-III[1]^{GFP} in *rim-bp* null background) appeared identical to the *rim-bp* null mutant (data not shown). As we were also

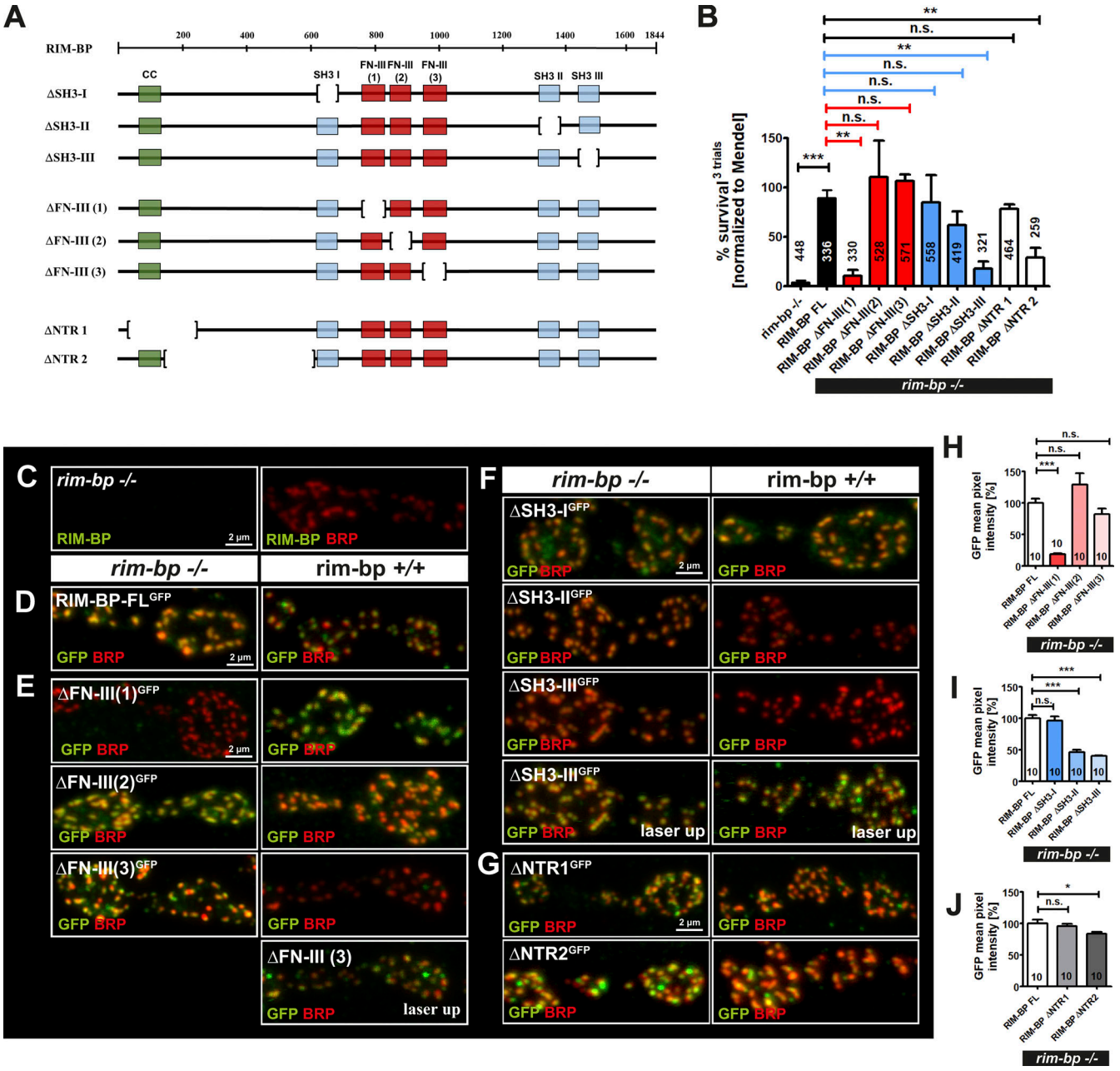

Figure 3. **RIM-BP structure/function analysis. (A)** Schematic representation of the RIM-BP deletion analysis, indicating in brackets the deleted domains. All constructs carry a C-terminal GFP tag. **(B)** Survival rates of adult *Drosophila* flies after reexpression of the RIM-BP-FL^{GFP} (control) and the single deletion constructs in the *rim-bp* mutant background in percentage, normalized to the Mendelian ratio (*rim-bp* mutant 3.66% ± 1.83, 448 flies tested; RIM-BP-FL^{GFP} 89.64% ± 7.83, 336 flies tested; RIM-BPΔFN-III(1)^{GFP} 10.13% ± 5.93, 330 flies tested; RIM-BPΔFN-III(2)^{GFP} 110.2% ± 37.04, 528 flies tested; RIM-BPΔFN-III(3)^{GFP} 106.8% ± 6.14, 571 flies tested; RIM-BPΔSH3-I^{GFP} 85.07% ± 27.31, 558 flies tested; RIM-BPΔSH3-II^{GFP} 61.60% ± 14.01, 419 flies tested; RIM-BPΔSH3-III^{GFP} 17.35% ± 7.78, 321 flies tested; RIM-BPΔNTR1^{GFP} 78.10% ± 4.78, 464 flies tested; RIM-BPΔNTR2^{GFP} 28.49% ± 10.43, 259 flies tested). All graphs show ±SEM. Data distribution was assumed to be normal; see Materials and methods. Unpaired, two-sided *t* test comparing RIM-BP-FL^{GFP} to all other genetic conditions, **, P < 0.01; ***, P < 0.001; n.s., not significant. Three biological replicates were performed, thus *n* = 3 for all datasets with ∼100–200 animals/replicate. **(C–G)** Confocal images of immunostained NMJs of third instar *Drosophila* larvae of the *rim-bp* mutant (C) and the RIM-BP-FL construct (D), RIM-BP FN-III deletion constructs (E), the RIM-BP SH3 deletion constructs (F), and the RIM-BP NTR deletion constructs (G), all in WT (+/+) (right panel) and *rim-bp* mutant (−/−) (left panel) background stained for RIM-BP (green, C) or GFP (green, D–G) and the presynaptic scaffold protein BRP (red). Scale bar, 2 µm. **(H)** Quantification of GFP mean pixel intensity per NMJ area normalized to control of the FN-III domains (RIM-BP-FL^{GFP} 100.0% ± 6.68, *n* = 10; RIM-BPΔFN-III(1)^{GFP} 18.51% ± 1.56, *n* = 10; RIM-BPΔFN-III(2)^{GFP} 129.6% ± 18.06, *n* = 10; RIM-BPΔFN-III(3)^{GFP} 82.48% ± 9.07, *n* = 10). **(I)** Quantification of GFP mean pixel intensity per NMJ area normalized to control of the SH3 domains (RIM-BP-FL^{GFP} 100.0% ± 5.53, *n* = 10; RIM-BPΔSH3-I^{GFP} 96.05% ± 7.03, *n* = 10; RIM-BPΔSH3-II^{GFP} 46.29% ± 3.37, *n* = 10; RIM-BPΔSH3-III^{GFP} 40.04% ± 1.25, *n* = 10). **(J)** Quantification of GFP mean pixel intensity per NMJ area normalized to control of the NTR domains (RIM-BP-FL^{GFP} 100.0% ± 5.82, *n* = 10; RIM-BPΔNTR1^{GFP} 95.37% ± 3.85, *n* = 10; RIM-BPΔNTR2^{GFP} 83.68% ± 2.78, *n* = 10). **(H–J)** All graphs show ± SEM. Data distribution is normal following D'Agostino and Pearson omnibus normality test. An unpaired, two-sided *t* test comparing RIM-BP-FL^{GFP} to all other genetic conditions was applied, *, P < 0.05; ***, P < 0.001; n.s., not significant. N represents a single NMJ; five animals/two NMJs per animal are analyzed.

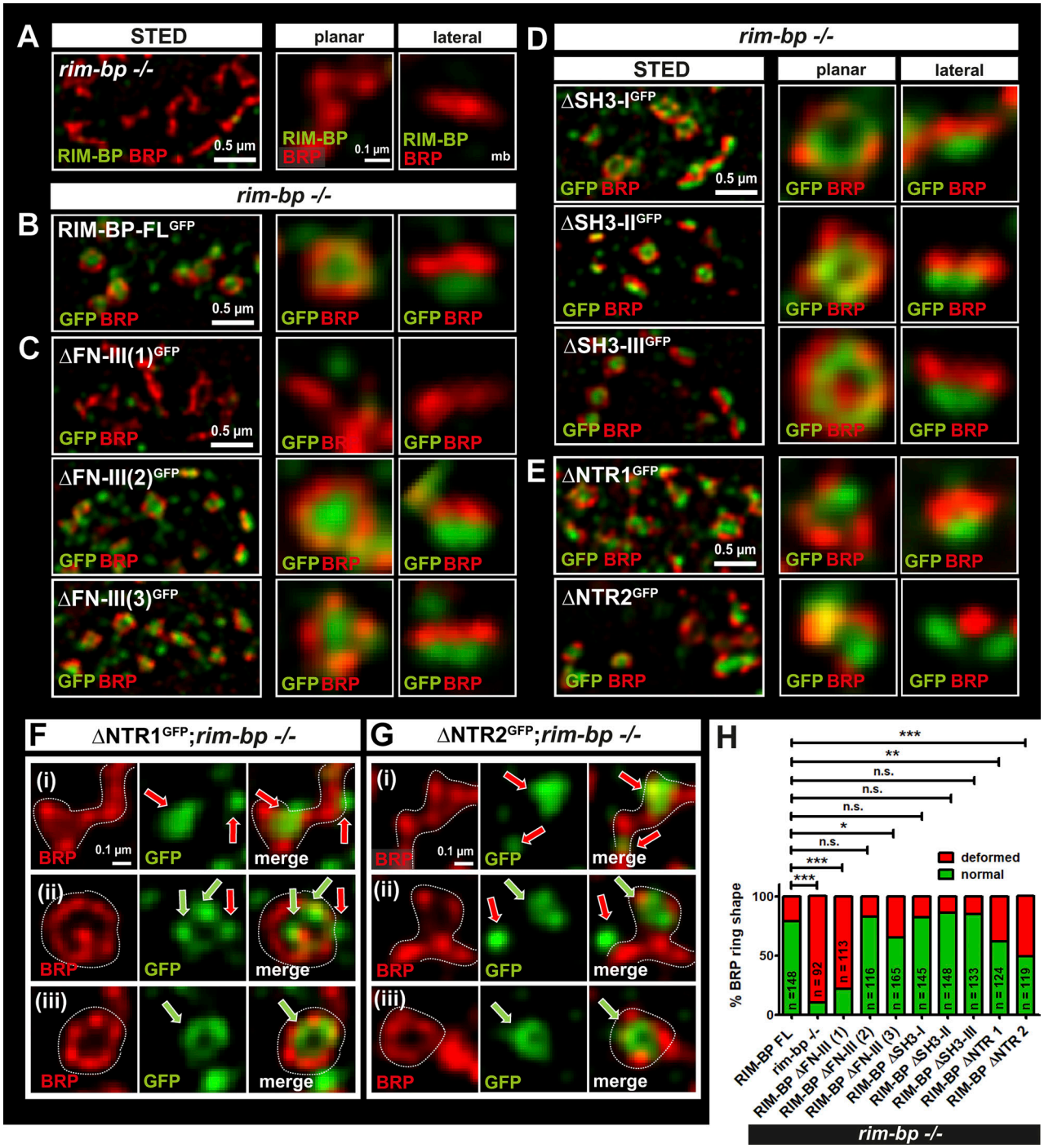

Figure 4. **RIM-BP NTR domain critical for AZ stability and integration into the AZ scaffold. (A–G)** RIM-BP FL, ΔSH3, ΔFN-III, and ΔNTR deletions were reexpressed in the *rim-bp* mutant background and analyzed by STED microcopy, allowing nanoscale analysis of the AZ scaffold architecture and construct integration. STED images of immunostained single AZs of third instar *Drosophila* larvae stained for a RIM-BP (green, A) or GFP (green, B–G) and BRP (red) with one overview (always left panel) and a planar (middle panel) or lateral (right panel) zoom. **(A–E)** *rim-bp* mutant (A), RIM-BP FL in the *rim-bp* mutant background (B), RIM-BP FN-III deletion constructs in the *rim-bp* mutant background (C), the RIM-BP SH3 deletion constructs in the *rim-bp* mutant background (D), RIM-BP NTR deletion constructs in the *rim-bp* mutant background (E; left panel always overview, middle panal planar view single AZ, and right panel lateral view single AZ, mb = membrane of the synaptic cleft). **(F)** Three representative images of the RIM-BPΔNTR1^{GFP} construct or (G) the RIM-BPΔNTR2^{GFP} construct both in the *rim-bp* mutant background showing a range of AZ deformations that can be observed ranging from strong architectural AZ defects (left panel, dashed lines mark the AZ, red arrows indicate delocalized and green arrows correctly localized RIM-BP) over slight deformations (middle panel) to fully restored AZ (right panel). Scale bar overview, 0.5 µm, and single AZ zoom, 0.1 µm. **(H)** Quantification of AZ scaffold architecture of the representative images shown in A–E. RIM-BP-FL^{GFP} 78.98% ± 3.23 normal AZs (BRP C-terminal rings) and 21.02% ± 3.28 deformed AZs (148 AZs analyzed); *rim-bp* mutant with 9.63% ± 2.49 normal AZs and 90.36% ± 2.49 deformed AZs (92 AZs analyzed); RIM-BPΔFN-III(1)^{GFP} 21.83% ± 3.78 normal AZs and 78.17% ± 3.78 deformed AZs (113 AZs analyzed); RIM-BPΔFN-III(2)^{GFP} 82.57% ± 2.36 normal AZs and 17.43% ± 2.36 deformed AZs (116 AZs analyzed); RIM-BPΔFN-III(3)^{GFP} 65.13% ± 1.72 normal AZs and 34.87% ±

1.72 deformed AZs (165 AZs analyzed); RIM-BPΔSH3-I^{GFP} 82.06% ± 3.82 normal AZs and 17.94% ± 3.82 deformed AZs (145 AZs analyzed); RIM-BPΔSH3-II^{GFP} 85.96% ± 1.85 normal AZs and 14.04 ± 1.85 deformed AZs (148 AZs analyzed); RIM-BPΔSH3-III^{GFP} 85.00% ± 2.19 normal AZs and 15.00% ± 2.19 deformed AZs (133 AZs analyzed); RIM-BPΔNTR1^{GFP} 61.70% ± 3.23 normal AZs and 38.31% ± 3.23 deformed AZs (124 AZs analyzed); RIM-BPΔNTR2^{GFP} 49.30% ± 2.74 normal AZs and 50.70% ± 2.74 deformed AZs (119 AZs analyzed). All graphs show ± SEM. Data distribution was assumed to be normal, see Materials and methods. A one-way ANOVA was applied, using the Tukey post-test, *, P < 0.05; **, P < 0.01; ***, P < 0.001; n.s. = not significant. N represents the mean of all AZ (20–40) from one to three boutons (one image); analyzed are two or three animals with two or three NMJs/animal and one to three boutons/NMJ to reach ∼100 AZ/genetic condition.

unable to detect RBPΔFN-III(1)^{GFP} in motoneuron somata and axons (data not shown), we have to conclude that deletion of the first FN-III domain renders the protein unstable in the cell body. Surprisingly, however, in the presence of endogenous RIM-BP, RBPΔFN-III(1)^{GFP} effectively reached the synaptic terminals and integrated into the BRP scaffold (Fig. 3 E). We indeed detected a RIM-BP band corresponding to RBPΔFN-III(1)^{GFP} in Western blot analysis of larval brains, only in the presence of endogenous RIM-BP and not in the *rim-bp* null mutant background (Fig. S3 H). The most plausible explanation for this is that the RIM-BP protein containing a deletion of the first FN-III domain is rendered unstable, potentially reflecting inappropriate folding, but stabilizes when given the chance to bind the endogenous, properly folded WT RIM-BP.

These results taken together show that the first FN-III domain in RIM-BP is probably critical to properly fold and/or stabilize the protein. Future analyses will have to elucidate the underlying mechanisms of this stability control.

Individual SH3 domains critical for transport but not for overall scaffold architecture

The results above suggested that RIM-BP scaffold integration might be mediated by regions other than the FN-III array. We therefore turned our attention to the SH3 domains. Deletion of the first SH3 domain (RIM-BP ΔSH3-I^{GFP}) did not have a major effect on the rescue rate (Fig. 3 B), did not influence the AZ targeting and nanoscopic integration of the protein, and completely rescued the scaffold assembly at NMJ synapses (Fig. 3, F and I; and Fig. 4, D and H). Thus, somewhat surprisingly, our analysis did not uncover any major functional role for the conserved SH3-I domain at NMJ synapses, in correspondence with our inability to detect binding to other AZ structural proteins and release relevant factors (see above).

The RIM-BPΔSH3-II^{GFP} protein showed slightly reduced rescue rates, while the RIM-BPΔSH3-III^{GFP} construct lacked rescue activity (Fig. 3 B). While both deletion variants were expressed, they reached the synaptic NMJ terminal only at reduced levels (Fig. 3, F and I; for ΔSH3-II, we measured 46%, for ΔSH3-III 40% of control RIM-BP level), probably due to transport impairments, as ectopic GFP signal could be detected in the neuronal somata of the ventral nerve cord (data not shown). We could, however, detect RIM-BPΔSH3-III^{GFP} robustly at the NMJ upon an increase in laser strength (Fig. 3 F), and STED microscopy indicated that both RIM-BPΔSH3-II^{GFP} and RIM-BPΔSH3-III^{GFP} integrated into the AZ scaffold with apparently normal topology. Importantly, both RIM-BPΔSH3-II^{GFP} and RIM-BPΔSH3-III^{GFP} rescued the BRP scaffold nanoarchitecture effectively, even at these reduced levels (Fig. 4, D and H). A double deletion of both SH3 domains (ΔSH3-II+III) led to the nearly complete absence of the protein at the synaptic terminal. In this context, the BRP scaffold appeared as defective as the *rim-bp* null mutant (Fig. S4, A and B), most probably a direct consequence of a nearly complete lack of RIM-BP in this situation.

Previous analyses using two-electrode voltage clamp recordings had shown that *rim-bp* null mutants suffer from severely reduced evoked junctional currents (eEJCs) and charge, and show increased paired pulse facilitation, probably reflecting a looser coupling of SVs to Ca^{2+} influx (Liu et al., 2011; Müller et al., 2015). Surprisingly, no significant defect of single AP-evoked release or spontaneous release could be detected for the RIM-BPΔSH3-III rescue situation (Fig. S4, C–I).

As presence of either SH3-II or SH3-III might suffice to organize Ca^{2+} channel α1 subunit binding, we generated a genomic mutant of the Ca^{2+} channel, in which we altered the PXXP motif that is responsible for the binding to RIM-BP (see Materials and methods; Han et al., 2011; Kaeser et al., 2011). We then compared cells expressing genomic constructs of either WT Ca^{2+} channel (cac wt) or a Ca^{2+} channel with mutated PXXP motif (cac APTA) in a *cac* null background by recording postsynaptic responses to single-action potential stimulation at 1 mM extracellular Ca^{2+}. Surprisingly, no significant differences were detected for eEJC response amplitudes (Fig. S5, A–E). However, there was a slight but significant increase in the time to peak of evoked responses after altering the Cac PXXP RIM-BP interaction motif.

Finally, we tested the ability of isolated SH3-III or SH3-II+III fragments to transport and enter into the AZ scaffold. Consequently, we created SH3-III^{GFP} and SH3-II+III^{GFP} expression constructs also tagged with a C-terminal GFP. Both constructs were effectively transported to the synaptic terminal but failed to integrate into the AZ scaffold in WT and *rim-bp* mutant larvae (Fig. S5 F).

In summary, we find that deletion of neither the second nor the third SH3 domain interferes with the ability of RIM-BP to integrate into the AZ scaffold. Moreover, deletion of either SH3 domain does not interfere with the ability of RIM-BP to establish a proper AZ nanoarchitecture. Genetic elimination of the RIM-BP binding motifs of the Ca^{2+} channel α1 subunit intracellular C terminus also did not "phenocopy" the *rim-bp* null allele. Our data suggest that interactions redundant to the RIM-BP contacts stabilize Ca^{2+} channel: AZ scaffold contacts at NMJ synapses (also see Discussion).

The RIM-BP NTR is critical for BRP scaffold organization

As shown above, the NTR of RIM-BP and a region from residues 300–600 from the BRP side seemingly provide contact surfaces between these two key AZ scaffold organizers. To probe the relevance of this scaffold–scaffold contact, we constructed RIM-BP variants, in which residues 24–250 (ΔNTR1) or residues

152–599 (ΔNTR2) were deleted (Fig. 3 A). Both N-terminal deletion variants were expressed at levels comparable to control protein and reached the synaptic terminal effectively in both the *rim-bp* null mutant and WT background (Fig. 3, G and J; and Fig. S6 A). Thus, RIM-BPΔNTR1^{GFP} and RIM-BPΔNTR2^{GFP} are competent for axonal transport, most probably because both constructs still contain the C-terminal SH3-II/III domains. However, despite efficient transport to synapses, RIM-BP-ΔNTR2^{GFP} was unable to rescue from lethality (Fig. 3 B). Moreover, quantifying NMJs of larvae expressing RIM-BPΔNTR2^{GFP} in the *rim-bp* null background showed that overall active zone numbers (BRP cluster counts) and BRP intensities were not significantly reduced, while the size of individual AZs was slightly increased (Fig. S6, B–D). The RIM-BPΔNTR2^{GFP} levels in STED analyses again appeared similar to control levels (Fig. 4, B and E), while about half of the individual AZ BRP scaffolds appeared as defective as in the null mutant (Fig. 4, A, G, and H).

The RIM-BPΔNTR1^{GFP} variant showed a similar but less severe phenotype. Also, this NTR mutant still was transported effectively to the NMJ terminals (Fig. 3, G and J). STED microscopy also revealed a range of BRP AZ scaffold deficits, which were again qualitatively similar but quantitatively less pronounced compared with the RIM-BPΔNTR2^{GFP} rescue phenotype (Fig. 4, E, F, and H). Consistent with its less pronounced nanoscopic phenotype, RIM-BPΔNTR1^{GFP} rescued from lethality more efficiently than RIM-BPΔNTR2^{GFP} (Fig. 3 B).

We applied EM to address independently scaffold organization and distribution of SVs upon truncating the NTR (Fig. 5, A and B). Consistent with the STED data, T-bars in EM cross-sections appeared morphologically atypical. Most of them appeared reduced in size and decomposed, reflected in a reduced ultrastructural area, length, and height (Fig. 5 C). Thus, both STED and EM analyses suggest that the NTR plays a nonredundant role in structuring the nanoarchitecture of the AZ scaffold, presumably by binding directly to the master AZ scaffold building block, BRP.

RIM cooperates with RIM-BP in the nanoscopic patterning of the BRP-core scaffold

The RIM-BPs, as their name indicates, also bind to RIM family proteins. Two family members, RIM proper (Graf et al., 2012; Müller et al., 2012) and FIFE, an extended Piccolo-RIM family member (Bruckner et al., 2012; Bruckner et al., 2017), function at NMJ synapses in *Drosophila*. RIM bound via a region containing a K/RPPXP motif in the last part of the protein to the C-terminal SH3-III domain, while also Fife bound the RIM-BP SH3-II//III domains via a K/RLPXXP motif in the center of the protein (Fig. 1 B). Given these conserved interactions, we asked whether deficits of *rim-bp* mutants might be also easily explained by defects in RIM localization/function.

So far, RIM and FIFE have been analyzed individually at NMJ synapses but not in a double loss of function situation. To explore redundancies between these two members of the RIM family in *Drosophila*, we subjected both single mutants and the double mutant to electrophysiological analysis (Fig. S7, A and B). As was expected (Graf et al., 2012; Müller et al., 2012), *rim* single mutants displayed severe release deficits, while release deficits were more moderate in *fife* mutants (Fig. S7, A and B). Notably, release in a double mutant combination was only as severely affected as in *rim* single mutants. In *rim* mutants, UNC13A AZ clusters were not reduced (Fig. S7, C and D), suggesting that RIM is functionally needed also beyond likely redundant roles in release machinery clustering and molecular release site definition.

We further analyzed RIM functionality via STED nanoscopy. Despite efforts, we could not retrieve antibodies to visualize the endogenous protein. Thus, we turned to an on-locus GFP insertion into the *rim* locus. We found RIM-GFP to be often localized to discrete clusters at the AZ center, consistent with a function in AZ release (Fig. S7, E and F). We then asked whether BRP AZ scaffold assembly would depend on RIM family proteins. The BRP distribution in *rim* single, *fife* single, and *rim/fife* double mutants appeared essentially unaffected (Fig. S7, G–J), at least on the level retrievable with STED microscopy. To test for functional redundancy between RIM-BP and RIM in the nanoscopic AZ patterning, we created a *rim*, *rim-bp* double loss-of-function mutant by combining a *rim* mutant with RNAi against RIM-BP (Fig. S7, K and L). Indeed, we could detect a significant increase in BRP scaffold defects in the double-LOF (loss-of-function) situation for *rim* and RIM-BP RNAi when compared with the RIM-BP RNAi situation (Fig. S7 L). Thus, RIM seems to operate synergistically with RIM-BP in establishing the AZ nanoscopic architecture.

The RIM-BP NTR is dispensable for SV/Ca^{2+} channel coupling and release site definition

We continued analyzing the RIM-BPΔNTR2^{GFP} situation. Despite the overall misorganization of the AZ scaffold, the density of Unc13A-positive release sites in STED images was not reduced but even slightly increased (Fig. 5, E and F). The total numbers of SVs in EM appeared unchanged, and SV docking persisted largely undisturbed (Fig. 5 D). Interestingly, however, we discovered that SVs tethered to the distal parts of the T-bars were significantly reduced, potentially pointing toward deficits in SV recruitment processes (Fig. 5 D).

We then subjected NMJs of larvae expressing RIM-BPΔNTR2^{GFP} in a *rim-bp* null mutant background to electrophysiological analysis to test for functional consequences of the RIM-BP N-terminal truncation. Single-action potential-evoked release was slightly but significantly reduced for the RIM-BPΔNTR2^{GFP}-expressing larvae compared with the control rescue situation (Fig. 6, A–C; same experiment as in Fig. S4, C–F; therefore, same controls). At the same time, no change of short-term facilitation behavior was observed, very different from the *rim-bp* mutant, which, as expected (Liu et al., 2011), showed dramatic facilitation (Fig. 6 D). We observed a similar but less pronounced trend upon expressing the RIM-BPΔNTR1^{GFP} construct in the *rim-bp* null mutant, with the single-action potential-evoked charge being slightly, although not significantly, reduced (Fig. S8, A–C). Short-term facilitation was again unaffected (Fig. S8 D), while the quantal content showed a significant reduction (Fig. S8 E). Based on these data, the RIM-BP NTR obviously plays no major role in the coupling of SVs to release machinery and Ca^{2+} channels.

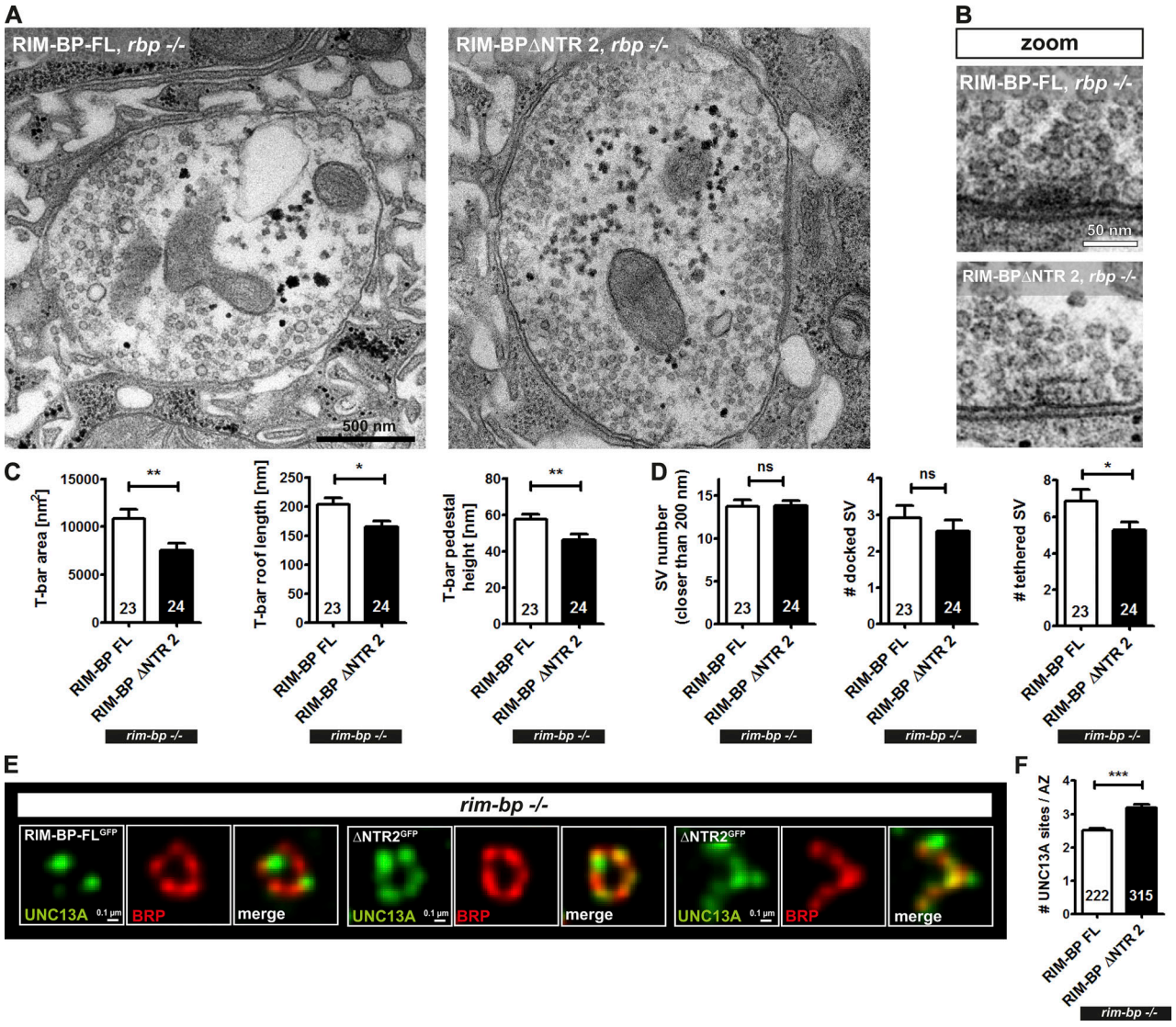

Figure 5. **RIM-BP NTR required for AZ architecture and SV tethering on ultrastructural level. (A–D)** Electron micrographs of *Drosophila* third instar NMJ boutons reexpressing the RIM-BP-FL (A, left panel) or the RIM-BPΔNTR2^{GFP} construct (A, right panel) in the *rim-bp* mutant and zoom of a representative single T-Bar (B). Scale bar, 500 nm for whole bouton and 50 nm for zoom. **(C)** T-bar structural quantification of the representative images shown in A and B. T-bar area (left panel): RIM-BP-FL 10,830 ± 969.1 nm^2, *n* = 23; RIM-BPΔNTR2^{GFP} 7,548 ± 741.4 nm^2, *n* = 24; T-bar roof length (middle panel): RIM-BP-FL 203.4 ± 11.08 nm, *n* = 23; RIM-BPΔNTR2^{GFP} 164.7 ± 10.33 nm, *n* = 23; T-bar pedestal height (right panel): RIM-BP-FL 57.41 ± 2.82 nm, *n* = 23; RIM-BPΔNTR2^{GFP} 46.41 ± 2.82 nm, *n* = 23. Scale bar, 500 nm. **(D)** SV quantification of the representative images shown in A and B. SV number in a range of 200 nm around the AZ center (left panel): RIM-BP-FL 13.74 ± 0.78, *n* = 23; RIM-BPΔNTR2^{GFP} 13.79 ± 0.67, *n* = 24; number of AZ-docked SVs (middle panel): RIM-BP-FL 2.91 ± 0.34, *n* = 23; RIM-BPΔNTR2^{GFP} 2.54 ± 0.31, *n* = 24; number of T-bar tethered SVs (right panel): RIM-BP-FL 6.87 ± 0.63, *n* = 23; RIM-BPΔNTR2^{GFP} 5.25 ± 0.44, *n* = 24. For C and D, all graphs show ± SEM. Data distribution is normal following the D'Agostino and Pearson omnibus normality test. An unpaired, two-sided *t* test was applied, *, P < 0.05; **, P < 0.01; ***, P < 0.001; ns = not significant. All numbers represent the number of quantified T-bars/SVs at a T-bar of four to six animals. **(E)** Representative STED images of *Drosophila* third instar single AZs reexpressing the RIM-BP FL (left panel) or the RIM-BPΔNTR2^{GFP} construct in the *rim-bp* mutant (correctly formed AZ middle panel and deformed AZ right panel). AZ are immunostained for UNC13A (green) and BRP (red). Scale bar, 0.1 µm. **(F)** Quantification of representative data shown in E (RIM-BP-FL^{GFP}: 2.50 ± 0.07, *n* = 15 NMJs from three animals, a total of 222 AZs counted; RIM-BPΔNTR2^{GFP} 3.18 ± 0.11, *n* = 12 NMJs from three animals, a total of 315 AZs counted). All graphs show ± SEM. Data distribution is normal following the D'Agostino and Pearson omnibus normality test. An unpaired, two-sided *t* test was applied, ***, P < 0.001. N represents a single AZ. Three animals are analyzed with two or three NMJs/animal and one to three boutons/NMJ to reach ∼100–300 AZ/genetic condition.

We then used variance mean analysis of synaptic responses (Clements and Silver, 2000; Liu et al., 2011; Sakaba et al., 2002; Silver, 2003) to further dissect the release function after eliminating the RIM-BP NTR. Thus, we determined the mean amplitude and variance of the eEJCs in a two-electrode voltage clamp mode at Ca^{2+} concentrations between 0.75 and 6 mM (Fig. 6 F) and calculated vesicular release probabilities at the Ca^{2+} concentrations used, applying parabolic fits (Fig. 6 G). The SV release probability was indeed unchanged in the mutants compared with the control over the whole range of concentrations tested (Fig. 6 H), again emphasizing that SV-Ca^{2+} channel coupling is obviously undisturbed. Extrapolation of

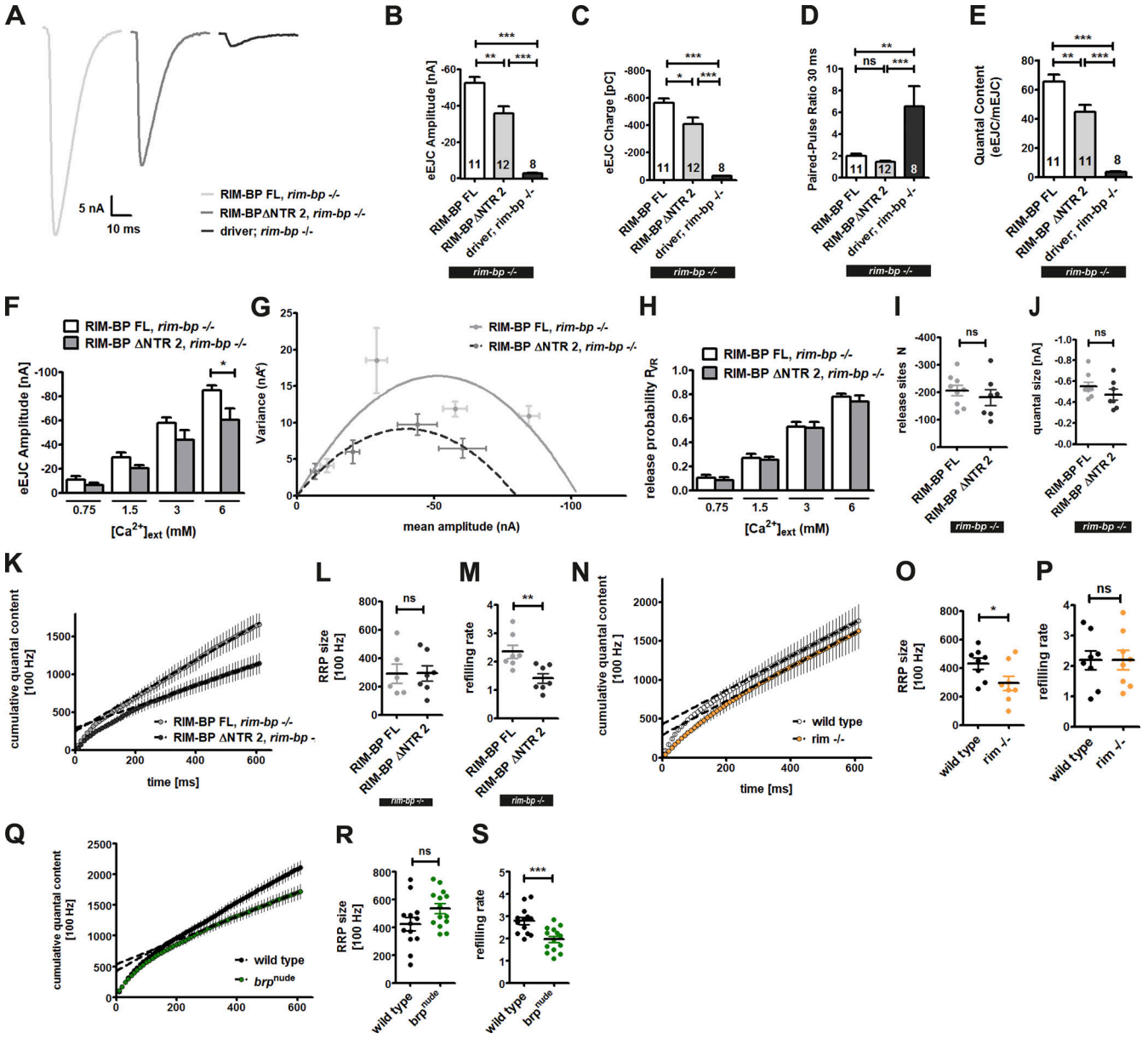

Figure 6. **Physiological evidence for the RIM-BP NTR to promote SV recruitment. (A–E)** Two-electrode voltage clamp electrophysiological recordings of *Drosophila* third instar larvae reexpressing the RIM-BP-FL^{GFP}, the RIM-BPΔNTR2^{GFP} construct and driver control all in the *rim-bp* mutant. **(A)** Example traces of evoked EJC. **(B)** eEJC amplitudes (RIM-BP-FL^{GFP} -52.73 ± 3.17 nA, *n* = 11; RIM-BPΔNTR2^{GFP} −35.76 ± 4.03 nA, *n* = 12; *rim-bp* mutant −2.86 ± 0.31 nA, *n* = 8), **(C)** Evoked excitatory junctional charge (RIM-BP-FL^{GFP} −564.3 ± 31.45 pC, *n* = 10; RIM-BPΔNTR2^{GFP} −411.0 ± 45.83 pC, *n* = 12; *rim-bp* mutant −29.36 ± 2.03 pC, *n* = 8; same experiment as in Fig. S4, C–F, therefore same controls). **(D)** 30 ms paired-pulse ratio (RIM-BP-FL^{GFP} 1.96 ± 0.21, *n* = 11; RIM-BPΔNTR2^{GFP} 1.44 ± 0.11, *n* = 12; *rim-bp* mutant 6.53 ± 1.83, *n* = 8). **(D)** Quantal content (RIM-BP-FL^{GFP} 65.48 ± 4.6, *n* = 11; RIM-BPΔNTR2^{GFP} 44.63 ± 4.73, *n* = 11; *rim-bp* mutant 3.29 ± 0.38, *n* = 8). **(B–E)** All graphs show ± SEM. Data distribution is normal following the D'Agostino and Pearson omnibus normality test. A one-way ANOVA using Tukey post-test was applied, *, P < 0.05, **, P < 0.01, ***, P < 0.001, n.s. = not significant. N represents a single cell. Four to six animals are analyzed with one or two cells/animal. **(F–J)** Two-electrode voltage clamp electrophysiological recordings of *Drosophila* third instar larvae reexpressing the RIM-BP-FL^{GFP} or the RIM-BPΔNTR2^{GFP} construct in the *rim-bp* mutant. **(F)** eEJC amplitudes at several c$[Ca^{2+}]_{ext}$ (0.75 mM: RIM-BP-FL^{GFP} −10.9 ± 2.61 nA, *n* = 9; RIM-BPΔNTR2^{GFP} −6.38 ± 1.75 nA, *n* = 7. 1.5 mM: RIM-BP-FL^{GFP} −29.03 ± 4.09 nA, *n* = 9; RIM-BPΔNTR2^{GFP} −20.21 ± 2.75 nA, *n* = 7. 3.0 mM: RIM-BP-FL^{GFP} −57.65 ± 4.55 nA, *n* = 9; RIM-BPΔNTR2^{GFP} −43.8 ± 7.76 nA, *n* = 7. 6.0 mM: RIM-BP-FL^{GFP} −84.59 ± 4.0 nA, *n* = 9; RIM-BPΔNTR2^{GFP} −60.31 ± 9.28 nA, *n* = 7). **(G)** Parabolic fit for variance-mean analysis. **(H)** Vesicular release probability P_{VR} (0.75 mM: RIM-BP-FL^{GFP} 0.10 ± 0.03, *n* = 9; RIM-BPΔNTR2^{GFP} 0.08 ± 0.03, *n* = 7. 1.5 mM: RIM-BP-FL^{GFP} 0.27 ± 0.04, *n* = 9; RIM-BPΔNTR2^{GFP} 0.25 ± 0.03, *n* = 7. 3.0 mM: RIM-BP-FL^{GFP} 0.53 ± 0.04, *n* = 9; RIM-BPΔNTR2^{GFP} 0.52 ± 0.05, *n* = 7. 6.0 mM: RIM-BP-FL^{GFP} 0.78 ± 0.02, *n* = 9; RIM-BPΔNTR2^{GFP} 0.74 ± 0.05, *n* = 7). **(F and H)** All graphs show ± SEM. Data distribution is normal following the D'Agostino and Pearson omnibus normality test. An unpaired, two-sided *t* test was applied, *, P < 0.05. N represents number of animals tested. **(I)** Number of release sites (RIM-BP-FL^{GFP} 205.6 ± 18.98, *n* = 9; RIM-BPΔNTR2^{GFP} 180.6 ± 28.82, *n* = 7). Graph shows ± SEM. Data distribution is normal following the D'Agostino and Pearson omnibus normality test. An unpaired, two-sided *t* test was applied, ns = not significant. N represents number of animals tested. **(J)** Quantal size (RIM-BP-FL^{GFP} −0.55 ± 0.04 nA, *n* = 9; RIM-BPΔNTR2^{GFP} -0.48 ± 0.05 nA, *n* = 7). Graph shows ± SEM. Data distribution was not normal following the D'Agostino and Pearson omnibus normality test. We therefore applied the nonparametric two-tailed Mann–Whitney test, ns = not significant. N represents number of animals tested. **(K, N, and Q)** Back extrapolation of cumulative quantal content in high-frequency stimulated larvae (K) RIM-BP-FL^{GFP} and RIM-BPΔNTR2^{GFP} in the *rim-bp*

mutant background, (N) WT and *rim* mutant, (Q) WT and *brp* ^{nude}. **(L, O, and R)** Size of the readily releasable pool (RRP) of SVs (L) RIM-BP-FL^{GFP} and RIM-BPΔNTR2^{GFP} in the *rim-bp* mutant background (RIM-BP-FL^{GFP} 291 ± 67.37, *n* = 6; RIM-BPΔNTR2^{GFP} 292.8 ± 53.75, *n* = 7), (O) WT and *rim* mutant (WT 430.5 ± 39.09, *n* = 8; *rim* mutant 292.8 ± 48.92, *n* = 8), (R) WT and *brp*^{nude} (WT 423.7 ± 47.64, *n* = 13; *brp*^{nude} 534.2 ± 35.28, *n* = 14). **(M, P, and S)** Refilling rates (M) RIM-BP-FL^{GFP} and RIM-BPΔNTR2^{GFP} in the *rim-bp* mutant background (RIM-BP-FL^{GFP} 2.35 ± 0.23, *n* = 7; RIM-BPΔNTR2^{GFP} 1.41 ± 0.17, *n* = 7), (P) WT and *rim* mutant (WT 2.18 ± 0.31, *n* = 8; *rim* mutant 2.19 ± 0.32, *n* = 8), (S) WT and *brp*^{nude} (WT 2.79 ± 0.17, *n* = 13; *brp*^{nude} 1.96 ± 0.15, *n* = 14). **(L, M, O, P, R, and S)** All graphs show ± SEM. Data distribution is normal following the D'Agostino and Pearson omnibus normality test. An unpaired, two-sided *t* test was applied, *, P < 0.05; **, P < 0.01; ***, P < 0.001; n.s. = not significant. N represents a single cell. Four to six animals are analyzed with one or two cells/animal.

release site number N (Fig. 6 I) and quantal size (Fig. 6 J) showed slight reductions for the RIM-BPΔNTR2^{GFP}-expressing situation. Taken together, no signs of defective Ca^{2+} channel/SV coupling could be observed after eliminating the NTR in two assays, consistent with the SH3 domains (but not the NTR) binding to Ca^{2+} channels and the Unc13A release factor. Considered together, the RIM-BP NTR, though critical for proper bundling of the BRP-based AZ scaffold, is obviously largely dispensable for SV/Ca^{2+} channel coupling and molecular release site definition.

The RIM-BP NTR promotes vesicle recruitment

The BRP-based T-bar scaffold has been implicated in the activity-dependent recruitment of SVs into the SV releasable pool, which involves the tethering of SVs to the membrane-distal ends of the BRP filaments forming the T-bar "roof" (Hallermann et al., 2010b). As has already been mentioned above, the number of SVs tethered to the distal T-bar was significantly reduced in the absence of the NTR (Fig. 5 D). We therefore asked whether the dynamic recruitment of SVs in episodes of increased release would depend on the RIM-BP NTR2 (Fig. 6, K–M). Accordingly, we subjected the RIM-BPΔNTR2^{GFP} rescue larvae to trains of 60 Hz and plotted cumulative quantal contents. Back extrapolation to the y axis allowed for the determination of release-ready vesicle pool (RRP) sizes, while the slopes gave refilling rates (Fig. 6 K; extrapolated straight lines are indicated in the graph). No significant change of the RRP size was observed (Fig. 6 L). Instead, the SV refilling rate in the course of enhanced SV release was significantly reduced (Fig. 6 M).

To further explore the latter phenotype, we first asked whether RIM-BP–controlled refilling rates might depend on RIM. However, the corresponding *rim* mutant phenotype was rather inverse to that of RIM-BPΔNTR2^{GFP} rescue larvae: the RRP sizes were significantly reduced (Fig. 6, N and O), but refilling rates were unchanged (Fig. 6 P). Elimination of RIM in isolation thus seemingly plays no major role in the recruitment of SVs into release sites, at least not at the NMJ synapse. The RIM-BP NTR, while not playing a major role in release site function and definition, seems to take part in a rate-limiting step of recruiting SVs into their release sites at the base of the AZ scaffold.

Notably, BRP has been implicated in RRP refilling previously, based on a specific mutation (*brp*^{nude}) that deletes only the last 17 amino acids of the membrane-distal C terminus of BRP (Hallermann et al., 2010b). Interestingly, refilling rates were reduced similarly in *brp*^{nude} as in the RIM-BPΔNTR2^{GFP} rescue larvae (Fig. 6, Q–S).

RIM-BP might connect release sites with scaffold-based SV recruitment

Our recent analysis provided evidence for discrete Unc13A clusters operating as SV release sites (Böhme et al., 2016; Reddy-Alla et al., 2017). These Unc13A clusters group physically around the AZ central Ca^{2+} channel cluster with an average distance of ∼70 nm from the AZ and Ca^{2+} channel cluster center at planar STED-imaged AZs (Böhme et al., 2016). The extended BRP protein converges from the membrane-distal C terminus to the membrane-proximal N terminus in a funnel-like manner, with the C termini grouping around the AZ center in planar projections at a distance of ∼100 nm. The BRP N termini, instead, overlay the Ca^{2+} channels in the AZ center directly, consistent with the probable role of BRP in Ca^{2+} channel clustering, redundant to RIM-BP (see Discussion).

Our findings that the RIM-BP SH3-II/III domains bind release effectors physically, among them Unc13A, while the RIM-BP NTR binds a region of BRP, suggest that RIM-BP, due to its conserved architecture, might functionally bridge BRP-associated SV recruitment to the Unc13A-dependent SV release sites. We therefore analyzed the nanoscopic distribution of RIM-BP epitopes at planar imaged AZs. The RIM-BP C termini localized toward the outer BRP C termini (Fig. 7 A, upper panel) and, thus, in the direction of the Unc13A clusters. The RIM-BP NTR epitope, instead, was positioned more toward the AZ center and partially colocalized with the BRP N-terminal epitope (Fig. 7 A, middle and lower panels). Line profiles of single AZs show larger rings for the RIM-BP C-terminal than the RIM-BP N-terminal epitope (Fig. 7 B, upper panel). Quantification of the peak-to-peak distances revealed a significant ring diameter difference (Fig. 7 C). The quantified numbers are depicted on a top view model of the AZ (Fig. 7 D), showing that RIM-BP^{Nterm} and BRP^{Nterm} are in close proximity, consistent with both NTRs being in stable physical contact, as indicated by our Y2H and in vivo cross-linking data (Fig. 1). Thus, our nanoscopic analysis suggests a functional architecture in which BRP filaments guide SVs into SV release slots, and RIM-BP might represent a relay factor that bridges between BRP and release sites functionally and topologically.

Discussion

Our current view of AZ scaffolds emphasizes their role in providing a "smart catalytic surface" integrating sub-functionalities that facilitate and control the SV cycle. Providing SV release sites with a proteinaceous "nano-environment" defining release probability, by precisely defining their spatial distance to voltage-operated Ca^{2+} channels, is probably one fundamental function using these highly conserved, "ancient" protein architectures. The SV release sites probably also have to be coupled to processes retrieving SVs from more membrane-distant positions. Concerning protein architectures harvesting SVs, evolutionary solutions might have been somewhat more flexible,

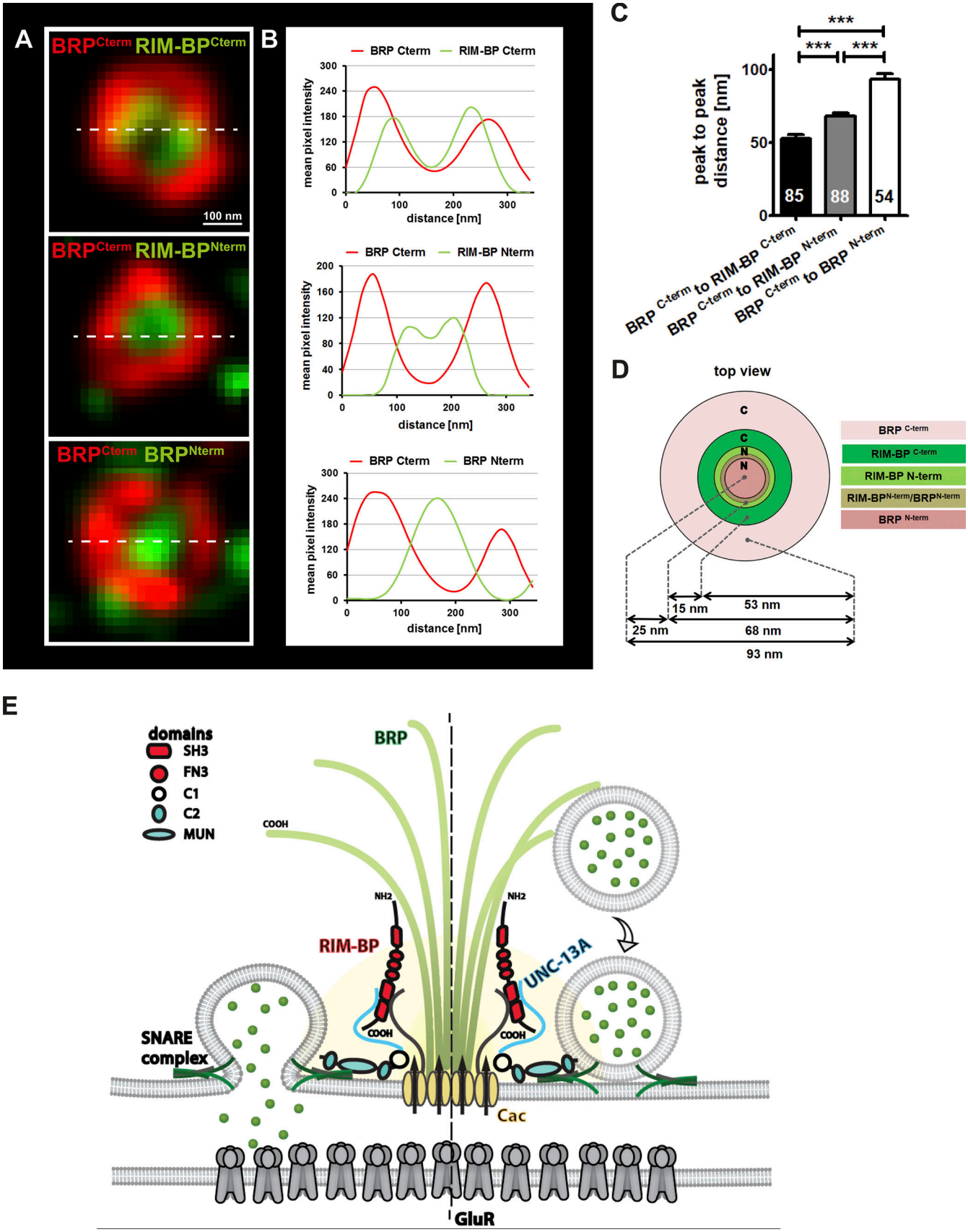

Figure 7. **RIM-BP NTR localizes to the center of the AZ to stabilize the BRP scaffold and promote SV recruitment. (A–D)** RIM-BP^{Nterm} localizes (A and B, middle panel) closer to the center of the AZ than the RIM-BP^{Cterm} (A and B, upper panel), where it might interact with the BRP$^{N\text{-}term}$ (A and B lower panel) as

shown by the Y2H (see Fig. 1 A). **(A)** Representative STED images of WT *Drosophila* third instar single AZs immunostained for RIM-BP^{Cterm} (green) and BRP^{Cterm} (red; upper panel), RIM-BP^{Nterm} (green) and BRP^{Cterm} (red; middle panel) and BRP^{Nterm} (green) and BRP^{Cterm} (red; lower panel). Scale bar, 100 nm. **(B)** Line profiles from the dashed white line in A. **(C)** Quantification of the distances between BRP^{Cterm}/RIM-BP^{Nterm}, BRP^{Cterm}/RIM-BP^{Cterm}, and BRP^{Nterm}/BRP^{Cterm}, showing that RIM-BP^{Cterm} is close to distant BRP^{Cterm} and RIM-BP^{Nterm} is close to the central BRP^{Nterm}. BRP^{Cterm} to RIM-BP^{Cterm} 52.64 ± 2.56, n = 85 AZs, BRP^{Cterm} to RIM-BP^{Nterm} 67.86 ± 2.50, n = 88 AZs, BRP^{Cterm} to BRPN^{term} 93.03 ± 3.96, n = 54 AZs. All graphs show ± SEM. Data distribution is normal following the D'Agostino and Pearson omnibus normality test. A one-way ANOVA was applied using Tukey post-test; ***, P < 0.001. N represents single AZ from three animals with two or three NMJs/animal and one or two boutons/NMJ. **(D)** Schematic representation of the AZ from a top view indicating the distances between RIM-BP/BRP termini from C. **(E)** Model of the AZ scaffold. See text for explanation.

obviously adopted to the synapse-type specific needs in physiologically relevant fusion rates. Identifying proteins that might be involved in structurally and functionally coupling recruitment protein architectures with release sites is an emerging topic. We here provide evidence that RIM-BP with its interactions obviously plays a role in both "nanoscopic locations." First, through its SH3 domains, it binds RIM, the intercellular C-terminus of the voltage-operated Ca^{2+} channel and also Unc13A, the release factor whose nanoscale positioning we recently identified as critical for SV release definition (Reddy-Alla et al., 2017). Second, we found here that it also binds conserved regions of BRP in the core of the AZ central scaffold. Deleting this interaction surface, though not reducing AZ protein levels, obviously undermines the proper bundling of BRP filaments, at least for a major fraction of AZs. Though it is not easy to prove that individual RIM-BP protein molecules span this distance physically, it is tempting to hypothesize that RIM-BP might literally connect the recruitment of SVs from more membrane distant pools, probably starting at the distal end of the BRP filaments, with their integration into SV release sites (see model, Fig. 7 E).

Differentiating subfunctions of RIM-BP for release and AZ assembly

At mammalian synapses, recent multi-loci genetics have demonstrated most severe deficits when eliminating combinations of AZ scaffold proteins between RIM, ELKS, and RIM-BP family members (Acuna et al., 2016; Wang et al., 2016). Here, quadruple knockouts of RIM1/2, together with RIM-BP1/2 proteins in mice, exhibit a total loss of neurotransmitter release from severe impairments in SV priming and docking, a dramatic loss of AZ scaffold density, with a trans-synaptic effect that impairs the organization of the postsynaptic density (Acuna et al., 2016). These severe synthetic "catastrophic" phenotypes, eliminating ultrastructural specializations and release factor targeting, demonstrate a principal functional redundancy between RIM-BPs, RIMs, and ELKS family proteins. Similar results were also retrieved from work on mice in which RIM1αβ and RIM2αβγ, together with ELKS1α and ELKS2α isoforms, have been completely eliminated. Cultured hippocampal synapses of these mutant mice consequently lose Munc13, Bassoon, Piccolo, and RIM-BP, following a mass disassembly of the AZ scaffold (Wang et al., 2016). Similarly, in this study, we observed that RIM seemingly operates synergistically with RIM-BP in establishing the AZ nanoscopic architecture (Fig. 6, K and L).

Despite the obvious importance of these findings for understanding the collective role of the AZ scaffold, the fact that the domain organization for all specific scaffold proteins has been individually conserved over hundreds of millions of years motivated us to search for ways to demonstrate specific functions of these AZ core scaffold proteins. We here molecularly isolated an additional sub-functionality for the so-far functionally non-considered RIM-BP NTR, and provide evidence that its protein architecture might have been conserved for the reason that it operates as an adaptor coupling SV recruitment processes with the membrane-associated SV release sites.

Mechanistic analysis of RIM-BPs so far has largely focused on SH3 domains II and III, which bind to Ca^{2+} channels and RIM in both mammals and *Drosophila* (Acuna et al., 2015; Hibino et al., 2002; Liu et al., 2011; Wang et al., 2002), and Unc13A in *Drosophila* (Böhme et al., 2016). Analysis of RIM-BP at *Drosophila* NMJ synapses was the first to demonstrate a major role of the protein family in neurotransmission (Liu et al., 2011), characterized by a severe reduction in release probability and signs of defective Ca^{2+} channel clustering. We here exploit the glutamatergic NMJ synapses for a stringent genetic analysis with multimodal readouts, also including an analysis of transport and nanoscale integration into the AZ scaffold. Deletion of individual SH3 domains majorly affected RIM-BP transport, probably directly reflecting their high affinity binding to JIP-1 homologue Aplip1, whose deletion also interferes with effective axonal transport of BRP/RIM-BP "packages" (Siebert et al., 2015). Somewhat surprisingly, however, moderately or even strongly reduced levels of RIM-BPΔSH3-II or RIM-BPΔSH3-III, respectively, still restored RIM-BP functionality when expressed in a null background. It obviously might be argued that only combined elimination of SH3-II together with SH3-III might uncover their function collectively. Indeed, Aplip1 binds both SH3-II and III, and AZ levels were decreased even more strongly in the RIM-BPΔSH3-II/III double-deleted variant. However, at least concerning the role of Ca^{2+} channel binding, the AZ scaffold can seemingly compensate for the absence of RIM-BP-SH3 mediated interactions, as Ca^{2+} channels with the highly conserved PXXP RIM-BP binding motif deleted still retained full activity in a genetic rescue assay (instead of resembling the *rim-bp* null phenotype). We suggest that redundant interactions stabilize Ca^{2+} channel: AZ scaffold contacts at NMJ synapses, an idea that might be relevant for other synapses as well. Indeed, we showed previously that the N terminus of BRP also binds the Ca^{2+} channel α1 subunit intracellular C terminus (Fouquet et al., 2009). Given the essential character of SH3-III for survival, however, it appears likely that slightly different rules and "vulnerabilities" apply to other synapse types, for example, in the *Drosophila* brain. In fact, we have found lately that synapses in the *Drosophila* brain differ substantially in their BRP content, with, for example, interneuron synapses largely lacking BRP

(Fulterer et al., 2018). This might result in different efficacy of compensation via BRP and be responsible for the essential character of SH3-III. Put differently, it still appears plausible that the C-terminal close SH3 domains might be of truly essential character dependent on synapse type given the results retrieved at mammalian synapses (Acuna et al., 2015; Grauel et al., 2016; Kaeser et al., 2011).

Finally, the presence of three FN-III domains, despite their invariable character, remained and remains an enigma. FN-III modules are common in extracellular but rarer in intracellular proteins, such as RIM-BP, here found chiefly as the main components of a group of intracellular proteins associated with the contractile apparatus of muscles. The first x-ray structure of the RIM-BPs, which we can present here, depicts a typical FN-III-type organization; however, it is oriented in an extended hinge-like arrangement. It is tempting to speculate that the hinge-like architecture might support RIM-BP conformations or conformational change when connecting release sites with recruitment processes.

RIM-BP: A generic adaptor to couple SV replenishment with SV release sites?

Our physiological analysis points toward a discrete function of the RIM-BP N-terminal domain. Analysis of SV recruitment based on the *rim-bp* null allele is complicated due to the severe release probability deficits dominating the physiological scenario. Nonetheless, a careful analysis, using high Ca^{2+} concentrations to milden the influence of release probability differences, indeed identified recruitment defects (Müller et al., 2015). Remarkably, similar to our NTR-specific deletions, a previous study analyzing the *rim-bp* null mutant (Müller et al., 2015) for RIM-BP suggested a rate-limiting function for the replenishment of high release probability SVs following vesicle depletion at NMJ synapses. Moreover, in mouse *rim-bp2* knockouts, recruitment/replenishment deficits at auditory hair cells were reported (Krinner et al., 2017). In *rim-bp* null mutants, UNC13A levels are strongly reduced (Böhme et al., 2016), while for the dNTR-2 construct, UNC13A levels and consequently release site number were not reduced (instead rather slightly increased). Thus, our data apparently uncouple the role of RIM-BP for release site organization (via Unc13A clustering) from its role in overall scaffold organization where the NTR plays an important role.

The extended BRP filaments in *Drosophila* probably operate as "antennae" to harvest SVs from the reserve pool, a process facilitated by the C-terminal amino acids of BRP, made evident by the defects of the brp^{nude} allele lacking only the last 17 amino acids (Hallermann et al., 2010b). BRP in its first half is highly homologous to ELKS/CAZ-associated structural proteins (CAST) AZ proteins; however, its C-terminal half is specific for insects and obviously evolved here for harvesting SVs. The large vertebrate-specific AZ protein Bassoon was shown to help SV replenishment at the central synapse under conditions of heavy stimulation (Hallermann et al., 2010a). Notably, Bassoon binds to the first SH3 domain of RIM-BP (Davydova et al., 2014), suggestive of convergent evolution where different molecular antennae were used to finally target RIM-BP, the generic "old" adaptor coupling to the membrane close release sites.

In its current form, static STED microscopy as used here only samples average epitope distributions, while the relevant proteins likely are dynamically switched in the course of the SV cycle. As an indication of this, the RIM-BP C-terminal SH3 domains were found to bind both the Ca^{2+} channel C-terminus and Unc13A N terminus (Böhme et al., 2016). As these binding events can hardly be accomplished by a single Unc13A molecule at a single time point, future analysis will have to address the underlying conformational dynamics likely involved here.

Taken together, RIM-BPs might take a generic role of SV replenishment, apart from their obvious role in coclustering of release machinery and Ca^{2+} channels at the AZ membrane. Indeed, the highly conserved domain architecture might have evolved for exactly this reason, to guide SVs into the proper release environment.

Materials and methods

Cloning and mutagenesis

Generation of the RIM-BP deletion constructs

The full-length d*rbp* cDNA (according to isoform F) has been obtained via PCR using a forward primer with additional 4 bp (CACC; see Table 1) and then ligated into pENTR-dTOPO (Invitrogen) according to the manufacturer's instructions. Finally, pENTR-dTOPO-*rim-bp* FL was recombined with pUAST-attB-rfa-EGFP using the Gateway System (Invitrogen) to yield pUAST-attB-*rim-bp* FL-*EGFP*. After confirmation by double-strand sequencing, transgenic flies were generated using the PhiC31 system with defined landing sites in the *Drosophila* genome.

All additional domain deletions of RIM-BP were generated by using the pENTR-dTOPO-*rim-bp* FL as a template and overlapping primers in a self sequence– and ligation-independent cloning strategy (SLIC; Li and Elledge, 2012) approach (primer sequences, see Table 1). The following amino acids were deleted: RIM-$BP^{\Delta FN\text{-}III(1)}$ 747–826 aa, RIM-$BP^{\Delta FN\text{-}III(2)}$ aa 837–938, RIM-$BP^{\Delta FN\text{-}III(3)}$ 951–1030 aa, RIM-$BP^{\Delta SH3\text{-}I}$ 606-681aa, RIM-$BP^{\Delta SH3\text{-}II}$ 1318–1382 aa, RIM-$BP^{\Delta SH3\text{-}III}$ 1445-1509aa, RIM-$BP^{\Delta SH3\text{-}II+III}$ 1318-1509aa, RIM-$BP^{SH3\text{-}II+III}$ 1318-1509aa, RIM-$BP^{SH3\text{-}III}$ 1445-1509aa, for NTRs RIM-$BP^{\Delta NTR1}$ and RIM-$BP^{\Delta NTR2}$.

The cloning strategy for the generation of RIM-$BP^{\Delta NTR1(26–250)}$. For the amplification of the first fragment (A), the primer pair Fwd_1 and Rev_1 was used. For the amplification of the second fragment (B), the primer pair Fwd_2 and Rev_2 (see Table 1) was used. For annealing of fragments (A and B), the Invitrogen Elongase Enzyme Mix kit was used with the primer pair combination of Fwd_1 and Rev_2. Domain deletions of RIM-BP were generated by using overlapping primers in a SLIC (Li and Elledge, 2012) approach with RIM-BP^{FL} as a template. Through Gateway reaction, all RIM-BP deletion constructs were shuttled into GAL4/UAS vector (pUAST) containing a C-terminal EGFP tag. After sequencing, the constructs were injected into an attP site containing fly strain (y1 w1118; PBac{y+-attP-3B} VK00002; Bloomington *Drosophila* Stock Center line 9723) using the services of BestGene Inc.

Table 1. **Used primer sequences of this study**

Construct	Primers	Sequence (5′→3′)
RIM-BP^{FL}	Fwd	CACCATGCATTTATGTGAATTTCCCAGCGC
	Rev	GTATTTGCCAAAGCCGAACCCGAATTTTC
RIM-BP$^{\Delta NTR1(26-250)}$	Fwd_1	GATCGGCGCGCCATGCATTTATGTGAATTTCCCAGCGC
	Rev_1	CGCTTCCTCCCAGAACTGCTCTTTTTGCTGCTGCTGCTGCTTTTTCAGG
	Fwd_2	CCTGAAAAAGCAGCAGCAGCAGCAAAAAGAGCAGTTCTGGGAGGAAGCGG
	Rev_2	GATCGAGCTCGCCCTCAGCCTCCCTGCAAGG
RIM-BP$^{\Delta NTR2(152-599)}$	Fwd_3	ATCCCGCTCGGATATTCCTGGAAAGGGCCG
	Rev_3	CAGGAATATCCGAGCGGGATGCCTG
RIM-BP$^{\Delta SH3I(606-681)}$	Fwd_4	TGGAAAGGGCGACCTCCTGGAGTTCCACC
	Rev_4	CCAGGAGGTCGCCCTTTCCAGGAATATCGAG
RIM-BP$^{\Delta SH3II(1318-1382)}$	Fwd_5	GAAGAAGCCCGACACCACCGCCTCC
	Rev_5	TGTACTGGTCGGGCTTCTTCTGTGCTCCGGG
RIM-BP$^{\Delta SH3III(1445-1509)}$	Fwd_6	CATGCCCGTGGCGCCCGACCAGTACAAC
	Rev_6	GCGCCCGACCAGCACGGGCATGTTGGC
RIM-BP$^{\Delta FN3\ I(747-826)}$	Fwd_7	CAGCGACAATCGGGATGCCGCCTGC
	Rev_7	CGGGATGCCGATTGTCGCTGATGTCG
RIM-BP$^{\Delta FN3\ II(837-938)}$	Fwd_8	GATCATCGGGGACTTCCGCACCCTCACCAAG
	Rev_8	GGCCCTTGGTCCCGATGATCATCGTGC
RIM-BP$^{\Delta FN3\ III(951-1030)}$	Fwd_9	CAAGGGCCTGGCGGACAGTGCGC
	Rev_9	GCGGACAGTGCAGGCCCTTGG
RIM-BP$^{SH3\ II\ +\ III\ OE(1317-1509)}$	Fwd_10	GAAGAAGCCCGACCAGTACAACAACCAGATGG
	Rev_10	TGTACTGGTCGGGCTTCTTCTGTGCTCCGGG

Generation of the RIM-BP-RNAi

RIM-BP-RNAi constructs were cloned into the pWalium20 vector following the Harvard Medical School TRIP protocol and injected into the Bloomington line 9744-VK27 and balanced over CyO (BestGene). 71-nucleotide primers were synthesized using isoform-specific primers: RBP2-Fw: 5′-CTAGCAGTGGGCACC GACAATCAGCCACCTAGTTATATTCAAGCATAGGTGGCTGAT TGTCGGTGCCCGCG-3′ and RBP2-Rv: 5′-AATTCGCGGGCACCG ACAATCAGCCACCTATGCTTGAATATAACTAGGTGGCTGATT GTCGGTGCCCACTG-3′.

Generation of modified and P(acman)-cac-apta construct

The mutation of second PXXP motif at position 1690,1693 to APTA was cloned according to the Counter Selection BAC Modification kit obtained from Gene Bridges GmbH.

The rpsL-neomycin (neo) template DNA was used to generate selectable cassettes. The primers consisted of 50-bp homology regions and a sequence for the amplification of the rpsL-neo counter selection cassette. The selectable cassettes were generated in a proofreading PCR with Vent Polymerase (New England Biolabs, Inc.) and the following primer pairs: fw: 5′-GTGTAACGCATGTACAGCATAGTTACC CAACACTGGCCTCCCGAAGAGCCGGCCTGGTGATGATGG CGGGATCG-3′, and rv: 5′-GTGTGGGACTGGCATTCAGCTTCGG GAAATTGATATTGGTTGGCTTGATCAGAAGAACTCGTCAAG AAGGCG-3′.

APTA point-mutated cac cDNA was used as a template to generate selectable cassettes. The selectable cassettes were generated in a proofreading PCR with Vent Polymerase (New England Biolabs, Inc.) and the following primer pairs: 5′-GTG TAACGCATGTACAGCATAG-3′ and 5′-ATGTGTGGGACTGGC ATTCAG-3′.

All cac constructs were injected into an attP site containing fly strain (PBac {y[+]-attP-3B}VK00033; Bloomington *Drosophila* Stock Center line 9750) using the services of BestGene Inc.

Cloning and mutagenesis

Generation of the RIM-BP deletion constructs

The full-length d*rbp* cDNA (according to isoform F) domain deletions of RIM-BP were generated by using overlapping primers in a SLIC (Li and Elledge, 2012) approach, the gateway cloning system, or conventional cloning (contact the authors for exact cloning strategies and primers). The following aa were deleted: RIM-BP$^{\Delta FN\text{-}III(1)}$ 747–826 aa, RIM-BP$^{\Delta FN\text{-}III(2)}$ aa 837–938, RIM-BP$^{\Delta FN\text{-}III(3)}$ 948–1030 aa, RIM-BP$^{\Delta SH3\text{-}I}$ 606-681aa, RIM-BP$^{\Delta SH3\text{-}II}$ 1318–1382 aa, RIM-BP$^{\Delta SH3\text{-}III}$ 1445-1509aa, RIM-BP$^{\Delta SH3\text{-}II+III}$ 1318-1509aa, RIM-BP $^{SH3\text{-}II+III}$ 1318-1509aa, RIM-BP $^{SH3\text{-}III}$ 1445-1509aa, for NTRs RIM-BP$^{\Delta 26\text{-}250}$ and RIM-BP$^{\Delta 152\text{-}599}$. Through Gateway reaction, all RIM-BP deletion constructs were shuttled into GAL4/UAS vector (pUAST) containing a C-terminal EGFP tag. After sequencing, the constructs were injected into an attP site containing fly strain (y1 w1118; PBac{y+-attP-3B}VK00002;

Bloomington *Drosophila* Stock Center line 9723) using the services of BestGene Inc.

Generation of the RIM-BP-RNAi

RIM-BP-RNAi constructs were cloned into the pWalium20 vector following the Harvard Medical School TRIP protocol (https://fgr.hms.harvard.edu/files/fly/files/2ndgenprotocol.pdf) and injected into the Bloomington line 9744-VK27 and balanced over CyO (BestGene). 71-nucleotide primers were synthetized using isoform-specific primers: RBP2-Fw: 5′-CTAGCAGTGGGC ACCGACAATCAGCCACCTAGTTATATTCAAGCATAGGTGGCT GATTGTCGGTGCCCGCG-3′ and RBP2-Rv: 5′-AATTCGCGGGCA CCGACAATCAGCCACCTATGCTTGAATATAACTAGGTGGCTG ATTGTCGGTGCCCACTG-3′.

Generation of modified and P(acman)-cac-apta construct

The mutation of second PXXP motif at position 1690,1693 to APTA was cloned according to the Counter Selection BAC Modification kit obtained from Gene Bridges GmbH.

The rpsL-neomycin (neo) template DNA was used to generate selectable cassettes. The primers consisted of 50-bp homology regions and a sequence for the amplification of the rpsL-neo counter selection cassette. The selectable cassettes were generated in a proofreading PCR with Vent Polymerase (New England Biolabs, Inc.) and the following primer pairs: fw: 5′-GTGTAA CGCATGTACAGCATAGTTACCCAACACTGGCCTCCCGAAGAG CCGGCCTGGTGATGATGGCGGGATCG-3′, and rv: 5′-GTGTGG GACTGGCATTCAGCTTCGGGAAATTGATATTGGTTGGCTTGA TCAGAAGAACTCGTCAAGAAGGCG-3′.

APTA point-mutated cac cDNA was used as a template to generate selectable cassettes. The selectable cassettes were generated in a proofreading PCR with Vent Polymerase (New England Biolabs, Inc.) and the following primer pairs: 5′-GTG TAACGCATGTACAGCATAG-3′ and 5′-ATGTGTGGGACTGGC ATTCAG-3′.

All cac constructs were injected into an attP site containing fly strain (PBac {y[+]-attP-3B}VK00033; Bloomington *Drosophila* Stock Center line 9750) using the services of BestGene Inc.

Animal rearing and fly strains

Fly strains were reared under standard laboratory conditions at 25°C and 65–70% humidity in incubators. Both male and female larvae were used for analysis in all experiments, except when indicated differently. All pUAST-RIM-BP-GFP constructs were crossed into the WT and into a *rim-bp*^{null} (*Df2.01* and *rim-bp*^{STOP1}) background (Liu et al., 2011) using the UAS-GAL4 expression system (Brand and Perrimon, 1993). The following genotypes were used: WT: +/+ (*w1118*), UAS-RIM-BP-FL^{GFP}; UAS-RIM-BPΔFN-III(1)^{GFP}; UAS-RIM-BPΔFN-III(2)^{GFP}; UAS-RIM-BPΔFN-III(3)^{GFP}; UAS-RIM-BPΔSH3-I^{GFP}; UAS-RIM-BPΔSH3-II^{GFP}; UAS-RIM-BPΔSH3-III^{GFP}; UAS-RIM-BPΔSH3-II^{GFP}+ΔSH3-III^{GFP}; UAS-RIM-BP-SH3-III^{GFP}; UAS-RIM-BP-SH3-II+III^{GFP}; UAS-RIM-BPΔNTR1^{GFP}; UAS-RIM-BPΔNTR2^{GFP}; elaV-Gal4 (C155)/X (Bloomington 458) was used for reexpression of all deletion construct (elaV-Gal4/X;; *rim-bp*^{STOP1}/TM6B); and ok6-Gal4 (Bloomington 64199) was used for expression of the RIM-BP-RNAi (Sigrist laboratory, see above). We used the MIMIC line from Bloomington (60200, MIMIC line, C-terminal genomic EGFP insertion in the PB isoform) for RIM-EGFP, and we used *rim*^{103} as *rim* mutant (Müller et al., 2012)/Df(3R)BSC650 (Bloomington 25740). We used *fife*^{ex1027} as *fife* mutant (Bruckner et al., 2012)/Df(3L)BSC412 (Bloomington 24916). For *brp*^{nude}, see Hallermann et al. (2010b). Deletion constructs were raised at 29°C for IF and STED analysis and at 25°C for viability assay and used protein-rich food (see Liu at al., 2011).

Yeast two-hybrid analyses

The Y2H analyses were performed as described in Böhme et al. (2016) and are summarized here: DNA fragments encoding various regions of RIM-BP, BRP, and Unc13A were each cloned into two bait and two prey vectors (plasmids pACT4-DM and pGAD426-D3 [encoding Gal4 activation domain fusions at the N terminus]). The bait/prey constructs encode for the following proteins: RIM-BP (Isoform F) 1–600 aa; RIM-BP 610–1042 aa; RIM-BP 745–1024 aa; RIM-BP 1040–1328 aa; RIM-BP 1441–1507 aa; RIM-BP 1441–1844 aa; Cacophony (Isoform A) 1500–1848 aa; Unc13 (Isoform A) 1–606 aa; Aplip1 (Isoform B) 1–250 aa; RIM (Isoform P) 1–227 aa; RIM (Isoform P) 1135–1306 aa; Fife (Isoform D) 474–794 aa; and BRP (Isoform G) 100–650 aa. All cDNA fragments encoding the bait protein fragments were subcloned into two gateway-compatible yeast expression vectors, pBTM116-D9 and pBTMcC24-DM, and transformed into the MATa yeast strain L40ccua. Bait and prey constructs that led to autoactivation (transcription of the reporter genes HIS3, URA3) were removed from the analysis. For mating, 25 ml fresh overnight cultures of the bait strains (–Trp/+His +Ade +Ura +Leu) were distributed into 384-well micro titer plates (40 µl each well) using a pipetting robot (Biomek FX, Beckman Coulter). Each single prey yeast colony grown on media containing –Leu/+His +Ade +Ura + Trp was selected and resuspended into a well of the 40-µl bait strains. The pairwise combinations of bait and prey strains were mixed and transferred immediately onto yeast extract peptone dextrose (YPD) agar plates using a spotting robot (KBiosystems) and incubated for 36 h at 30°C. For detection of protein–protein interactions, diploid yeasts carrying both baits and preys were spotted from YPD agar to synthetic dropout IV media that lacked tryptophan, leucine, histidine, and uracil (–Leu –Trp –Ura –His) agar plates. Interacting bait–prey pairs were identified by growth on selective synthetic dropout IV agar plates (–Leu –Trp –Ura –His) after 5–6 d of incubation at 30°C. Non-autoactivating baits (L40ccU MATa yeast strains) were mated with prey strains at least four times using independently transformed bait and prey yeast colonies (384 array format). Only bait vector/prey vector combinations that showed growth in at least four independent replicas were considered as putative PPIs.

Cross-link mapping between BRP and RIM-BP

For synaptosomes preparation, see below. The synaptosome pellet was resuspended in homogenization buffer (320 mM sucrose, 5 mM Hepes, 1 mM PMSF, and a protease inhibitor tablet, pH 7.4). Freshly prepared disuccinimidyl sulfoxide cross-linker (http://www.thermofisher.com/order/catalog/product/A33545) was added to a final concentration of 1 mM and incubated for 1 h at room temperature. The cross-linking reaction was quenched by the addition of 50 mM Tris, pH 8.0, for 30 min. The cross-linked

synaptosome pellet was denatured in 8 M urea, reduced with 5 mM DTT at 56°C for 30 min and alkylated with 40 mM chloroacetamide for 30 min in the dark. Proteins are sequentially digested with Lys-C (4 h, 37°C, 1:75 [wt/wt] enzyme:substrate ratio) and trypsin (overnight, 37°C, 1:100 [wt/wt] enzyme:substrate ratio). The resulting peptide mixture was desalted using Sep-Pak C18 cartridges (Waters), dried under vacuum, reconstituted in 10% (vol/vol) formic acid, and fractionated by strong cation exchange chromatography. Strong cation exchange fractions were analyzed by liquid chromatography/mass spectrometry (LC/MS) using an UltiMate 3000 UPLC system (Thermo Fisher Scientific), equipped with an in-house packed C18 column for reversed phase separation (column material: Poroshell 120 EC-C18, 2.7 µm; Agilent Technologies) and coupled online to an Orbitrap Fusion mass spectrometer (Thermo Fisher Scientific). LC/MS acquisition was performed using 3 h gradient and a previously established MS2-MS3 method (https://www.ncbi.nlm.nih.gov/pubmed/28524877). In brief, sequential collision-induced dissociation (CID) MS2, and electron transfer dissociation MS2 acquisitions were applied to each MS1 precursor, followed by CID MS3 acquisitions if a unique mass difference (Δ = 31.9721 D) was observed in the CID MS2 spectrum. Data analysis was accomplished using XlinkX software (https://www.ncbi.nlm.nih.gov/pubmed/28524877), and results were reported at 1% false discovery rate (FDR).

Immunostainings of larval NMJs

Dissections were performed following standard protocols (Andlauer et al., 2014; Andlauer and Sigrist, 2012) and are described here: Third instar larvae were opened in HL3 by opening dorsally along the midline and removing the innards. Filets were fixated with 4% paraformaldehyde in PBS (pH 7.2) for 10 min for all antibodies or ice-cold MeOH for the anti-UNC13A antibody. After fixation, the filets were washed with PBS plus 0.05% Triton X-100 and blocked for 60 min in 5% normal goat serum. The larvae were incubated with primary antibodies at 4°C overnight and subsequently washed in a PBS plus 0.05% Triton X-100 solution for 2 h at room temperature for immunostaining. Larvae were then incubated for 3 h with secondary antibodies at room temperature. Washing procedures were repeated. Immunocytochemistry was equal for both conventional confocal and STED microscopy. Larvae were finally mounted either in Vectashield (Vector Laboratories) or Mowiol (Sigma-Aldrich) for STED.

Antibodies

The following primary antibodies were used: aBRP$^{C\text{-}term}$ (DSHB: Nc82), mouse, for IF 1:250, Developmental Studies Hybridoma Bank; aBRP$^{N\text{-}term}$ (Ex -2), rabbit, for IF 1:500 from our laboratory (see below); aBRP (last200), rabbit, for Western blot (WB) 1:50,000 (Siebert et al., 2015); aRIM-BP$^{C\text{-}term}$, (9171) rabbit, for IF 1:500, for WB 1:5,000 (Liu et al., 2011); aRIM-BP$^{N\text{-}term}$, (9172) rabbit, for IF 1:500 from our laboratory (see below); aUNC13A, guinea pig, for IF 1:500 (Böhme et al., 2016), aGFP mouse (A-11120, Invitrogen), aGFP rabbit (cA-11122, Invitrogen) for IF 1:500, aTubulin mouse, for WB 1:100,000 (62204, Thermo Fisher Scientific), HRP-Cy5 conjugated antibody (123–605-021, Jackson ImmunoResearch), for IF 1:250. All secondary antibodies were used 1:500. The following secondary antibodies were used: Alexa 488 anti-mouse (A-11001, Invitrogen) and anti-rabbit (A-11008, Invitrogen), 1:500; Cy3 anti-mouse (ab97035, abcam) and Cy3 anti-rabbit (ab6939, abcam), 1:500; Cy5 anti-mouse (ab6563, abcam) and anti-rabbit (ab97077, abcam), 1:500; Alexa 594 anti-mouse (A32742, Invitrogen) and anti-rabbit (A32754, Invitrogen) 1:500 used for STED; Atto647N anti-mouse (50185, Sigma Aldrich) and anti-rabbit (40839, Sigma Aldrich) and Al647 anti-guinea pig (A-21450, Invitrogen) 1:500 used for STED.

The BRP N-terminal (Ex -2) antibody was raised in rabbit against the peptide sequence RVRRLQELPTVDR, which is only present in the *brp* exon-2 encoded amino acid sequence (BRP isoform G; aa 19–31). The antiserum was affinity-purified with the peptide.

The RIM-BP$^{N\text{-}term}$ (9172) antibody was raised in rabbit against the following peptide sequence: SANVEEENRRPEKAAAAAS KKQKHKQQKSRPRGSHSMPYESMHHHQSAAAAVAAGTTPNGM LDALSLQLRDAEMRRTEIERAHQETLAQIRNLSGSARPDAEAVENLQSRAR-ELEKKVALENVRCEELQIELTSALKAKQASRSACSGMGSVSSGGGATIPTSA SSSTVTWAPTISHQDQGSEIDIIMAKIEQDNRVLAELEQPRTSASASMSALP PSSMLSTVNSEFRTISKSELEEELNRYKRAV. A 6×His-tagged fusion protein was used for immunization of rabbit. The amino acid sequence of positions 8–151 aa was used as antigen. The primers used for amplification of the DNA fragment are RBP-N-term FW 5′-AGGGCGCCATGGCCAGCGCAAACGTG-3′ and RBP-N-term REV 5′-CGGATCCGGTACCTTAAACTGCTCTTTT-3′. The fragment was cloned topET-30 His-tag vector, and *Escherichia coli* was used as an expression host for expression and purification of the target protein. Following the injection of the animals, the antibody (AB)-containing serum (obtained from Selbaq) was affinity-purified versus the same protein as used for immunization.

Image acquisition and analysis

Conventional confocal and STED images were acquired with Leica DMI 6000 (SP8) and TCS SP8 gSTED 3× microscopes (Leica Microsystems), respectively. For confocal scans, a HC PL APO CS2 63×/1.40-NA oil objective (Leica Microsystems) was used, and for STED a HC PL APO CS2 100×/1.40-NA oil objective (Leica Microsystems). Images were acquired at ∼20°C, and fluorochromes used are indicated in the antibody section. For detection, HYD (high sensitive) 400–800 nm spectral descanned for green and red channels and PMT 400–800 nm spectral descanned for far red channels were used for confocal scans. For STED, HyD Sp GaAsP were used. The NMJ z-stacks had a step size of 0.2–0.3 µm between single optical slices. All images were acquired using the LAS X software (Leica Microsystems). For all confocal and STED image analysis, the software ImageJ 1.52n was used. For all statistical analysis, the software GraphPad Prism, version 5.01, was used. For STED microscopy, Huygens Deconvolution software was used, applying a theoretical point spread function automatically computed based on pulsed- or continuous-wave STED optimized function and the specific microscope parameters. Default deconvolution settings were applied. Image analysis followed the standard protocol as

described in Andlauer and Sigrist (2012) and is described in detail for the different analyses as follows.

For whole NMJ confocal GFP mean pixel intensities for RIM-BP-FL^{GFP} and RIM-BP deletions^{GFP}, first the original confocal stacks were converted to maximal projections and the background subtracted. Second, the HRP signal was used as a template for a mask, restricting the quantified area to the shape of the NMJ. This mask was applied to the GFP channel and mean pixel intensity measured. Data distribution was tested following the D'Agostino and Pearson omnibus normality test, all data had a normal distribution, and an unpaired, two-sided *t* test comparing RIM-BP-FL^{GFP} to all other genetic conditions was applied. N represents a single NMJ. Analyzed are five animals/two NMJs per animal.

For quantification of single synapses (BRP number/NMJ, BRP mean intensity or BRP area) by confocal imaging, the signal of an HRP channel was used as a template for a mask, restricting the quantified area to the shape of the NMJ. The original confocal stacks were converted to maximal projections. After background subtraction, a HRP mask was created by applying a threshold to remove spurious low-intensity pixels. The segmentation of single spots was performed semiautomatically via the "Find Maxima" routine and by hand with the pencil tool and a line thickness of 1 pixel. The processed picture was then transformed into a binary mask using the same lower threshold value as in the first step. This binary mask was then projected onto the original unmodified image using the "min" operation from the ImageJ image calculator. The individual spots of the resulting images were counted with the help of the "analyze particle" function with a lower threshold set to 5. Single active zone per NMJ (AZ/NMJ) were then analyzed regarding mean pixel intensity, area, and number. AZ/NMJ area was obtained by normalizing the total number of AZs analyzed to the NMJ area measured via HRP. HRP mean pixel intensity was also measured (via the HRP mask) and if not significantly different between the genotypes, BRP mean pixel intensity values were normalized to the HRP mean pixel intensity. Analyzed were two NMJs/animal of three to six animals; *n* represents a single NMJ. For comparison of WT with RIM-BP-FL^{GFP}, the D'Agostino and Pearson omnibus normality test could not be performed due to too small *n*, but data distribution was assumed to be normal. An unpaired, two-sided *t* test was applied. For all other analyses of this type, data distribution was normal according to D'Agostino and Pearson omnibus normality test, and an unpaired, two-sided *t* test was applied.

To evaluate the nanoarchitecture of the singe active zone, the BRP$^{C\text{-}term}$ ring was analyzed by STED microscopy. Closed rings were counted as normal rings, open or elongated rings as deformed. Lateral rings at the edge of the bouton as well as AZ marked by only two-clustered BRP "rings" were excluded from analysis. N represents the mean of all AZ (20–40) from 1–3 boutons (one image). Two or three animals with two or three NMJs/animal and one to three boutons/NMJ were analyzed to reach ∼100 AZ/genetic condition. The D'Agostino and Pearson omnibus normality test could not be performed due to too small *n*, but data distribution was assumed to be normal. A one-way ANOVA was applied, using Tukey post-test.

To determine the number of UNC13A sites at a single AZ by STED microscopy, individual 100–300 AZs in a planar orientation were manually chosen in three animals with two or three NMJs/animal and two or three boutons/NMJ. *n* represents a single AZ (exception for the double LOF for RIM-BP-RNAi and *rim* mutant; as the genotype is highly lethal, we only had one larvae to analyze with three NMJs and one to three boutons/NMJ). UNC13A sites were identified via the Find Maxima function using a noise tolerance of 175 within a radius of 400 nm from the center of the BRP^{Nc82} ring. Data distribution is normal following the D'Agostino and Pearson omnibus normality test. An unpaired, two-sided *t* test was applied.

Distance measurements were performed by STED microcopy. A line profile was laid across vertical oriented synapses and the peak to peak distance measured. Data distribution is normal following the D'Agostino and Pearson omnibus normality test. A one-way ANOVA was applied using Tukey post-test. N represents a single AZ from three animals with two or three NMJs/animal and one or two boutons/NMJ; a total of 50–90 AZ/genotype was analyzed.

Viability assay

Three biological replicates were performed and 100–200 offspring per F1 generation analyzed. The genotypes were as follows: as driver line elaV-Gal4/X (homozygous);; *rim-bp*^{STOP1}/TM6B crossed either to the RIM-BP-FL^{GFP} rescue construct/II (homozygous); *rim-bp*^{null} (*Df2.01*)/TM6B or the eight deletion constructs (see Fig. 3 A; ΔRIM-BP^{GFP}/II (homozygous); *rim-bp*^{null} (*Df2.01*)/TM6B). Applying the Mendelian laws, the theoretically possible outcome of the correct genotype (elaV-Gal4/+; ΔRIM-BP^{GFP}/+; *rim-bp*^{null} (*Df2.01*)/*rim-bp*^{STOP1}) is due to lethality of the balancer chromosomes if homozygous (TM6B/TM6B) 33%. The survival rate was thus normalized to those 33% for all genotypes. Statistical analysis was performed with GraphPad Prism 5 software using an unpaired, two-sided *t* test comparing RIM-BP-FL^{GFP} with all other genetic conditions. As *n* = 3 for each biological replicate (per replicate, 100–200 animals were analyzed), the D'Agostino and Pearson omnibus normality test could not be performed due to too small *n*, but data distribution was assumed to be normal.

Multiple sequence alignment, phylogenetic tree, and sequence source

Sequences used in this study were obtained using a nucleotide and protein BLAST search from the publicly available database of the National Center for Biotechnology Information. The phylogenetic tree, multiple global sequence alignments (Blosum65), and editing (indications of deletion constructs, coiled-coil domain and interaction sites identified in cross-linking mass spectrometry) were performed in a Windows platform with the Geneious program version 9.1.8. Dark color within alignment indicates amino acid identity; light color indicates amino acid similarity.

Electrophysiology

Two-electrode voltage clamp (TEVC) recordings were performed essentially as previously reported (Matkovic et al., 2013). They

comprised spontaneous recordings (miniature excitatory junction currents: mEJCs, 90 s), single evoked (evoked excitatory junction currents: eEJCs, 20 repetitions at 0.2 Hz) and high-frequency recordings (paired-pulse 10 ms or 30 ms interstimulus interval, PP10 or PP30, 10 repetitions at 0.2 Hz; 60 pulses at 100 Hz for cumulative quantal content computation) as well as mean variance analysis (4× eEJC protocol at different c[Ca^{2+}]). All experiments were performed on third instar larvae raised at 25°C on semi-defined medium (Bloomington recipe). The dissection and recording medium was extracellular haemolymph-like solution 3 (Stewart et al., 1994; composition in mM: 70 NaCl, 5 KCl, 20 $MgCl_2$, 10 $NaHCO_3$, 5 trehalose, 115 sucrose, and 5 Hepes, pH adjusted to 7.2). Dissection was performed in ice-cold Ca^{2+}-free HL3 medium, while mEJC, eEJC, and high-frequency recordings were performed in 1.5 mM Ca^{2+} HL3 at room temperature. Data for mean-variance analysis were recorded at 0.75, 1.5, 3, and 6 mM Ca^{2+} by starting with a bath volume of 2 ml 0.75 mM Ca^{2+} HL3, consecutively removing 1 ml of the former bath solution and adding 1 ml of 2.25, 4.5, or 9 mM Ca^{2+} HL3, respectively, while mixing carefully with a pipette and giving 1 min of acclimation period before the next measurement. For all physiological recordings, intracellular electrodes with a resistance of 15–25 MΩ (filled with 3M KCl) were placed at muscle 6 of the abdominal segment A2/A3 for all physiological recordings. The data acquired were low-pass filtered at 1 kHz and sampled at 10 kHz. The command potential for mEJC recordings was −80 mV, and −60 mV for all other recordings. Only cells with an initial membrane potential between −50 and −70 mV and input resistances of ∼4 MΩ were used for further analysis.

The eEJC and paired-pulse traces were analyzed for standard parameters (amplitude, rise time, decay, charge flow, paired-pulse [PP]-ratio) by using a semiautomatic custom-written Matlab script (Mathworks, version R2009a). The 100-Hz trains were analyzed for amplitudes by using another semiautomatic custom-written Matlab script that calculates eEJC amplitudes by measuring peak to baseline directly before the onset of the response. The quantal content of each response was calculated by dividing the amplitude by the mean quantal size of the respective genotype. Release-ready vesicles (y intercept) and refilling rate (slope) were determined by back extrapolation of the last 300 ms of cumulative quantal contents. Mean variance analysis was basically performed as described previously (Reddy-Alla et al., 2017). In short, the amplitudes of 20 repetition traces per c[Ca^{2+}] were averaged and plotted against mean variance of the amplitudes (SD^2) to obtain the mean versus variance plot and parabolic fits. Second-order polynomial fits ($SD^2 = q \times \bar{I} - \bar{I}^2/N$) were performed per cell where q is the quantal size, $\bar{I}$ is the mean current amplitude, and N is the number of release sites. Vesicular release probability was calculated by $P_{VR} = \bar{I}/(N \times q)$ per cell. The parabolas in Fig. 4 represent fits to the mean values of a full dataset per genotype. Stimulation artifacts in eEJC and paired-pulse recordings were removed for clarity. The mEJC recordings were analyzed with pClamp 10 software (Molecular Devices). GraphPad Prism v5.01 (GraphPad Software, Inc.) was used for all fitting procedures.

Data were analyzed using GraphPad Prism v5.01. Data distribution is normal following the D'Agostino and Pearson omnibus normality test. If data had a normal distribution, an unpaired, two-sided *t* test was applied for comparison of two conditions or a one-way ANOVA using Tukey post-test if more than two conditions were compared. If data did have a normal distribution, the nonparametric, two-tailed Mann–Whitney test was applied for comparison of two conditions or the nonparametric Kruskal–Wallis test with the Dunn's post-test if more than two conditions were compared. For standard TEVC analysis, $n = 1$ cell, and one or two cells from four to six animals were analyzed. For variance-mean analysis, *n* is one animal, and seven to nine animals were analyzed.

EM

Conventional embedding was performed as described previously (Matkovic et al., 2013) and described here: dissected third instar larvae were fixed with PFA (10 min; 4% PFA and 0.5% glutaraldehyde in 0.1 M PBS) and glutaraldehyde (60 min; 2% glutaraldehyde in 0.1 M sodium cacodylate), washed in sodium cacodylate buffer, and post-fixed with 1% osmium tetroxide and 0.8% KFeCn in 0.1 M sodium cacodylate buffer (1 h on ice). After washing with sodium cacodylate buffer and distilled water, the samples were stained with 1% uranyl acetate in distilled water. Samples were dehydrated and infiltrated in epon resin. Subsequently, muscles 6/7 of the abdominal segment A2/3 were cut out. Collected in an embedding mold, the blocks were polymerized and cut into thin serial sections (65–70 nm). These sections were post-fixed and poststained with uranyl acetate/lead citrate. Micrographs were taken with an EM (JEM 1011; JEOL) equipped with a camera (Orius 1200A; Gatan) using the DigitalMicrograph software package (Gatan).

The plasma membrane and the electron-dense T-bar were detected by eye and labeled manually for quantification. The T-bar roof size was measured by a straight line connecting the furthest distance of the upmost T-bar dense material (in relation to the plasma membrane). The T-bar area was obtained by surrounding the dense material and measuring the area of the region of interest created.

Data were analyzed using GraphPad Prism v5.01. Data distribution is normal following the D'Agostino and Pearson omnibus normality test. An unpaired, two-sided *t* test was applied. All *ns* represent the number of quantified T-bars/SVs at a T-bar in four to six animals. No statistical methods were used to predetermine sample sizes, but our sample sizes are similar to those generally employed in the field.

Western blot analysis of larval central nervous system (CNS)

Larval CNS protein extraction was performed as follows: 10 CNS were dissected from third instar larvae. The tissues obtained were sheared manually in 5 µl of 2% SDS aqueous solution using a micropistill fitting tightly into a 1.5-ml cup. An amount of 0.5 µl of a 10% Triton X-100 aqueous solution and 5 µl of 2× sample Laemmli buffer was added, and samples were heated at 95°C for 10 min. Each sample was centrifuged for 2 min at 16,000 *g* to pellet the debris. An amount of 10 µl (equivalent to 10 larval CNS) was subjected to denaturing SDS-PAGE using a 6% Tris/HCl gel.

Proteins were then transferred onto a nitrocellulose membrane blocked with 5% skim milk in 1× PBS supplemented with 0.1% Tween-20 and probed with rabbit anti-RIM-BP (1:5,000; Liu et al., 2011) and mouse anti-tubulin (1:100,000) diluted in 5% milk in 1× PBS, supplemented with 0.1% Tween-20. After washing, secondary anti-rabbit (111–035-045, Dianova) or anti-mouse (115–035-146, Dianova) IgG HRP-conjugated antibodies were used for detection in conjunction with an enhanced chemiluminescence (RPN 2232, GE Healthcare ECL Prime) detection system with Hyperfilm ECL (GE Healthcare).

Co-immunoprecipitation analysis

Pulldown experiments with synaptosomes confirm the PPI between both proteins in vivo. Approximately 6,000 fly heads were collected, and synaptosomes were purified via differential centrifugation (see below and Depner et al., 2014). 20 µg of indicated rabbit antibodies each were coupled to 50 µl Protein A–coated agarose beads. Bead-antibody complexes were incubated with solubilized and precleared synaptosome membrane preparations (LP1) for at least 4 h. After four washing steps with immunoprecipitationbuffer (containing 20 mM Hepes, pH 7.4, 200 mM KCl, 2 mM $MgCl_2$, and 1% Triton X-100), antibody-antigen complexes were eluted with 60 µl 2× denaturing protein sample buffer each. For Western blot analysis, 1% of input and 10 µl of eluate were loaded. Probing was performed with RbαBRPlast200 (1:50,000, Depner et al., 2014) and RbαRIM-BPC-term (1:5,000, Liu et al., 2011).

Purification of pre- and post-synaptic components

The procedure involves decapitation of adult flies (sieving, ∼6,000 heads), pulverization, homogenization (320 mM sucrose, 4 mM Hepes, protease inhibitors [complete, 11873580001, Roche]) and differential centrifugation (from low speed to higher speed: 1,000–15,000 *g*) of fly heads, which allows subsequent purification of presynaptic and postsynaptic components (Depner et al., 2014).

NTR production and purification

Two constructs for the NTR were prepared (NTR^{8-151} and NTR^{8-254}) and cloned into the pETM11 vector with an N-terminal His_6-tag. The protein production of NTR^{8-151} and NTR^{8-254} is identical. The expression vector was transformed in *E. coli* BL21 Roesetta2 cells. Overexpression was performed using auto-induction media at 37°C until an OD ∼0.7 was reached and subsequently cooled down to 18°C (Studier, 2005). Cells were harvested by centrifugation (10 min, 6,000 rpm at 4°C). Buffer A was used (50 mM Tris/HCl, pH 7.4, 250 mM NaCl, 1 mM DTT, and 20 mM imidazole) for resuspension of the cell pellets. Cells were lysed by homogenization at 4°C, and the lysate was cleared by centrifugation (1 h, 21,000 rpm at 4°C). A Ni^{2+}-NTA (column volumes [cv] ∼1 ml; GE Healthcare) was equilibrated with buffer A. The NTR was loaded on the column and washed with 10 cv of buffer A. The NTR was eluted in a linear gradient to buffer A with an imidazole concentration of 400 mM. Pooled fractions were dialyzed overnight into buffer B (50 mM Tris/HCl, pH 7.4, 100 mM NaCl, and 1 mM DTT). A MonoQ HR 16/10 column (GE Healthcare) was equilibrated with buffer B before protein loading. Subsequently, the column was washed with 5 cv of buffer B. The NTR was eluted in a linear gradient to buffer B but with 1 M NaCl over 10 cv. 2 mg of Tobacco Etch Virus (TEV) protease were added to the pooled fractions and the protein dialyzed overnight into buffer C (10 mM Tris/HCl, pH 7.4, 100 mM NaCl, and 1 mM DTT). Size exclusion chromatography was performed with a HighLoad Superdex S75 26/60 column (GE Healthcare), equilibrated with buffer C. Pooled protein fractions were concentrated with Amicon-Ultra 10,000. Protein concentrations were determined by the absorbance at 280 nm.

FN-III(1–3) production and purification

The DNA coding for the three FN-III domains comprising aa 745–1042 was cloned into the pGEX-6P vector (GE Healthcare) fused to an N-terminal GST-tag. Expression and cell harvesting were performed as described above. The pellet was resuspended in buffer D (50 mM Tris/HCl, pH 7.5, 500 mM NaCl, 10% [vol/vol] glycerol, and 2 mM DTT). Cells were broken by sonication at 4°C, and the supernatant was cleared by 1 h of centrifugation (20,000 rpm at 4°C). The supernatant was loaded on 5 ml GSH-sepharose beads (GE Healthcare) equilibrated with buffer D. The bound protein sample was washed with 10 cv of buffer A, and a subsequent high-salt wash with buffer A with 1 M NaCl followed by 10 cv of buffer A. The protein was cleaved from the beads overnight by the addition of 2 mg Precission protease in buffer D. Size exclusion chromatography of FN-III(1–3) and a HighLoad Superdex S75 26/60 column (GE Healthcare) were equilibrated with 10 mM Tris/HCl, pH 7.5, 500 mM NaCl, and 10% (vol/vol) glycerol. Pooled protein fractions were concentrated with Amicon-Ultra 10,000 to 6 mg/ml.

Selenomethionine-labeled protein was overexpressed in *E. coli* BL21pLys Express cells in minimal medium supplemented with amino acids including selenomethionine instead of methionine (Van Duyne et al., 1993). The DTT was added to all buffers to a final concentration of 4 mM for protein purification. Incorporation of selenomethionine and molecular mass of proteins was confirmed by MALDI-TOF mass spectrometry.

Differential scanning fluorimetry experiment

The influence on the thermal stability of proteins under different buffer conditions was measured with the Mx3005P qPCR system (Agilent) in a 96-well plate format using a laboratory-made screen. Each well contained 135 µl buffer, 10 µl protein (1–2 µg/µl), and 1 µl of 10x SYPRO Orange dye (Invitrogen). The program consisted of three steps: step 1 was a preincubation for 1 min at 20°C, and steps 2 and 3 were cycles comprising the temperature increase of 1°C within 20 s. The temperature gradient proceeded from 25 to 95°C at 1°C per minute.

Crystallization and crystal cooling

The FN-III(1–3) was concentrated to 5 mg/ml for the crystallization experiment. Initial crystals of FN-III were obtained at 291 K in a sitting drop setup. Crystals appeared after 1 d in a sitting drop using a reservoir solution with a volume of 700 µl composed of 16% (wt/vol) polyethylenglycol 3350 and 300–400 mM KH_2PO_4. The crystallization drop was mixed from 1 µl protein and

1 µl reservoir solution. Initial crystals were obtained of a FN-III construct spanning residues 748 to 1039 diffracted to 10 Å. The diffraction quality of the initial crystals could be significantly improved by streak seeding. Fine tuning of the construct to a core region of ranging from 745 to 1042 improved the resolution to 3.6 Å. Differential scanning fluorimetry was employed to optimize the protein buffer. Addition of 10% (vol/vol) glycerol in all buffers increased the stability by 5°C and improved the diffraction quality of the crystals further. The crystals were transferred to a reservoir solution supplemented with 20% (vol/vol) glycerol and subsequently flash-cooled in liquid nitrogen for cryoprotection. Selenomethionine-labeled protein was concentrated to 4 mg/ml and crystallized under identical conditions as described for the native protein.

X-ray data collection, phasing, and refinement

Synchrotron diffraction data were collected at the beamline 14.2 of the MX Joint Berlin laboratory at BESSY (Berlin, Germany) or beamline P14 of Petra III (Deutsches Elektronen Synchrotron, Hamburg, Germany). X-ray data collection was performed at 100 K. Diffraction data were processed with the XDS package (Kabsch, 2010; Table S1). A randomly generated set of 5% of the reflections from the diffraction dataset was used to calculate the free R-factor and excluded from the refinement. Initial phases of the FN-III were determined by a three-wavelength multiwavelength anomalous diffraction experiment. Two selenomethionine sites per monomer could be identified with the program SHARP (Vonrhein et al., 2007). An initial model was built with the program BUCCANEER (Cowtan, 2008). The structure was first refined by applying a simulated annealing protocol and in later refinement cycles merely by maximum-likelihood restrained refinement implemented in PHENIX (Afonine et al., 2012), followed by iterative model building cycles with COOT (Emsley et al., 2010). Model quality was evaluated with PROCHECK (Laskowski et al., 1996) and MolProbity (Chen et al., 2010). Figures were prepared using PyMOL. Domain movements were analyzed with the DynDom software (Girdlestone and Hayward, 2016). The atomic coordinates and structure factor amplitudes have been deposited in the Protein Data Bank under the accession no. 6Q9M.

Circular dichroism (CD) spectroscopy

Proteins were dialyzed against CD buffer (10 mM K_2HPO_4 and 50 mM NaCl) at 4°C overnight and diluted to a final concentration of 1.2 mg/ml. All spectra were recorded with a Jasco J-810 spectropolarimeter using quartz cuvettes with 0.1 mm path length. Initial CD spectra were collected at wavelengths between 190 and 240 nm at 20°C. The α-helical content was calculated with the CDNN CD spectral deconvolution software (version 2.1, Gerald Böhm). The CD melting profiles were recorded by heating the samples by 2°C/min from 20 to 95°C, following the CD signal at 222 nm.

RNA extraction and quantitative RT-PCR

Total RNA was purified from ∼20 adult fly heads using the NucleoSpin RNA Isolation kit (Macherey-Nagel) according to the manufacturer's instructions. 1 µg RNA was reverse-transcribed into cDNA using M-MuLV Reverse transcription enzyme (200,000 units/ml, New England Biolabs) and random primers (100 pmol/µl, Invitrogen). Quantitative RT-PCR was performed using a StepOnePlus Real-Time PCR System (Thermo Fisher Scientific). Reactions were performed in triplicates in MicroAm Optical 96-well Reaction Plates (Thermo Fisher Scientific) using Luna Universal qPCR Master Mix (New England Biolabs). Target gene expression was quantified relative to *Act5C* using the ΔΔCT method including primer efficiency (Pfaffl, 2001). The following primer sets were used (5′-3′, forward and reverse): total *RIM-BP* forward 5′-CCGGCCGCGGCGGTCTGAGCC-3′ and reverse 5′-GTGTAGGGGAAGCAGGGCGAG-3′, and *GFP* forward 5′-GGCGTG CAGTGCTTCAGCCG-3′ and reverse 5′-CGTCCTTGAAGAAGA TGGTG-3′. N represents three independent experiments ($n = 3$). As $n = 3$, the D'Agostino and Pearson omnibus normality test could not be performed due to too small n, but data distribution was assumed to be normal. A one-way ANOVA was applied using the Tukey post-test.

Online supplemental material

Fig. S1 shows that RIM-BP and the RIM-BP SH3 domain are conserved across species. Fig. S2 shows RIM-BP:: BRP pulldown experiments, synaptosome preparation, and RIM-BP FN-III domain conservation. Fig. S3 shows validation of the RIM-BP-FL^{GFP} rescue construct and Western blot analysis of *Drosophila* larval brains. Fig. S4 shows RIM-BP SH3-III domain analysis. Fig. S5 shows that RIM-BP SH3-II/III binding to Ca^{2+} channels is dispensable for RIM-BP integration into the AZ matrix and SH3-II/III domain localization. Fig. S6 shows that RIM-BP NTR2 is required for AZ scaffold stability and synaptogenesis. Fig. S7 is an analysis of RIM-family protein function in electrophysiology, scaffold assembly, and release site positioning. Fig. S8 shows that RIM-BP NTR1 promotes SV recruitment into the release sites. Table S1 shows diffraction data collection, phasing, and refinement statistics for FN-III(1).

Acknowledgments

We thank C. Alings for support in the crystallization experiments. We acknowledge access to the CD spectrometer of Prof. B. Koch. We thank T. Schneider for access and support at beamline P14 of PETRA III (Deutsches Elektronen Synchrotron, Hamburg, Germany). We accessed beamlines of the BESSY II (Berliner Elektronenspeicherring-Gesellschaft für Synchrotronstrahlung II) storage ring (Berlin, Germany) via the Joint Berlin MX-Laboratory sponsored by the Helmholtz Zentrum Berlin für Materialien und Energie, the Freie Universität Berlin, the Humboldt-Universität zu Berlin, the Max-Delbrück Centrum, and the Leibniz-Institut für Molekulare Pharmakologie. Finally, we would like to thank Paul Sigrist for his support.

We were supported by the Deutsche Forschungsgemeinschaft (SFB958/A6 and TRR186/A3). We thank C. Weise (SFB958/Z3) for mass spectrometric analysis. A.G. Petzoldt was supported by the SFB958 women support program and the Berlin Institute of Health Gender Equality Fund.

The authors declare no competing financial interests.

Author contributions: A.G. Petzoldt performed all genetic experiments, designed experiments, and performed all confocal and STED imaging, including analysis. T.W.B. Götz conducted all electrophysiological experiments, except for the Cac analysis, which was done by E. Knoche. J.H. Driller, J. Lützkendorf, and U. Stelzl performed the Y2H analysis. J.H. Driller and B. Loll performed the crystal structure analysis. J.H. Driller, J. Lützkendorf, S. Liu, S. Reddy-Alla, S. Mertel, and C. Beuschel cloned constructs. S. Liu performed recombinant expression experiments. J.H. Driller performed WB analysis. V. Ugorets and J. Lützkendorf performed RT-PCR. T. Matkovic-Rachid performed the EM analysis. M. Lehmann contributed to the STED microscopy. N. Ramesh and A.G. Petzoldt created the model. B. Kuropka and C. Freund performed mass spectrometry on the FN-III constructs. F. Liu performed the cross-linking experiment. M.C. Wahl and S.J. Sigrist designed the study and wrote the manuscript.

Submitted: 11 February 2019
Revised: 3 February 2020
Accepted: 7 April 2020

References

Acuna, C., X. Liu, A. Gonzalez, and T.C. Südhof. 2015. RIM-BPs Mediate Tight Coupling of Action Potentials to Ca(2+)-Triggered Neurotransmitter Release. *Neuron*. 87:1234–1247. https://doi.org/10.1016/j.neuron.2015.08.027

Acuna, C., X. Liu, and T.C. Südhof. 2016. How to Make an Active Zone: Unexpected Universal Functional Redundancy between RIMs and RIM-BPs. *Neuron*. 91:792–807. https://doi.org/10.1016/j.neuron.2016.07.042

Afonine, P.V., R.W. Grosse-Kunstleve, N. Echols, J.J. Headd, N.W. Moriarty, M. Mustyakimov, T.C. Terwilliger, A. Urzhumtsev, P.H. Zwart, and P.D. Adams. 2012. Towards automated crystallographic structure refinement with phenix.refine. *Acta Crystallogr. D Biol. Crystallogr*. 68:352–367. https://doi.org/10.1107/S0907444912001308

Andlauer, T.F., and S.J. Sigrist. 2012. Quantitative analysis of Drosophila larval neuromuscular junction morphology. *Cold Spring Harb. Protoc*. 2012:490–493.

Andlauer, T.F., S. Scholz-Kornehl, R. Tian, M. Kirchner, H.A. Babikir, H. Depner, B. Loll, C. Quentin, V.K. Gupta, M.G. Holt, et al. 2014. Drep-2 is a novel synaptic protein important for learning and memory. *eLife*. 3. e03895. https://doi.org/10.7554/eLife.03895

Andrews-Zwilling, Y.S., H. Kawabe, K. Reim, F. Varoqueaux, and N. Brose. 2006. Binding to Rab3A-interacting molecule RIM regulates the presynaptic recruitment of Munc13-1 and ubMunc13-2. *J. Biol. Chem*. 281: 19720–19731. https://doi.org/10.1074/jbc.M601421200

Betz, A., P. Thakur, H.J. Junge, U. Ashery, J.S. Rhee, V. Scheuss, C. Rosenmund, J. Rettig, and N. Brose. 2001. Functional interaction of the active zone proteins Munc13-1 and RIM1 in synaptic vesicle priming. *Neuron*. 30:183–196. https://doi.org/10.1016/S0896-6273(01)00272-0

Böhme, M.A., C. Beis, S. Reddy-Alla, E. Reynolds, M.M. Mampell, A.T. Grasskamp, J. Lützkendorf, D.D. Bergeron, J.H. Driller, H. Babikir, et al. 2016. Active zone scaffolds differentially accumulate Unc13 isoforms to tune Ca2+ channel–vesicle coupling. *Nat Neurosci*. 19(10):1311–1320.

Brand, A.H., and N. Perrimon. 1993. Targeted gene expression as a means of altering cell fates and generating dominant phenotypes. *Development*. 118:401–415.

Brockmann, M.M., M. Maglione, C.G. Willmes, A. Stumpf, B.A. Bouazza, L.M. Velasquez, M.K. Grauel, P. Beed, M. Lehmann, N. Gimber, et al. 2019. RIM-BP2 primes synaptic vesicles *via* recruitment of Munc13-1 at hippocampal mossy fiber synapses. *eLife*. 8. e43243. https://doi.org/10.7554/eLife.43243

Bruckner, J.J., S.J. Gratz, J.K. Slind, R.R. Geske, A.M. Cummings, S.E. Galindo, L.K. Donohue, and K.M. O'Connor-Giles. 2012. Fife, a Drosophila Piccolo-RIM homolog, promotes active zone organization and neurotransmitter release. *J. Neurosci*. 32:17048–17058. https://doi.org/10.1523/JNEUROSCI.3267-12.2012

Bruckner, J.J., H. Zhan, S.J. Gratz, M. Rao, F. Ukken, G. Zilberg, and K.M. O'Connor-Giles. 2017. Fife organizes synaptic vesicles and calcium channels for high-probability neurotransmitter release. *J. Cell Biol*. 216: 231–246. https://doi.org/10.1083/jcb.201601098

Carr, P.D., S.E. Gustin, A.P. Church, J.M. Murphy, S.C. Ford, D.A. Mann, D.M. Woltring, I. Walker, D.L. Ollis, and I.G. Young. 2001. Structure of the complete extracellular domain of the common beta subunit of the human GM-CSF, IL-3, and IL-5 receptors reveals a novel dimer configuration. *Cell*. 104:291–300. https://doi.org/10.1016/S0092-8674(01)00213-6

Chen, V.B., W.B. Arendall, III, J.J. Headd, D.A. Keedy, R.M. Immormino, G.J. Kapral, L.W. Murray, J.S. Richardson, and D.C. Richardson. 2010. MolProbity: all-atom structure validation for macromolecular crystallography. *Acta Crystallogr. D Biol. Crystallogr*. 66:12–21. https://doi.org/10.1107/S0907444909042073

Clements, J.D., and R.A. Silver. 2000. Unveiling synaptic plasticity: a new graphical and analytical approach. *Trends Neurosci*. 23:105–113. https://doi.org/10.1016/S0166-2236(99)01520-9

Cowtan, K.. 2008. Fitting molecular fragments into electron density. *Acta Crystallogr. D Biol. Crystallogr*. 64:83–89. https://doi.org/10.1107/S0907444907033938

Davydova, D., C. Marini, C. King, J. Klueva, F. Bischof, S. Romorini, C. Montenegro-Venegas, M. Heine, R. Schneider, M.S. Schröder, et al. 2014. Bassoon specifically controls presynaptic P/Q-type Ca(2+) channels via RIM-binding protein. *Neuron*. 82:181–194. https://doi.org/10.1016/j.neuron.2014.02.012

Depner, H., J. Lützkendorf, H.A. Babkir, S.J. Sigrist, and M.G. Holt. 2014. Differential centrifugation-based biochemical fractionation of the Drosophila adult CNS. *Nat. Protoc*. 9:2796–2808. https://doi.org/10.1038/nprot.2014.192

Emsley, P., B. Lohkamp, W.G. Scott, and K. Cowtan. 2010. Features and development of Coot. *Acta Crystallogr. D Biol. Crystallogr*. 66:486–501. https://doi.org/10.1107/S0907444910007493

Fouquet, W., D. Owald, C. Wichmann, S. Mertel, H. Depner, M. Dyba, S. Hallermann, R.J. Kittel, S. Eimer, and S.J. Sigrist. 2009. Maturation of active zone assembly by Drosophila Bruchpilot. *J. Cell Biol*. 186:129–145. https://doi.org/10.1083/jcb.200812150

Fulterer, A., T.F.M. Andlauer, A. Ender, M. Maglione, K. Eyring, J. Woitkuhn, M. Lehmann, T. Matkovic-Rachid, J.R.P. Geiger, A.M. Walter, et al. 2018. Active Zone Scaffold Protein Ratios Tune Functional Diversity across Brain Synapses. *Cell Rep*. 23:1259–1274. https://doi.org/10.1016/j.celrep.2018.03.126

Girdlestone, C., and S. Hayward. 2016. The DynDom3D Webserver for the Analysis of Domain Movements in Multimeric Proteins. *J. Comput. Biol*. 23:21–26. https://doi.org/10.1089/cmb.2015.0143

Graf, E.R., V. Valakh, C.M. Wright, C. Wu, Z. Liu, Y.Q. Zhang, and A. DiAntonio. 2012. RIM promotes calcium channel accumulation at active zones of the Drosophila neuromuscular junction. *J. Neurosci*. 32: 16586–16596. https://doi.org/10.1523/JNEUROSCI.0965-12.2012

Grauel, M.K., M. Maglione, S. Reddy-Alla, C.G. Willmes, M.M. Brockmann, T. Trimbuch, T. Rosenmund, M. Pangalos, G. Vardar, A. Stumpf, et al. 2016. RIM-binding protein 2 regulates release probability by fine-tuning calcium channel localization at murine hippocampal synapses. *Proc. Natl. Acad. Sci. USA*. 113:11615–11620. https://doi.org/10.1073/pnas.1605256113

Hallermann, S., A. Fejtova, H. Schmidt, A. Weyhersmüller, R.A. Silver, E.D. Gundelfinger, and J. Eilers. 2010a. Bassoon speeds vesicle reloading at a central excitatory synapse. *Neuron*. 68:710–723. https://doi.org/10.1016/j.neuron.2010.10.026

Hallermann, S., R.J. Kittel, C. Wichmann, A. Weyhersmüller, W. Fouquet, S. Mertel, D. Owald, S. Eimer, H. Depner, M. Schwärzel, et al. 2010b. Naked dense bodies provoke depression. *J. Neurosci*. 30:14340–14345. https://doi.org/10.1523/JNEUROSCI.2495-10.2010

Han, Y., P.S. Kaeser, T.C. Südhof, and R. Schneggenburger. 2011. RIM Determines Ca2+ Channel Density and Vesicle Docking at the Presynaptic Active Zone. *Neuron*. 69(2):304–316.

Hegele, A., A. Kamburov, A. Grossman, C. Sourlis, S. Wowro, M. Weimann, C.L. Will, V. Pena, R. Luhrmann, and U. Stetzl; A. Kamburov, A. Grossmann, C. Sourlis, S. Wowro, M. Weimann, C.L. Will, V. Pena, R. Luhrmann, and U. Stelzl. 2012. Dynamic protein-protein interaction wiring of the human spliceosome. *Mol Cell*. https://doi.org/10.1016/j.molcel.2011.12.034

Hibino, H., R. Pironkova, O. Onwumere, M. Vologodskaia, A.J. Hudspeth, and F. Lesage. 2002. RIM binding proteins (RBPs) couple Rab3-interacting molecules (RIMs) to voltage-gated Ca(2+) channels. *Neuron*. 34:411–423. https://doi.org/10.1016/S0896-6273(02)00667-0

Jahn, R., and D. Fasshauer. 2012. Molecular machines governing exocytosis of synaptic vesicles. *Nature*. 490:201–207. https://doi.org/10.1038/nature11320

Kabsch, W.. 2010. Integration, scaling, space-group assignment and post-refinement. *Acta Crystallogr. D Biol. Crystallogr.* 66:133–144. https://doi.org/10.1107/S0907444909047374

Kaeser, P.S., L. Deng, Y. Wang, I. Dulubova, X. Liu, J. Rizo, and T.C. Südhof. 2011. RIM proteins tether Ca2+ channels to presynaptic active zones via a direct PDZ-domain interaction. *Cell*. 144:282–295. https://doi.org/10.1016/j.cell.2010.12.029

Kelley, L.A., S. Mezulis, C.M. Yates, M.N. Wass, and M.J. Sternberg. 2015. The Phyre2 web portal for protein modeling, prediction and analysis. *Nat. Protoc.* 10:845–858. https://doi.org/10.1038/nprot.2015.053

Kittel, R.J., C. Wichmann, T.M. Rasse, W. Fouquet, M. Schmidt, A. Schmid, D.A. Wagh, C. Pawlu, R.R. Kellner, K.I. Willig, et al. 2006. Bruchpilot promotes active zone assembly, Ca2+ channel clustering, and vesicle release. *Science*. 312:1051–1054. https://doi.org/10.1126/science.1126308

Krinner, S., T. Butola, S. Jung, C. Wichmann, and T. Moser. 2017. RIM-Binding Protein 2 Promotes a Large Number of $Ca_V1.3$ Ca^{2+}-Channels and Contributes to Fast Synaptic Vesicle Replenishment at Hair Cell Active Zones. *Front. Cell. Neurosci.* 11:334. https://doi.org/10.3389/fncel.2017.00334

Krissinel, E., and K. Henrick. 2007. Inference of macromolecular assemblies from crystalline state. *J. Mol. Biol.* 372:774–797. https://doi.org/10.1016/j.jmb.2007.05.022

Laskowski, R.A., J.A. Rullmannn, M.W. MacArthur, R. Kaptein, and J.M. Thornton. 1996. AQUA and PROCHECK-NMR: programs for checking the quality of protein structures solved by NMR. *J. Biomol. NMR*. 8:477–486. https://doi.org/10.1007/BF00228148

Leitner, A., M. Faini, F. Stengel, and R. Aebersold. 2016. Crosslinking and Mass Spectrometry: An Integrated Technology to Understand the Structure and Function of Molecular Machines. *Trends Biochem. Sci.* 41:20–32. https://doi.org/10.1016/j.tibs.2015.10.008

Li, M.Z., and S.J. Elledge. 2012. SLIC: a method for sequence- and ligation-independent cloning. *Methods Mol. Biol.* 852:51–59. https://doi.org/10.1007/978-1-61779-564-0_5

Liu, F., and A.J. Heck. 2015. Interrogating the architecture of protein assemblies and protein interaction networks by cross-linking mass spectrometry. *Curr. Opin. Struct. Biol.* 35:100–108. https://doi.org/10.1016/j.sbi.2015.10.006

Liu, K.S., M. Siebert, S. Mertel, E. Knoche, S. Wegener, C. Wichmann, T. Matkovic, K. Muhammad, H. Depner, C. Mettke, et al. 2011. RIM-binding protein, a central part of the active zone, is essential for neurotransmitter release. *Science*. 334:1565–1569. https://doi.org/10.1126/science.1212991

Lupas, A.N., and J. Bassler. 2017. Coiled Coils - A Model System for the 21st Century. *Trends Biochem. Sci.* 42:130–140. https://doi.org/10.1016/j.tibs.2016.10.007

Matkovic, T., M. Siebert, E. Knoche, H. Depner, S. Mertel, D. Owald, M. Schmidt, U. Thomas, A. Sickmann, D. Kamin, et al. 2013. The Bruchpilot cytomatrix determines the size of the readily releasable pool of synaptic vesicles. *J. Cell Biol.* 202:667–683. https://doi.org/10.1083/jcb.201301072

Mittelstaedt, T., and S. Schoch. 2007. Structure and evolution of RIM-BP genes: identification of a novel family member. *Gene*. 403:70–79. https://doi.org/10.1016/j.gene.2007.08.004

Müller, M., K.S. Liu, S.J. Sigrist, and G.W. Davis. 2012. RIM controls homeostatic plasticity through modulation of the readily-releasable vesicle pool. *J. Neurosci.* 32:16574–16585. https://doi.org/10.1523/JNEUROSCI.0981-12.2012

Müller, M., Ö. Genç, and G.W. Davis. 2015. RIM-binding protein links synaptic homeostasis to the stabilization and replenishment of high release probability vesicles. *Neuron*. 85:1056–1069. https://doi.org/10.1016/j.neuron.2015.01.024

Pfaffl, M.W.. 2001. A new mathematical model for relative quantification in real-time RT-PCR. *Nucleic Acids Res.* 29. e45. https://doi.org/10.1093/nar/29.9.e45

Reddy-Alla, S., M.A. Bohme, E. Reynolds, C. Beis, A.T. Grasskamp, M.M. Mampell, M. Maglione, M. Jusyte, U. Rey, H. Babikir, et al. 2017. Stable Positioning of Unc13 Restricts Synaptic Vesicle Fusion to Defined Release Sites to Promote Synchronous Neurotransmission. *Neuron*. 95:1350–1364.e12.

Sakaba, T., R. Schneggenburger, and E. Neher. 2002. Estimation of quantal parameters at the calyx of Held synapse. *Neurosci. Res.* 44:343–356. https://doi.org/10.1016/S0168-0102(02)00174-8

Sakamoto, H., T. Ariyoshi, N. Kimpara, K. Sugao, I. Taiko, K. Takikawa, D. Asanuma, S. Namiki, and K. Hirose. 2018. Synaptic weight set by Munc13-1 supramolecular assemblies. *Nat. Neurosci.* 21:41–49. https://doi.org/10.1038/s41593-017-0041-9

Sclip, A., C. Acuna, F. Luo, and T.C. Südhof. 2018. RIM-binding proteins recruit BK-channels to presynaptic release sites adjacent to voltage-gated Ca^{2+}-channels. *EMBO J.* 37. e98637. https://doi.org/10.15252/embj.201798637

Siebert, M., M.A. Böhme, J.H. Driller, H. Babikir, M.M. Mampell, U. Rey, N. Ramesh, T. Matkovic, N. Holton, S. Reddy-Alla, et al. 2015. A high affinity RIM-binding protein/Aplip1 interaction prevents the formation of ectopic axonal active zones. *eLife*. 4. e06935. https://doi.org/10.7554/eLife.06935

Silver, R.A.. 2003. Estimation of nonuniform quantal parameters with multiple-probability fluctuation analysis: theory, application and limitations. *J. Neurosci. Methods*. 130:127–141. https://doi.org/10.1016/j.jneumeth.2003.09.030

Stanley, E.F.. 2016. The Nanophysiology of Fast Transmitter Release. *Trends Neurosci.* 39:183–197. https://doi.org/10.1016/j.tins.2016.01.005

Stelzl, U., U. Worm, M. Lalowski, C. Haenig, F.H. Brembeck, H. Goehler, M. Stroedicke, M. Zenkner, A. Schoenherr, S. Koeppen, et al. 2005. A Human Protein-Protein Interaction Network: A Resource for Annotating the Proteome. *Cell*. 122(6):957–968.

Stewart, B.A., H.L. Atwood, J.J. Renger, J. Wang, and C.F. Wu. 1994. Improved stability of Drosophila larval neuromuscular preparations in haemolymph-like physiological solutions. *J. Comp. Physiol. A Neuroethol. Sens. Neural Behav. Physiol.* 175:179–191. https://doi.org/10.1007/BF00215114

Studier, F.W.. 2005. Protein production by auto-induction in high density shaking cultures. *Protein Expr Purif*. https://doi.org/10.1016/j.pep.2005.01.016

Südhof, T.C.. 2012. The presynaptic active zone. *Neuron*. 75:11–25. https://doi.org/10.1016/j.neuron.2012.06.012

Swanson, C.J., and S. Sivaramakrishnan. 2014. Harnessing the unique structural properties of isolated α-helices. *J. Biol. Chem.* 289:25460–25467. https://doi.org/10.1074/jbc.R114.583906

Van Duyne, G.D., R.F. Standaert, P.A. Karplus, S.L. Schreiber, and J. Clardy. 1993. Atomic structures of the human immunophilin FKBP-12 complexes with FK506 and rapamycin. *J. Mol. Biol.* 229:105–124. https://doi.org/10.1006/jmbi.1993.1012

Van Vactor, D., and S.J. Sigrist. 2017. Presynaptic morphogenesis, active zone organization and structural plasticity in Drosophila. *Curr. Opin. Neurobiol.* 43:119–129. https://doi.org/10.1016/j.conb.2017.03.003

Venkatesan, K., J.-F. Rual, A. Vazquez, U. Stelzl, I. Lemmens, T. Hirozane-Kishikawa, T. Hao, M. Zenkner, X. Xin, K.-I. Goh, et al. 2008. An empirical framework for binary interactome mapping. *Nat Methods*. 6(1):83–90.

Vonrhein, C., E. Blanc, P. Roversi, and G. Bricogne. 2007. Automated structure solution with autoSHARP. *Methods Mol. Biol.* 364:215–230.

Wagh, D.A., T.M. Rasse, E. Asan, A. Hofbauer, I. Schwenkert, H. Dürrbeck, S. Buchner, M.C. Dabauvalle, M. Schmidt, G. Qin, et al. 2006. Bruchpilot, a protein with homology to ELKS/CAST, is required for structural integrity and function of synaptic active zones in Drosophila. *Neuron*. 49:833–844. https://doi.org/10.1016/j.neuron.2006.02.008

Wang, Y., S. Sugita, and T.C. Sudhof. 2000. The RIM/NIM family of neuronal C2 domain proteins. Interactions with Rab3 and a new class of Src homology 3 domain proteins. *J. Biol. Chem.* 275:20033–20044. https://doi.org/10.1074/jbc.M909008199

Wang, Y., X. Liu, T. Biederer, and T.C. Südhof. 2002. A family of RIM-binding proteins regulated by alternative splicing: Implications for the genesis of synaptic active zones. *Proc. Natl. Acad. Sci. USA*. 99:14464–14469. https://doi.org/10.1073/pnas.182532999

Wang, S.S.H., R.G. Held, M.Y. Wong, C. Liu, A. Karakhanyan, and P.S. Kaeser. 2016. Fusion Competent Synaptic Vesicles Persist upon Active Zone Disruption and Loss of Vesicle Docking. *Neuron*. 91:777–791. https://doi.org/10.1016/j.neuron.2016.07.005

Worseck, J.M., A. Grossman, M. Weimann, A. Hegele, and U. Stelzl. 2012. A stringent yeast two-hybrid matrix screening approach for protein-protein interaction discovery. *Methods Mol Biol*. https://doi.org/10.1007/978-1-61779-455-1_4

Xu, Y., N.J. Kershaw, C.S. Luo, P. Soo, M.J. Pocock, P.E. Czabotar, D.J. Hilton, N.A. Nicola, T.P. Garrett, and J.G. Zhang. 2010. Crystal structure of the entire ectodomain of gp130: insights into the molecular assembly of the tall cytokine receptor complexes. *J. Biol. Chem.* 285:21214–21218. https://doi.org/10.1074/jbc.C110.129502

JCB

Supplemental material

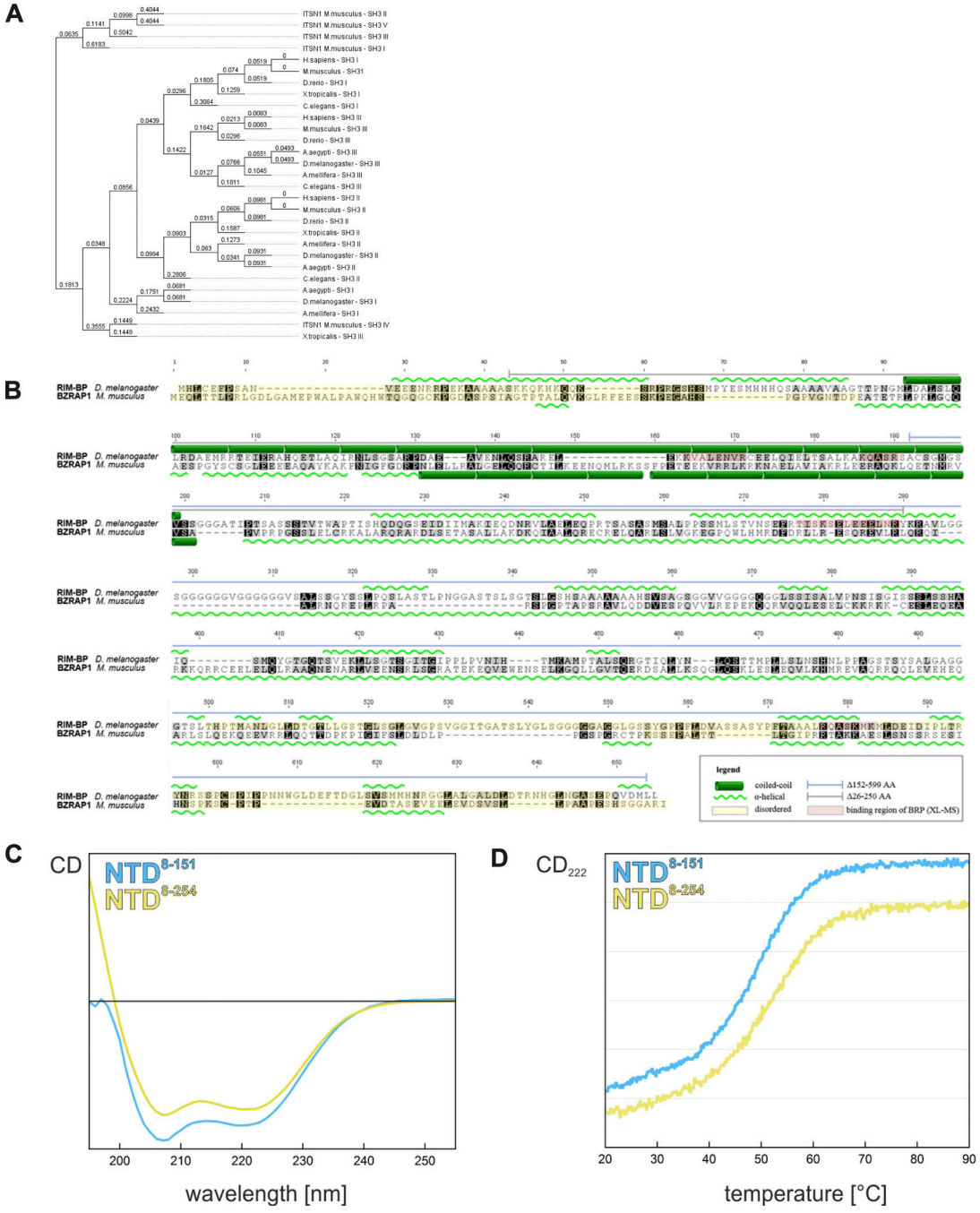

Figure S1. **RIM-BP and the RIM-BP SH3 domain are conserved across species. (A)** Phylogenetic tree representing the high degree of similarity of the RIM-BP SH3 domains among the following different species: *Mus musculus*, *Homo sapiens*, *Danio rerio*, *Xenopus tropicalis*, *Aedes aegypti*, *Caenorhabditis elegans*, *Apis mellifera*, and *Drosophila melanogaster*. The SH3 domain–rich protein Intersectin1 (M. *musculus*) was incorporated in the dendogram analysis as a phylogenetic test, showing less similarity to the RIM-BP SH3 domains. Sequences are grouped together as operational taxonomic units . The sum of the branches' lengths between sequences (referred to as patristic distance or tree distance) is shown. The smaller the distance value is, the higher the phylogenetic relationship. The C-terminal SH3 domains of *Drosophila* RIM-BP show the highest similarities across different species, for example *M. musculus* (0.61) and *A. aegypti* (0.1). Close similarities of the fly SH3 I domain exist with *A. aegypti* (0.76) and *A. mellifera* (0.76) than remote species, such as *M. musculus* (0.93) and *H. sapiens* (1.36). **(B)** Sequence alignment between *Drosophila* RIM-BP and mammalian BZRAP1 (RIM-BP1) showing the conserved clusters within the NTR. The increase in dark shading represents higher similarity: dark color within alignment indicates amino acid identity, and light color, amino acid similarity. The global alignment of a sequence was performed with Geneious software (8.1.9). The sequence alignment of *Drosophila* RIM-BP (isoform F) NTR and mammalian BZRAP1 (RIM-BP1) N-term shows the highest level of conservation throughout the predicted coiled-coil region (green cylindrical boxes), which consists of α-helical structures. Additionally, the conserved disordered regions (yellow shadow; Protein Homology/analogY Recognition Engine V 2.0 (Phyre2) [Kelley et al., 2015]) and α-helical structures (green waves; Phyre2) for mammalian and fly RIM-BPs are indicated in the alignment. A high amino acid similarity could be observed within the BRP binding sites detected in XL-MS (cross-link) analysis of purified *Drosophila* synaptosomes (indicated in red shadows). Both RIM-BP NTR deletion constructs used in this study are indicated by gray (RIM-BPΔNTR1^{GFP}) and blue (RIM-BPΔNTR2^{GFP}) lines. **(C)** CD spectra of the NTR$^{8-151}$ (blue) and NTR$^{8-254}$ (yellow). **(D)** CD melting curve of the NTR$^{8-151}$ (blue) and NTR$^{8-254}$ (yellow) with a melting temperature of 50°C.

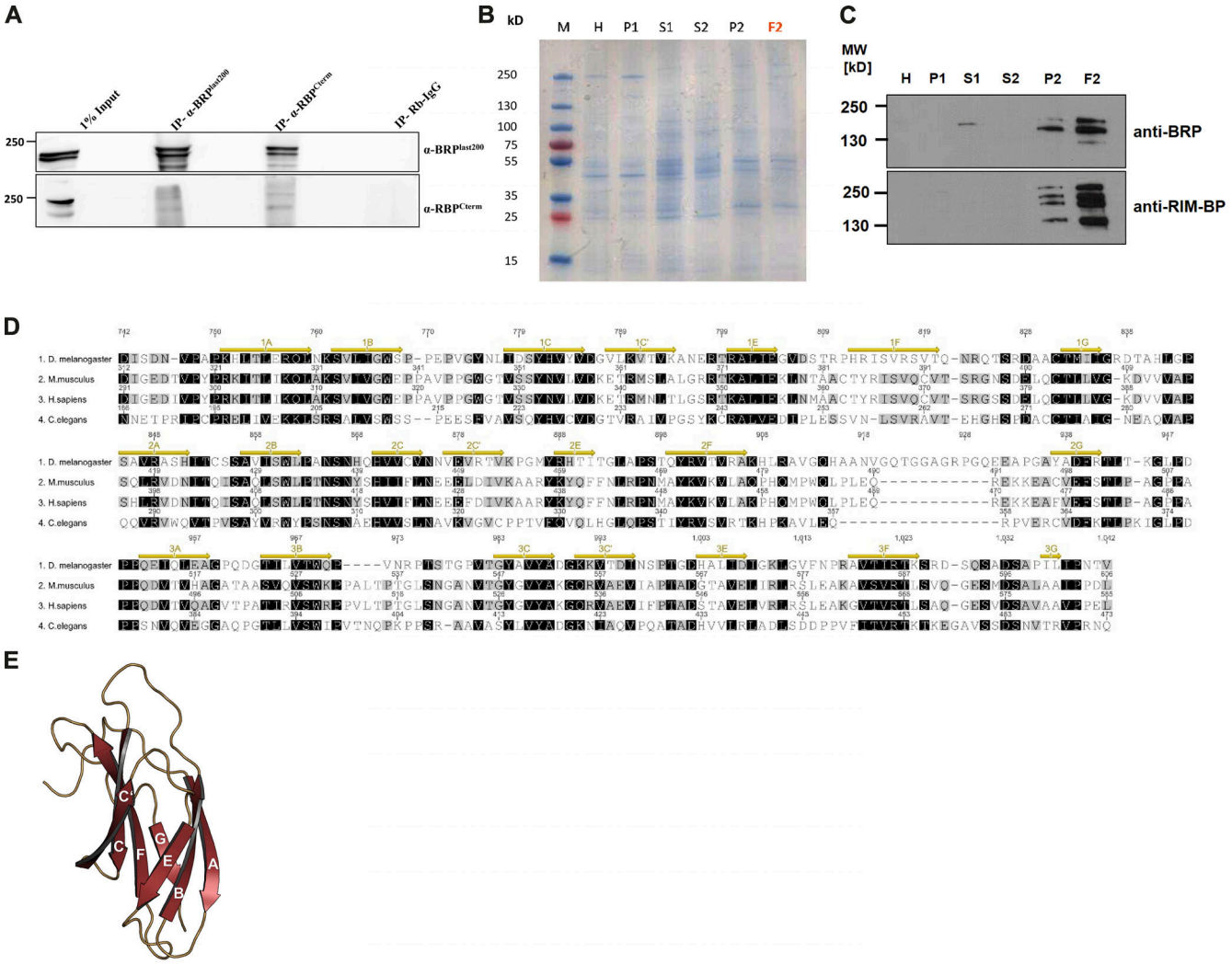

Figure S2. **RIM-BP:: BRP pulldown experiments, synaptosome preparation, and RIM-BP FN-III domain conservation. (A)** Pulldown experiments from synaptosomes (see C and Materials and methods) confirm the protein–protein interaction between RIM-BP and BRP. For Western analysis, 1% of input (lane 1) and 10 µl of eluate were loaded (lane 2 for BRP and lane 3 for RIM-BP). The eluate was probed against BRP (upper panel) and RIM-BP (lower panel). The BRP double bands (190 kD and 170 kD isoforms) are present in the input as well as both specific IPs, but are not present in control rabbit immunoglobulins (RbIgGs; lane 4). Similarly, for RIM-BP, two specific bands are detected in both obtained IP (lane 2 and 3) samples by Western blot. The negative IgG control (lane 4) is positive for neither BRP nor RIM-BP. **(B)** Coomassie staining of synaptosome preparation (see Materials and methods) following Depner et al. (2014). As a loading control, 10 µl protein of each fraction (analytical sample) has been loaded and stained with Coomassie blue. S = supernatants, P = pellets, H = head homogenate, S1 = small cell fragments and microsomes, P1 = fly head debris, large cell fragments, S2 = small cell fragments (microsomes) and synaptic vesicles, P2 = synaptosomes, LP1 = presynaptic and postsynaptic membranes, and LS1 = presynaptic cytosol and synaptic vesicles. **(C)** Synaptosome preparation according to Depner et al. (2014). Abbreviations as in C. Probed against BRP (upper panel) and RIM-BP (lower panel). MW, molecular weight. **(D)** Multiple sequence alignment of the three FN-III domains (residues 742–1042) of *D. melanogaster* RIM-BP isoform F with homologues from *H. sapiens*, *Mus musculus*, and *C. elegans* prepared with Geneious version 5.3.6 software. Darker shading indicates a higher conservation of residues; β-strands of our structure are indicated in yellow. **(E)** A structural cartoon representation of FN-III(1) in RIM-BP from molecule "B." Linker regions are colored in sand, and β-strands are labeled and colored in red.

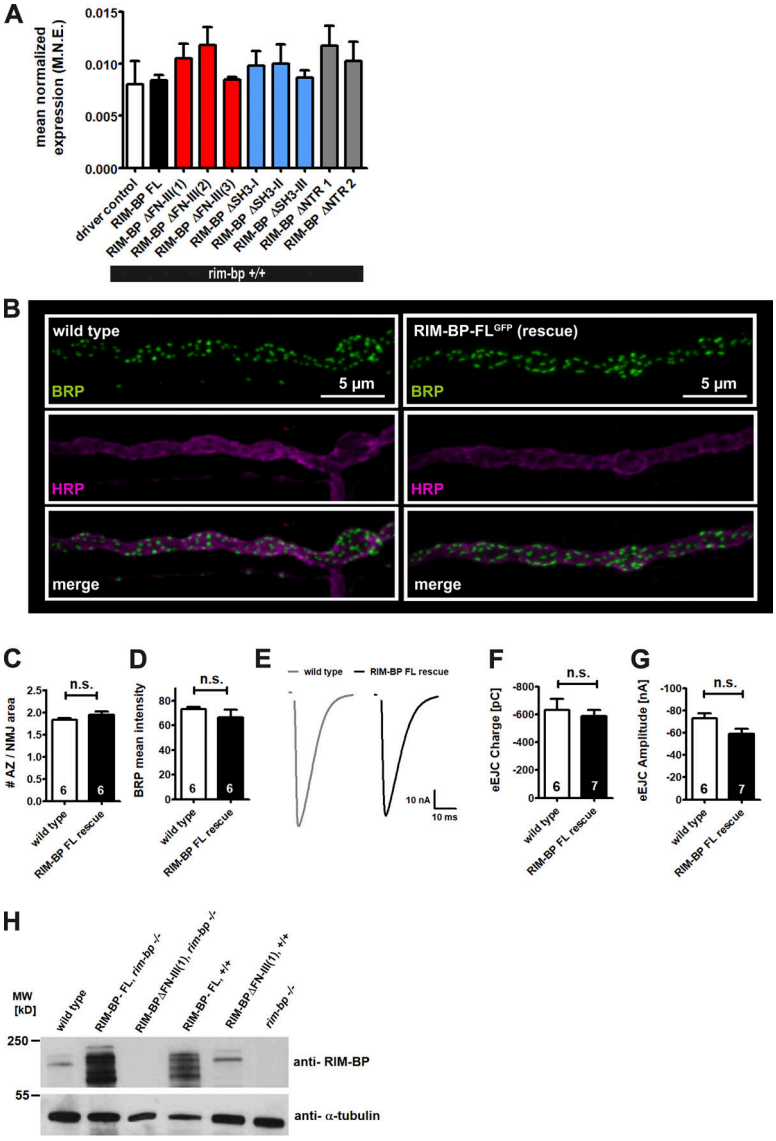

Figure S3. **Validation of the RIM-BP-FL^{GFP} rescue construct and Western blot analysis of *Drosophila* larval brains. (A)** Quantitative reverse-transcription polymerase chain reaction (qRT-PCR) analysis using RNA from of adult fly heads from the driver control, the RBP-FL, the RIM-BP ΔFN-III, ΔSH3, and ΔNTR domains in the WT (+/+) background were performed using primers detecting endogenous as well as GFP-tagged RIM-BP constructs. Data points summarize triplicate measurements and show mean normalized expression (M.N.E.) ± SEM (for duplicate measurements) normalized against the housekeeping gene Actin5c (driver control 0.0081 ± 0.0022; RIM-BP-FL^{GFP} 0.0084 ± 0.0005; RIM-BPΔFN-III(1)^{GFP} 0.0105 ± 0.0014; RIM-BPΔFN-III(2)^{GFP} 0.0118 ± 0.00182; RIM-BPΔFN-III(3)^{GFP} 0.0085 ± 0.0003; RIM-BPΔSH3-I^{GFP} 0.0098 ± 0.0014; RIM-BP ΔSH3-II^{GFP} 0.01 ± 0.0019; RIM-BPΔSH3-III^{GFP} 0.0087 ± 0.0007; RIM-BPΔNTR1^{GFP} 0.0117 ± 0.0019; RIM-BPΔNTR2^{GFP} 0.0103 ± 0.0019). All graphs show ± SEM. Data distribution was assumed to be normal; see Materials and methods. A one-way ANOVA was applied, using Tukey post-test. All comparisons are statistically nonsignificant. N represents three independent experiments (n = 3). **(B)** Immunofluorescence stainings of NMJs of third instar *Drosophila* larvae comparing WT (left panel) and the RIM-BP-FL^{GFP} rescue construct in the *rim-bp* mutant background. Stained for BRP (green) and HRP (neuronal membrane marker, magenta). Scale bar, 5 µm. **(C)** Quantification of the number of AZ per NMJ area of the representative images in A (WT 1.83 ± 0.04, n = 6; RIM-BP-FL^{GFP} rescue 1.94 ± 0.08, n = 6). **(D)** Quantification of the single AZ BRP mean pixel intensity of the representative images in A (WT 73.09 ± 1.98, n = 6; RIM-BP-FL^{GFP} rescue 66.50 ± 6.13, n = 6). For C and D, all graphs show ± SEM. Data distribution was assumed to be normal; see Materials and methods. An unpaired, two-sided t test was applied, n.s. = not significant. N represents a single NMJ. Three animals are analyzed with two NMJs/animal. **(E–G)** TEVC analysis of the WT and RIM-BP-FL^{GFP} rescue construct in the *rim-bp* mutant background. **(E)** Example traces of evoked EJC. **(F)** eEJC charge (WT −632.2 ± 79.32 pC, n = 6; RIM-BP-FL^{GFP} rescue −587.5 ± 44.19 pC, n = 7). Graph shows ± SEM. Data distribution is normal following the D'Agostino and Pearson omnibus normality test. An unpaired, two-sided t test was applied, n.s. = not significant. N represents a single cell. Three or four animals are analyzed with one or two cells/animal. **(G)** eEJC amplitudes (WT −73.20 ± 4.45 nA, n = 6; RIM-BP-FL^{GFP} rescue −59.41 ± 4.41 nA, n = 7). Graph shows ± SEM. Data distribution was not normal following the D'Agostino and Pearson omnibus normality test; we therefore applied the nonparametric two-tailed Mann–Whitney test, n.s. = not significant. N represents a single cell. Three or four animals are analyze with one or two cells/animal. **(H)** Western blot analysis of the RIM-BP protein level of larval head protein extracts. Protein extracts of 10 dissected larval brains of each genotype indicated were subjected to SDS-PAGE followed by probing with rabbit anti-RIM-BP$^{N\text{-}term}$ and loading control mouse anti-tubulin. Two prominent RIM-BP bands were detected in the WT (w1118, first lane) that are not detected in the *rim-bp* mutant background (sixth lane). The RIM-BP-FL^{GFP} construct showed high expression of RIM-BP protein in both genetic backgrounds, *rim-bp* mutant (lane 2) and the endogenous background (lane 4). The RIM-BPΔFN-III(1)^{GFP} displayed two RIM-BP–specific bands (lane 5) but not in the *rim-bp* mutant background (lane 3) in the presence of endogenous RIM-BP.

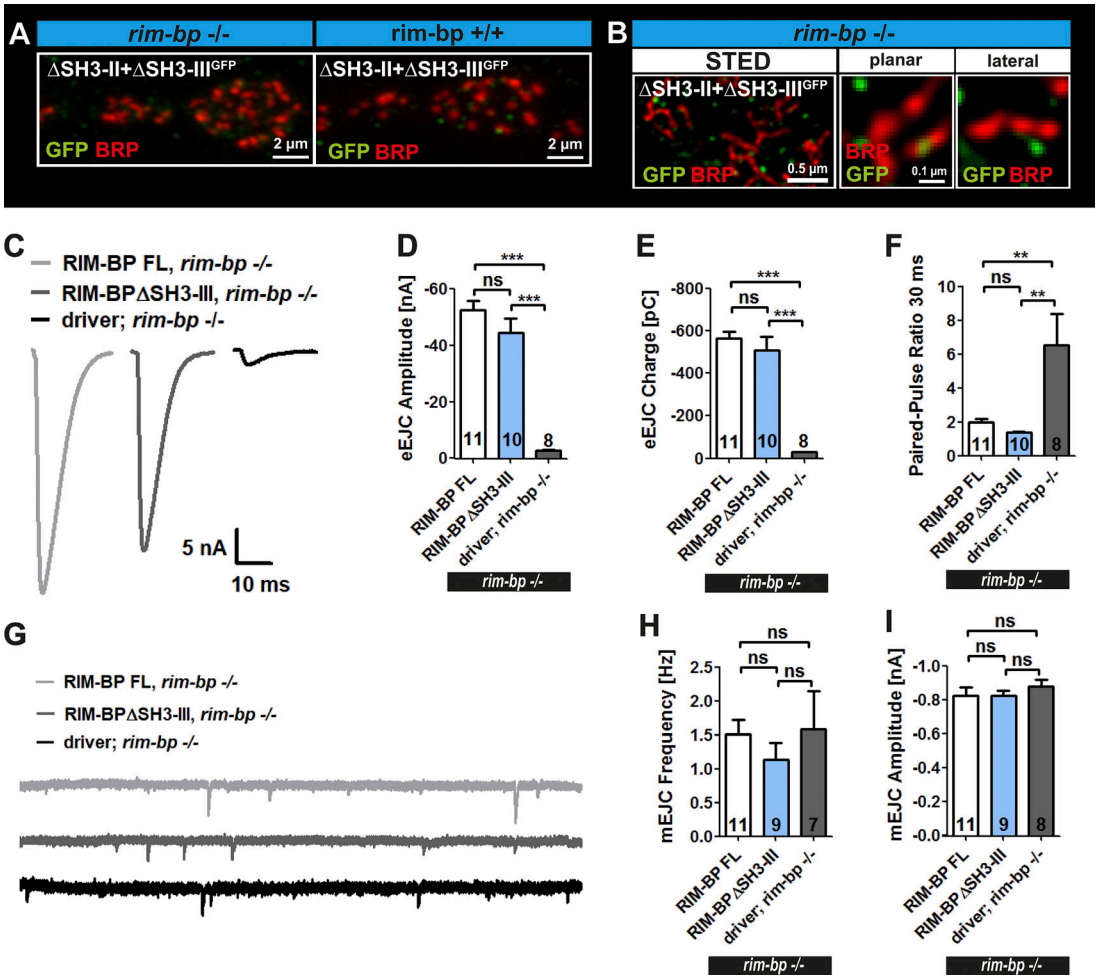

Figure S4. **RIM-BP SH3-III domain analysis. (A and B)** Representative confocal (A) and STED (B) images of immunostained third instar larval NMJs expressing the RIM-BPΔSH3-II + ΔSH3-III^{GFP} construct either into the *rim-bp* mutant (−/−) or WT (+/+) background stained for GFP (green) or BRP (red). Scale bar, 2 µm (B) or 0.5 µm (C). **(C–F)** Two-electrode voltage clamp electrophysiological recordings of *Drosophila* third instar larvae NMJs for the driver control, the RIM-BP-FL^{GFP}, and the RIM-BPΔSH3-III^{GFP} construct all reexpressed in the *rim-bp* mutant background. **(C)** Example traces of evoked EJC. **(D)** eEJC amplitudes (RIM-BP-FL^{GFP} −52.73 ± 3.17 nA, *n* = 11; RIM-BPΔSH3-III^{GFP} −44.56 ± 5.08 nA, *n* = 10; driver, *rim-bp* mutant −2.86 ± 0.31 nA, *n* = 8). **(E)** Evoked excitatory junctional charge (RIM-BP-FL^{GFP} −564.3 ± 31.45 pC, *n* = 11; RIM-BPΔSH3-III^{GFP} −508.2 ± 64.52 pC, *n* = 10; driver, *rim-bp* mutant −29.36 ± 2.06 pC, *n* = 8). **(F)** Paired-pulse ratio for 30 ms (RIM-BP-FL^{GFP} 1.96 ± 0.21, *n* = 11; RIM-BPΔSH3-III^{GFP} 1.37 ± 0.08, *n* = 10; driver, *rim-bp* mutant 6.53 ± 1.83, *n* = 8). **(D–F)** All graphs show ± SEM. Data distribution is normal following the D'Agostino and Pearson omnibus normality test. A one-way ANOVA was applied, using Tukey post-test, **, P < 0.01, ***, P < 0.001, n.s. = not significant. N represents a single cell. Four to six animals are analyzed with one or two cells/animal. **(G–I)** Spontaneous release TEVC analysis for the driver control, the RIM-BP-FL^{GFP}, and the RIM-BPΔSH3-III^{GFP} construct all reexpressed in the *rim-bp* mutant background. **(G)** Example traces of miniature EJC. **(H)** mEJC frequency (RIM-BP-FL^{GFP} 1.51 ± 0.21 Hz, *n* = 11; RIM-BPΔSH3-III^{GFP} 1.14 ± 0.24 Hz, *n* = 9; driver, *rim-bp* mutant 1.58 ± 0.21 Hz, *n* = 7). Graph shows ± SEM. Data distribution is not normal following the D'Agostino and Pearson omnibus normality test; we therefore applied the nonparametric Kruskal–Wallis test with the Dunn's post-test, ns = not significant. N represents a single cell. Four to six animals are analyzed with one or two cells/animal. **(I)** Miniature amplitude (RIM-BP-FL^{GFP} −0.83 ± 0.05 nA, *n* = 11; RIM-BPΔSH3-III^{GFP} −0.83 ± 0.03 nA, *n* = 9; driver, *rim-bp* mutant −0.88 ± 0.04 nA, *n* = 8). Graph shows ± SEM. Data distribution is normal following the D'Agostino and Pearson omnibus normality test. A one-way ANOVA was applied, using Tukey post-test, ns = not significant. N represents a single cell. Four to six animals are analyzed with one or two cells/animal.

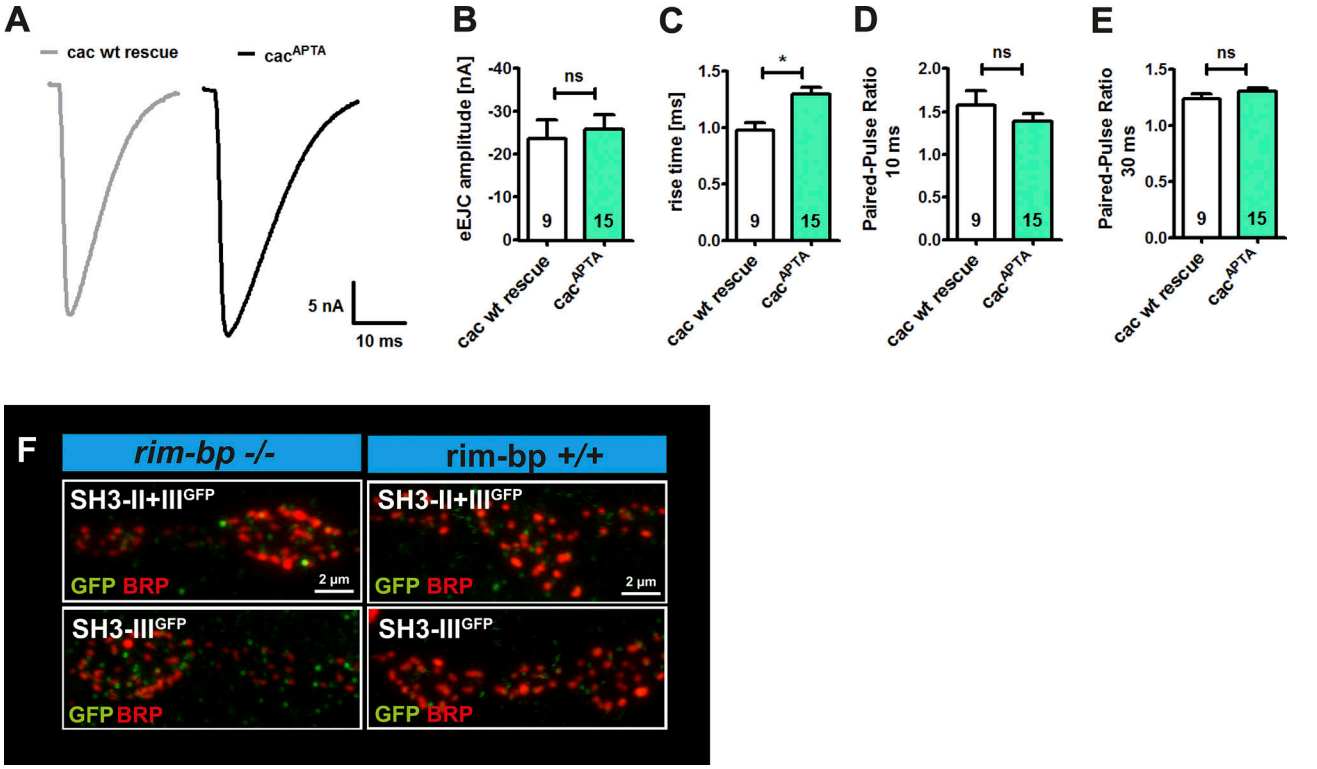

Figure S5. **RIM-BP SH3-II/III binding to Ca^{2+} channels is dispensable for RIM-BP integration into the AZ matrix and SH3-II/III domain localization.** **(A–E)** Two-electrode voltage clamp electrophysiological recordings of *Drosophila* third instar larval NMJs reexpressing either a WT (cac^{WT}) or the mutated cacophony (cac^{APTA}) into the *cac* mutant background. **(A)** Example traces of evoked EJC. **(B)** eEJC amplitudes (cac^{WT} −23.76 ± 4.29 nA, *n* = 9; cac^{APTA} −25.81 ± 3.39 nA, *n* = 15). Graph shows ± SEM. Data distribution was not normal following the D'Agostino and Pearson omnibus normality test; we therefore applied the nonparametric two-tailed Mann–Whitney test, ns = not significant. N represents a single cell. Three to six animals are analyzed with one or two cells/animal. **(C)** Rise time (cac^{WT} 0.98 ± 0.07 ms, *n* = 9; cac^{APTA} 1.3 ± 0.07 ms, *n* = 15). **(D)** 10 ms paired-pulse ratio (cac^{WT} 1.58 ± 0.17, *n* = 9; cac^{APTA} 1.39 ± 0.08, *n* = 15) and (E) 30 ms paired-pulse ratio (cac^{WT} 1.24 ± 0.05, *n* = 9; cac^{APTA} 1.31 ± 0.03, *n* = 15). **(C–E)** all graphs show ± SEM. Data distribution is normal following the D'Agostino and Pearson omnibus normality test. An unpaired, two-sided *t* test was applied, *, P < 0.05, ns = not significant. N represents a single cell. Three to six animals are analyzed with one or two cells/animal. **(F)** Single SH3-II/III^{GFP} or SH3-III^{GFP} domains were reexpressed in the *rim-bp* mutant background of *Drosophila* third instar larvae, and NMJs were immunostained for GFP (green) and BRP (red). Scale bar, 2 µm.

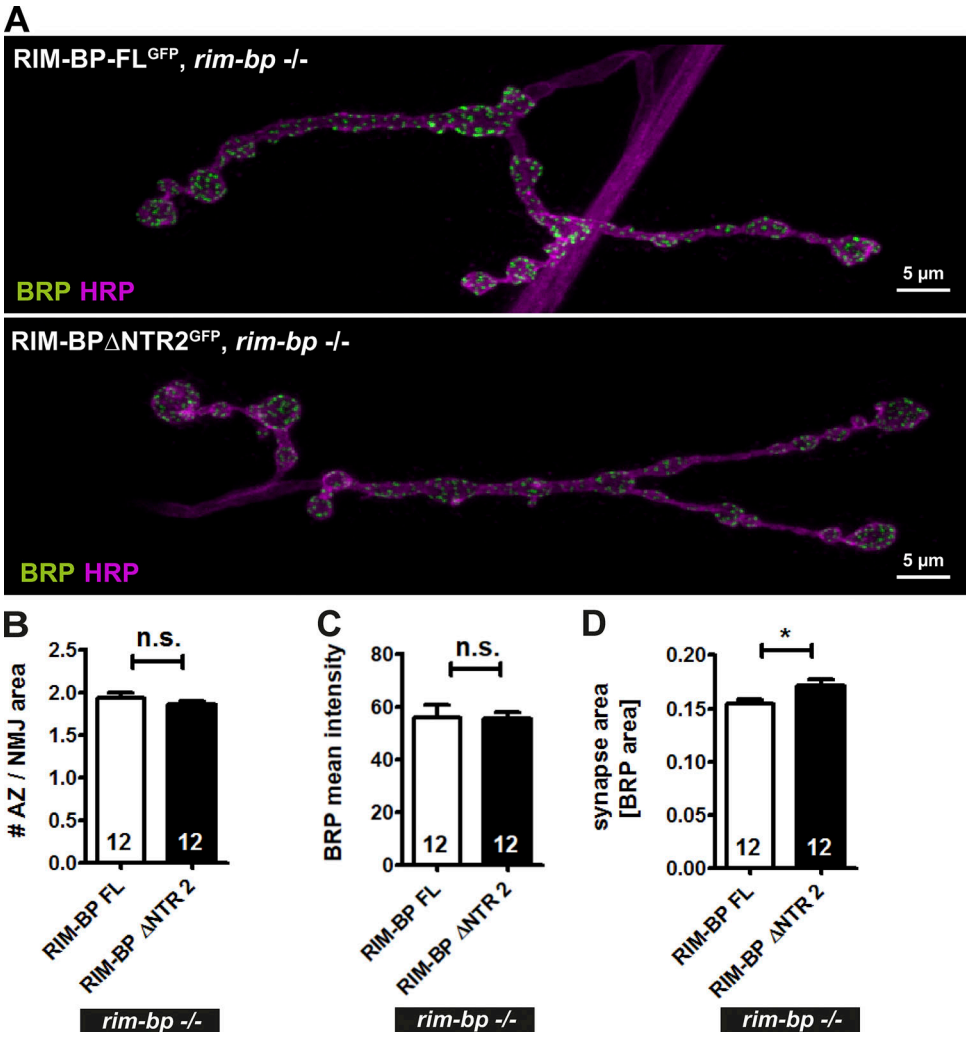

Figure S6. **RIM-BP NTR2 required for AZ scaffold stability and synaptogenesis. (A)** Confocal images of immunostained third instar *Drosophila* larval NMJs expressing either the RIM-BP-FL^{GFP} (upper panel) or the RIM-BPΔNTR2^{GFP} construct (lower panel) in the *rim-bp* mutant stained for BRP (green) and HRP (magenta). Scale bar, 5 µm. **(B–D)** Quantification of the representative images shown in Fig. S7. NMJs of third instar *Drosophila* larvae expressing either the RIM-BP-FL rescue or the RIM-BPΔNTR2^{GFP} construct in a *rim-bp* null background were immunostained and analyzed. **(B)** Number of AZs per NMJ area (RIM-BP-FL^{GFP} 1.94 ± 0.06, *n* = 12, RIM-BPΔNTR2^{GFP} 1.86 ± 0.03, *n* = 12). **(C)** BRP mean pixel intensity (BRP mean pixel intensity/HRP mean pixel intensity RIM-BP-FL^{GFP} 1.55 ± 0.04, *n* = 12, RIM-BPΔNTR2^{GFP} 1.39 ± 0.07, *n* = 12). **(D)** Synapse area defined by the BRP spot size (RIM-BP-FL^{GFP} 0.16 ± 0.004, *n* = 12, RIM-BPΔNTR2^{GFP} 0.17 ± 0.006, *n* = 12). **(B–D)** All graphs show ± SEM. Data distribution is normal following the D'Agostino and Pearson omnibus normality test. An unpaired, two-sided *t* test was applied, *, P < 0.05, n.s. = not significant. N represents a single NMJ. Six animals were analyzed with two NMJs/animal.

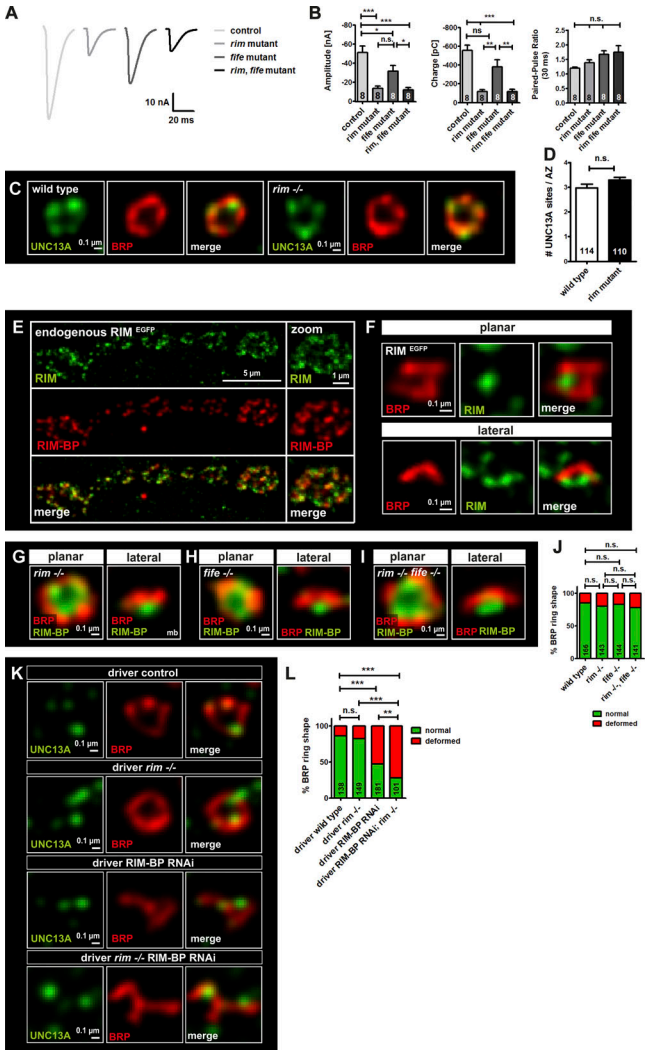

Figure S7. **Analysis of RIM-family protein function in electrophysiology, scaffold assembly, and release site positioning. (A and B)** Two-electrode voltage clamp electrophysiological recordings of *Drosophila* third instar larvae NMJs for the single *rim* mutant, the single *fife* mutant, and the *rim/fife* double mutant. **(A)** Example traces of evoked EJC. **(B)** eEJC amplitudes (left panel: control: −51.39 ± 6.63 nA, *n* = 8; *rim* mutant: −13.88 ± 2.31 nA, *n* = 8; *fife* mutant: −31.88 ± 2.31 nA, *n* = 8; *rim/fife* mutant: −12.04 ± 2.54 nA, *n* = 8), evoked excitatory junctional charge (middle panel: control: −557.9 ± 57.27 pC, *n* = 8; *rim* mutant: −116.3 ± 20.47 pC, *n* = 8; *fife* mutant: −380.6 ± 75.28 pC, *n* = 8; *rim/fife* mutant: −116.1 ± 27.55 pC, *n* = 8) and 30 ms paired-pulse ratio (right panel: control: 1.19 ± 0.04, *n* = 8; *rim* mutant: 1.38 ± 0.1, *n* = 8; *fife* mutant: 1.67 ± 0.13, *n* = 8; *rim/fife* mutant: 1.74 ± 0.23, *n* = 8). All graphs show ± SEM. Data distribution is normal following the D'Agostino and Pearson omnibus normality test. A one-way ANOVA was applied, using Tukey post-test, *, P < 0.05; **, P < 0.01; ***, P < 0.001; n.s. = not significant. N represents a single cell. Four to six animals are analyzed with one or two cells/animal. **(C)** Representative STED images of WT (left panel) and *rim* mutant AZs of third instar *Drosophila* larval NMJs (right panel) immunostained for UNC13A (green) and BRP (red). Scale bar, 0.1 µm. **(D)** Quantification of the number of UNC13A marked release sites of the representative images shown in C (WT 2.97 ± 0.16, *n* = 12 NMJs from three animals, a total of 114 AZs counted; *rim* mutant 3.29 ± 0.11, *n* = 12 NMJs from three animals, a total of 110 AZs counted). Graph shows ± SEM. Data distribution is normal following the D'Agostino and Pearson omnibus normality test. An unpaired, two-sided *t* test was applied, n.s. = not significant. **(E)** Confocal images of immunostained third instar *Drosophila* larval NMJs expressing endogenously tagged RIM^{EGFP} protein (anti-GFP, green) and RIM-BP (red). Scale bars, 5 µm. Right panel with zoom, scale bar, 1 µm. **(F)** STED images of the same genotype showing RIM (green) localization into the central AZ scaffold (BRP, red) in the planar view (upper panel) and close to the membrane at fusion sites in the lateral view (lower panel). Scale bar, 0.1 µm. **(G–I)** Representative STED images of third instar *Drosophila* larval NMJs stained for BRP (red) or RIM-BP (green) of the *rim* mutant (G), the *fife* mutant (H), and the *rim/fife* double mutant (I). Scale bar, 0.1 µm. **(J)** Quantification of AZ scaffold architecture of the representative images shown in G–I (WT 84.52% ± 2.96 normal AZs [BRP C-terminal rings] and 15.49% ± 2.96 deformed AZs; *rim* mutant 80.28% ± 3.18 normal AZs and 19.72% ± 3.18 deformed AZs; *fife* mutant 82.79% ± 2.95 normal AZs and 17.21% ± 2.95 deformed AZs; *rim/fife* double mutant normal AZs 77.67% ± 1.12 and 22.33% ± 1.12 deformed AZs). **(K)** STED images of immunostained third instar *Drosophila* larval NMJs expressing the driver (ok6-Gal4) control, the driver in the *rim* mutant (−/−), the driver with the RIM-BP RNAi, and the driver with the RIM-BP-RNAi in the *rim* mutant (−/−) stained for UNC13A (green) and BRP (red). Scale bar, 0.1 µm. **(L)** Quantification of AZ scaffold architecture of the representative images shown in K (driver, WT 86.14% ± 1.44 normal AZs (BRP C-terminal rings) and 13.86% ± 1.44 deformed AZs (from one or two animals with two or three NMJs/animal for all genotypes); driver, *rim* mutant 82.10% ± 2.18 normal AZs and 17.91% ± 2.18 deformed AZs; driver, RIM-BP RNAi 47.47% ± 4.39 normal AZs and 52.53% ± 4.39 deformed AZs; driver, RIM-BP RNAi, *rim* mutant 27.78% ± 5.28 normal AZs and 72.22% ± 5.28 deformed AZs. **(J and L)** All graphs show ± SEM. Data distribution was assumed to be normal; see Materials and methods. A one-way ANOVA was applied, using Tukey post-test, **, P < 0.01; ***, P < 0.001; n.s. = not significant. N represents the mean of all AZ (20–40) from one to three boutons (one image). Two or three animals are analyzed with two or three NMJs/animal and one to three boutons/NMJ to reach ∼100 AZ/genetic condition.

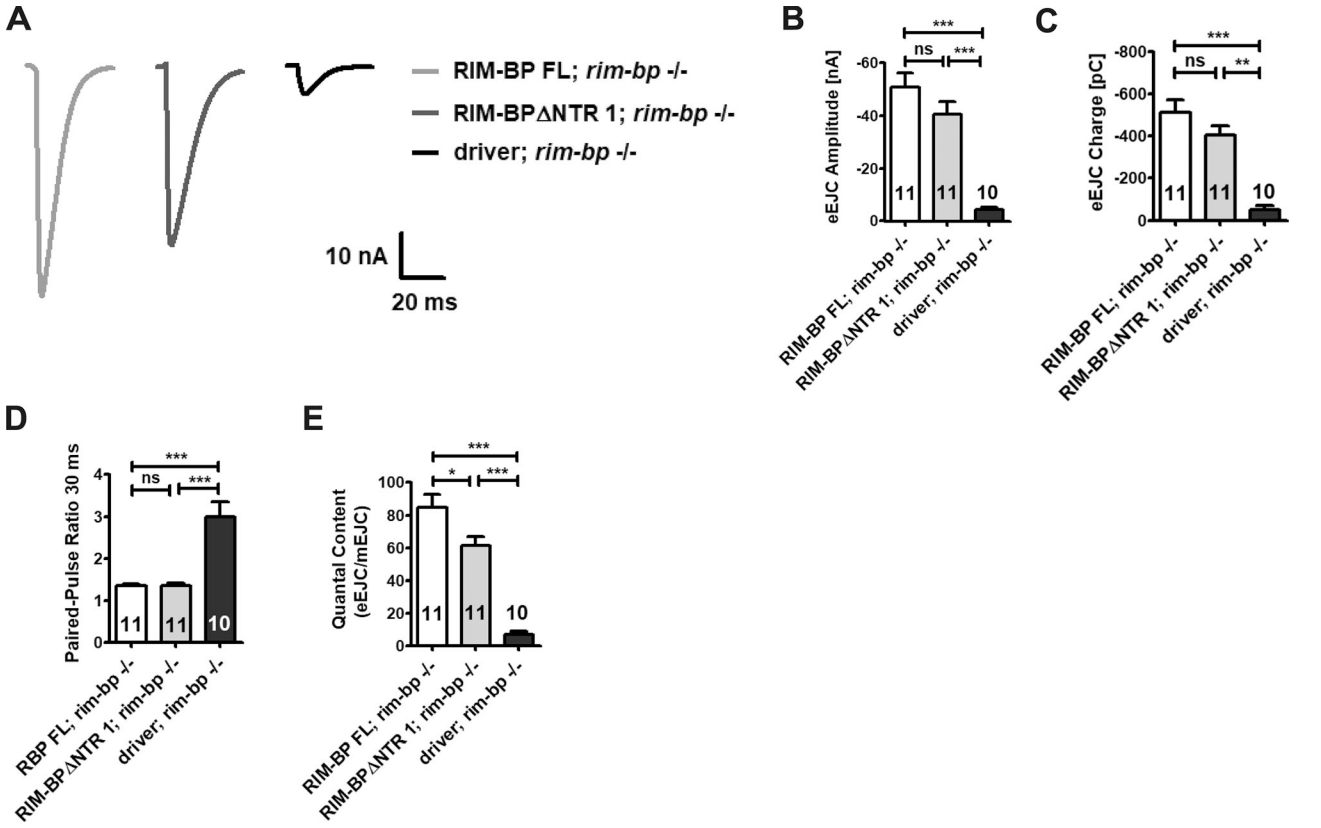

Figure S8. **RIM-BP NTR1 promotes SV recruitment into the release sites. (A–D)** Two-electrode voltage clamp electrophysiological recordings of *Drosophila* third instar larval NMJs expressing the RIM-BPΔNTR1^{GFP} construct in the *rim-bp* mutant background. **(A)** Example traces of evoked EJC. **(B)** eEJC amplitudes (RIM-BP-FL^{GFP} −50.93 ± 5.26 nA, *n* = 11; RIM-BPΔNTR1^{GFP} −40.62 ± 4.68 nA, *n* = 11; driver, *rim-bp* mutant −4.22 ± 1.07 nA, *n* = 10). **(C)** Evoked excitatory junctional charge (RIM-BP-FL^{GFP} −513.7 ± 60.94 pC, *n* = 11; RIM-BPΔNTR1^{GFP} −405.5 ± 43.61 nA, *n* = 11; driver, *rim-bp* mutant −50.72 ± 19.18 nA, *n* = 10). **(D)** 30 ms paired-pulse ratio (RIM-BP-FL^{GFP} 1.35 ± 0.04, *n* = 11; RIM-BPΔNTR1^{GFP} 1.36 ± 0.05, *n* = 11; driver, *rim-bp* mutant 3.0 ± 0.34, *n* = 10). **(E)** Quantal content (RIM-BP-FL^{GFP} 84.84 ± 7.84, *n* = 11; RIM-BPΔNTR1^{GFP} 61.17 ± 5.76 nA, *n* = 11; driver, *rim-bp* mutant 7.03 ± 1.93 nA, *n* = 10). **(B, D, and E)** all graphs show ± SEM. Data distribution is normal following the D'Agostino and Pearson omnibus normality test. A one-way ANOVA was applied, using Tukey post-test, *, P < 0.05; ***, P < 0.001; n.s. = not significant. N represents a single cell. Four to six animals are analyzed with one or two cells/animal. **(C)** Graph shows ± SEM. Data distribution is not normal following the D'Agostino and Pearson omnibus normality test; we therefore applied the nonparametric Kruskal–Wallis test with the Dunn's post-test, **, P < 0.01; ***, P < 0.001; n.s. = not significant. N represents a single cell. Four to six animals are analyzed with one or two cells/animal.

Table S1 is provided online. Table S1 shows diffraction data collection, phasing, and refinement statistics for FN-III(1).